ISSN: 1947-3931 Volume 2, Number 9, September 2010

Scientific Research

Engineering

Prof. David L. Carroll Wake Forest University, USA

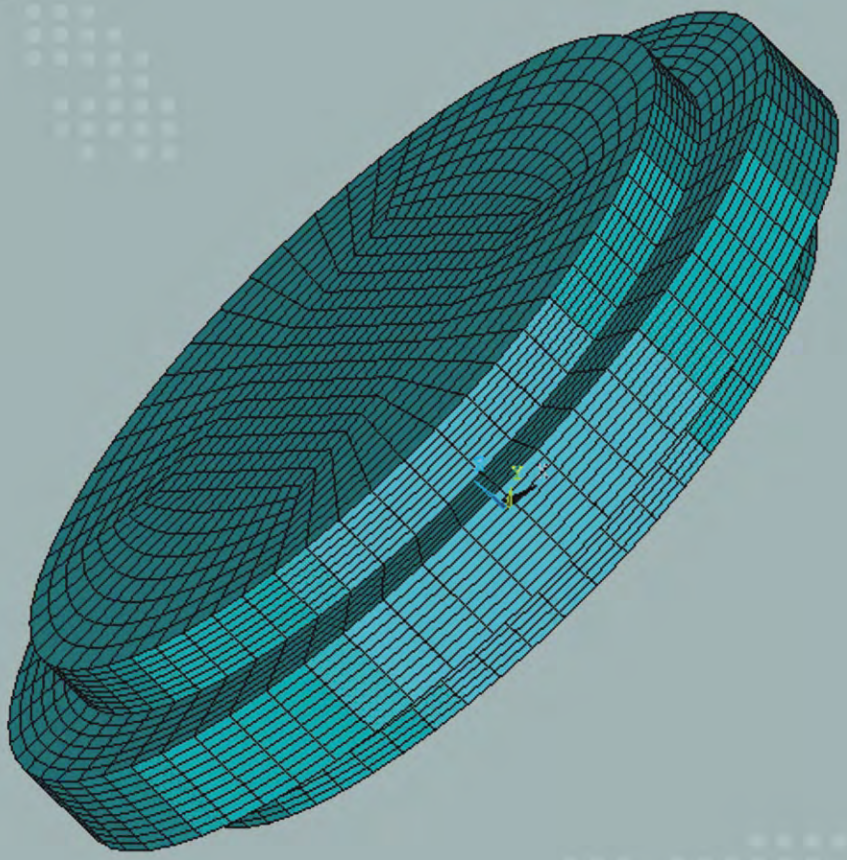

ISSN: 1947-3931

9 771947 393005 09

www.scirp.org/journal/eng/

Journal Editorial Board

ISSN: 1947-3931 (Print), 1947-394X (Online)

http://www.scirp.org/journal/eng

Engineering, 2010, 2, 673-749
Published Online September 2010 (http://www.SciRP.org/journal/eng)

TABLE OF CONTENTS

Volume 2 Number 9 September 2010

Engineering

Journal Information

SUBSCRIPTIONS

Engineering (Online at Scientific Research Publishing, www.SciRP.org) is published monthly by Scientific Research Publishing, Inc., USA.

Subscription rates:

Print: $50 per issue.
To subscribe, please contact Journals Subscriptions Department, E-mail: sub@scirp.org

SERVICES

Advertisements
Advertisement Sales Department, E-mail: service@scirp.org

Reprints (minimum quantity 100 copies)
Reprints Co-ordinator, Scientific Research Publishing, Inc., USA.
E-mail: sub@scirp.org

COPYRIGHT

PRODUCTION INFORMATION

For manuscripts that have been accepted for publication, please contact:
E-mail: eng@scirp.org

Engineering, 2010, 2, 673-682
doi:10.4236/eng.2010.29087 Published Online September 2010 (http://www.SciRP.org/journal/eng)

Static and Dynamic Characterization of High-Speed Silicon Carbide (SiC) Power Transistors

Johnson A. Asumadu[1], James D. Scofield[2]
[1]*Electrical and Computer Engineering Department, Western Michigan University, Kalamazoo, USA*
[2]*Air Force Research Laboratory/Propulsion Directorate, Power Division, Wright-Patterson Air Force Base, Dayton, USA*
E-mail: *johnson.asumadu@wmich.edu, james.scofield.1@us.af.mil*
Received September 14, 2009; *revised July* 23, 2010; *accepted July* 24, 2010

Abstract

This paper describes the operating characteristics of NPN 4H-SiC (a polytype of silicon carbide) bipolar junction transistor (BJT) and 4H-SiC Darlington Pairs. A large amount of experimental data was collected. The wafer BJTs were able to block over the rated 600 V in the common-emitter configuration and the TO-220 BJTs were able to block over the 1200 V rated voltage. In the thermal analysis, it is found out that at higher temperatures the forward and reverse (blocking) characteristics were stable at 100°C and 200°C. The transistors show positive temperature coefficients of forward voltage (*V*f). In general the current gain (β) characteristics obtained (with *V*CE = 6 V) were approximately as expected for the BJTs. The β's were very low (2 to 5 for wafer BJTs, 5 to 20 for the wafer Darlington Pairs, and 5 to 30 for TO-220 BJTs). The large amount of experimental data collected confirms some of the superior properties of the Silicon carbide material when used to fabricate power semiconductor devices, namely high thermal conductivity and high temperature operability. The data presented here will establish the trends and the performance of silicon carbide devices. The silicon carbide BJT has fast switching and recovery characteristics. From the analysis, silicon carbide power devices will be smaller (about 20 times) than a similar silicon power device and with reduced power losses. Silicon carbide will also be very useful for device integration in high densities, as found in integrated chips for current handling capabilities, for applications in instrumentation and measurements. Presently, most of the research is on improving the basic silicon carbide material quality, power device optimization, and applications engineering using devices that have been developed to date.

Keywords: Silicon Carbide, Static Characteristics, Dynamic Characteristics

1. Introduction

Today's efforts to replace conventional mechanical, hydraulic, and pneumatic power transfer systems with electric drives and their power electronics converters have taken off at an increasingly rapid rate (e.g., automobile electric brakes, traction control and electronic stability-control systems, electronic power-assisted steering (EPAS), etc.). The high demand for small power devices for instrumentation and measurements is expected to stay that way for many years to come, thereby challenging technology and circuit design in an unprecedented fashion. Biological and biologically-inspired instruments (e.g., nano-technology probes, MEMS, and so on) as well as portable equipment (e.g., laptops, palm pilots, camera recorders, midi players, meters, and more) are a few examples driving new areas of research in instrumentation and measurements. If silicon carbide (SiC) devices (power transistors, integrated chips (ICs), etc.) are developed and commercialized, they will replace silicon (Si) devices, since SiC devices will offer improvements to system weight, volume, losses, efficiency, and temperature capability. These improvements are needed over the next few years to realize the full potential of more-electric system paradigms and reduced power consumption goals. **Table 1** illustrates many of the benefits SiC has to offer. This paper is an expansion and continuation of our paper [1] on the characteristics of SiC bipolar transistors.

Silicon carbide material has been widely studied be-

Table 1. Comparison of the electrical and material properties of Si and SiC.

Property	Si	SiC
Bandgap (eV)	1.11	3.5
Maximum Temperature (°C)	425	> 900
Maximum Voltage (10^6V/cm)	0.3	4
Thermal Conductivity (W/cm°C) at 300° K	1.5	5
Electron Mobility (cm^2/Vs)	1350	500
Dielectric Constant	11.8	9.66
Process Maturity	High	Low
Intrinsically Hard	NO	YES

cause it is a promising material for higher power and high temperature applications. The properties of SiC include high field electric breakdown (2.2 MV/cm), high saturated electron drift velocity (2E7 cm/s), and high thermal conductivity (4.5 W/cm-K) making SiC very attractive for high-voltage, high-frequency, high power semiconductor devices and switches, including those for instrumentation and measurement. The properties of SiC material and power devices have been documented over the last twenty years [2-6].

Although 6H- and 4H-SiC polytypes are the most researched crystal structures, the 4H-SiC polytype dominates power device development activity because the electron mobility in 4H-SiC is two times that of 6H-SiC perpendicular to the *c*-axis and about ten times that of 6H-SiC parallel to the *c*-axis [7,8]. SiC Schottky Barrier Diodes (SBDs) have been available commercially since 2001 with 300 to 1200 volt, 175°C ratings. Although SiC power MOSFETs [8,9] have received significant emphasis, they continue to suffer from poor MOS channel mobility and reliability, especially in the 4H-SiC polytype. However, high voltage *npn* bipolar junction transistors (BJTs) and gate turn-off bipolar transistors (GTOs) in 4H-SiC have been demonstrated [9,12] with superior characteristics. SiC BJTs have been reported in the literature to block 1.8-2.5 kV with peak currents of over 30 A, with DC current gains of 40 when operated in the common-emitter configuration. The active area of these devices was in the 1 mm × 1.4 mm to 3.16 mm × 3.16 mm range. Static and dynamic characteristics of 6H-SiC Diodes, BJTs, and MOSFETs have been presented [10], but have had drawbacks in performance because of the poor electron mobility in the vertical direction. Despite the superior theoretical properties of SiC, material cost, base material quality, and substrate size are areas all requiring continued development and improvement prior to widespread technology adoption.

In this paper, the results of forward and reverse V-I characteristics, current gain characteristics, and dynamic measurements on 4H-SiC Darlington Pairs and BJTs in the common-emitter configuration are presented. The BJTs were characterized in two formats – on wafer probing and in TO-220 packages. The Darlington Pairs were in the wafer die format only. The current and voltage ratings of the wafer power devices are 5 A and 600 V, respectively, while the ratings of the TO-220 BJTs are 5 A and 1200 V, respectively. The active area of the 4H-SiC Darlington Pairs and BJTs are in the range of 1 to 3 mm^2 with emitter finger widths and spacings from 10 μm × 15 μm (pitch = 25 μm) to 10 μm × 27 μm (pitch = 37 μm), respectively. Device data presented in this paper represent the measured performance characteristics observed from numerous devices of each type, enabling reasonable statistical inferences.

2. Device Structure, Design, and Fabrication

2.1. Device Structure

The BJTs came in two formats – on wafers and in TO-220 packages. The Darlington Pairs were available only on wafers. The current and voltage ratings of the wafer power devices are 5 A and 600 V, respectively, while the TO-220 BJTs are 5 A and 1200 V. The **Figure 1** shows a typical BJT cross-sectional diagram of the implanted device on a wafer. The maximum overall cross-sectional dimension of a typical transistor is 235 μm × 235 μm.

The substrate material used for both Darlington Pairs and BJTs was n-type, 20 mΩ-cm 4H-SiC from Cree, Inc. on which n-collector, p-base, and n-emitter epitaxy of 10 μm 5E15 cm^{-3}, 1 μm 2E17 cm^{-3}, and 0.5 μm 5E19 cm^{-3}, respectively, were grown. Devices with active areas in the range of 1 to 3 mm^2 with emitter finger widths and spacings from 10 μm × 15 μm (pitch = 25 μm) to 10 μm × 27 μm (pitch = 37 μm), respectively, were subsequently fabricated for testing. **Figure 2** shows how a Darlington Pair and BJT images are laid out on a single wafer probing Reticle. There are several images on a

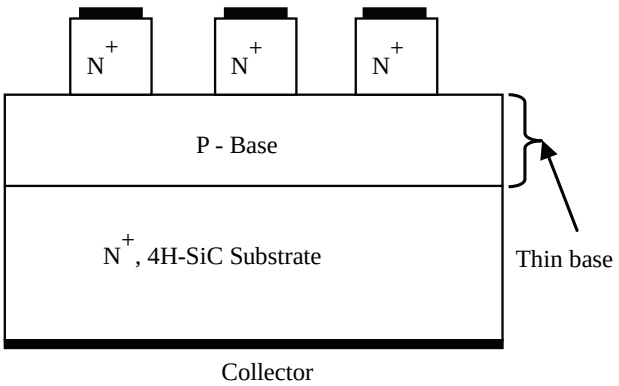

Figure 1. Simplified cross-section structure of 4H-SiC BJT.

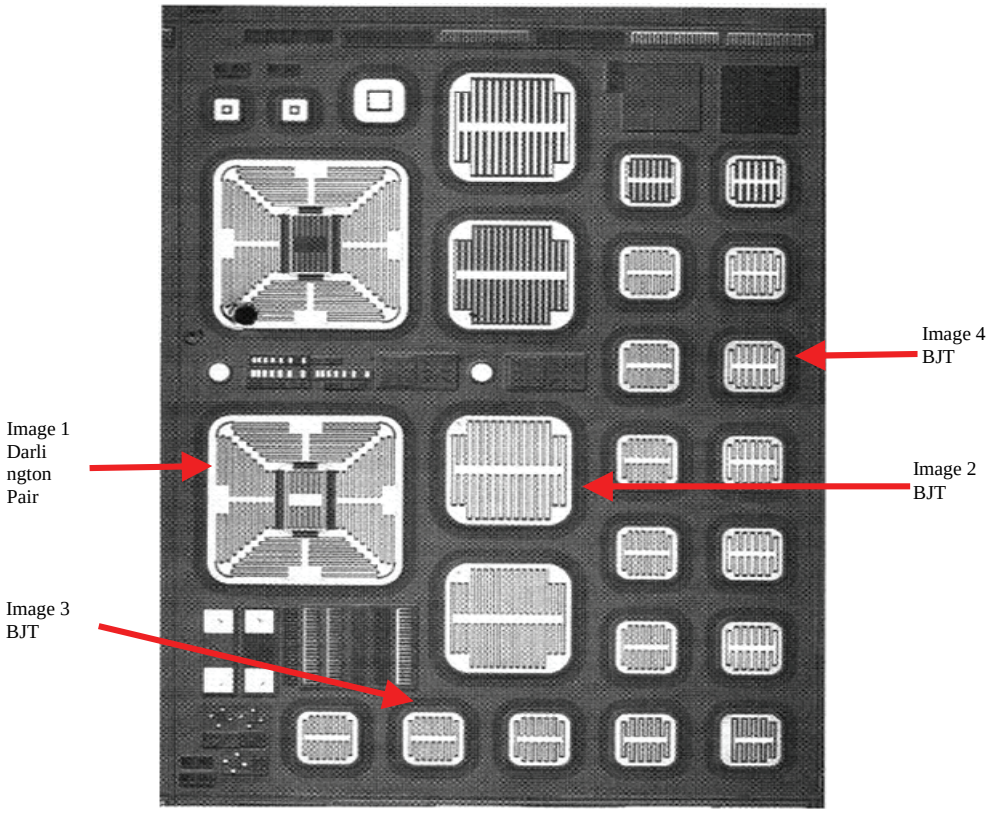

Figure 2. Reticle design layout of BJT and Darlington pair images.

Reticle. Image 1 on all the Reticles is a Darlington Pair and the remaining images are all BJTs. The characteristics were measured on 4 wafer Reticles with different orientation, resistivity, and thickness. The images selected on a Reticle are Image 1 – Darlington Pair and Images 2 to 4 – BJTs as shown in **Figure 2**.

2.2. Device Design and Fabrication

Table 2 shows the emitter configurations (emitter width (x), base width (y)) and pitch ($x + y$) of the selected Images 2, 3, and 4. The emitter configuration of Darlington Pair (Image 1) was not available (N/A). A Darlington Pair was designed to contain 54 emitter fingers and a BJT has 28 emitter figures. The distance between the implanted edge termination regions for devices is typically 2 μm. **Table 3** shows the off-axis orientation, resistivity, and thickness of the four device wafer Reticles. **Figure 3** shows examples of the top view of a fabricated 4H-SiC Darlington Pair and a BJT.

3. Experimental Setup

The forward and reverse *V*ce vs. *I*c characteristics were measured using Tektronix 371 curve tracer for both the wafer and the TO-220 BJTs. The dynamic characteristics were similarly measured but only on the TO-220 BJTs. Even though large amount of data was collected for these studies, results are presented for typical Darlington Pair and typical BJT devices from the wafer Reticles, and the TO-220 BJTs.

4. Experimental Results and Discussions

4.1. Experimental Results – Wafer Probing 4H-SiC Darlington Pair and BJT

4.1.1. Forward and Reverse (Blocking) Characteristics

The **Figures 4** and **5** show the forward and reverse (blocking) *V*ce vs. *I*c characteristics for a typical Dar-

Table 2. Reticle active area.

Images	Emitter Width (x)	Base Width (y)	Pitch (x + y)
1	N/A	N/A	N/A
2	15	15	30
3	10	15	25
4	15	15	30

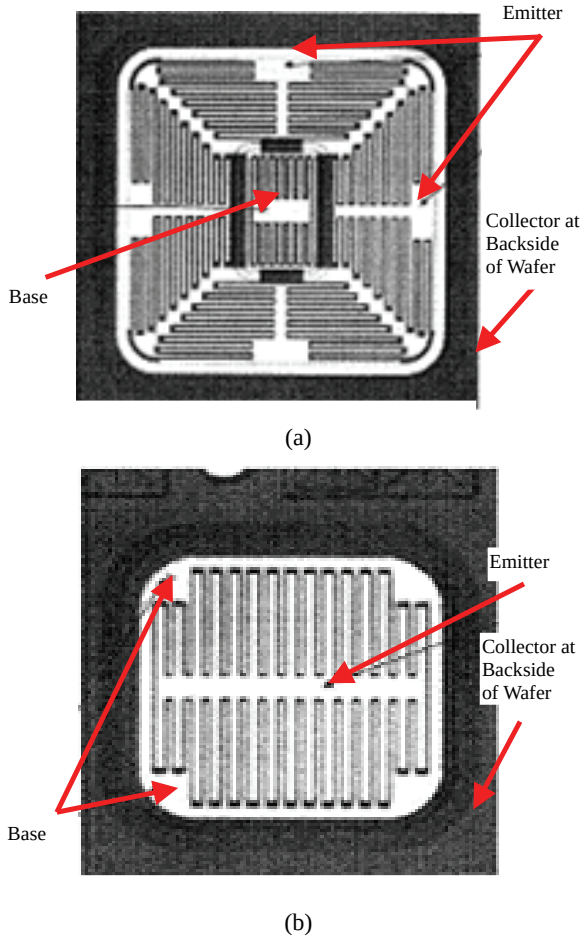

Figure 3. (a) Top view of a fabricated 4H-SiC Darlington Pair; (b) Top view of a fabricated 4H-SiC BJT.

lington Pair (Image 1 on Reticle # 2).

Similarly, the **Figures 6** and **7** show the forward and reverse *V*ce vs. *I*c characteristics for a typical BJT (Image 4 on Reticle #4). The sustaining voltage *BV*CE0 ranges from 200 V to 800 V for the Darlington Pair and from 200 V to 1200 V for the BJTs. The designed stand-off voltage of the BJT epitaxy was 600 V.

Reverse voltage characteristics depend on the drift layer thickness, the base doping used, and the base contact implantation tail, which tends to decrease the base width. High current gain and high reverse voltage can be achieved with the proper doping and width of base, and an optimized carrier lifetime.

4.1.2. Current Gain

The **Figure 8** shows the forward current gain characteristics (base current *I*b vs. β) of the above-mentioned devices. The maximum current gains (βmax) occur at room temperature and decrease as temperature and base current increase. The low current gains in Darlington Pair and most of the BJT samples may be due to 1) low emitter injection efficiency because of high base doping and/or low emitter doping, 2) low minority carrier life-times in the base layer, and 3) poor ohmic contact resistance of the p + layer contact [9-12].

The **Figure 8** also shows the effect of temperature on the common-emitter current gains (β) from room temperature to 200°C. As temperature increases, background carrier concentrations in the base region increase. This is due to an increase in the ionization fraction of the aluminum (E_A ~200 meV) acceptors, as a result, emitter

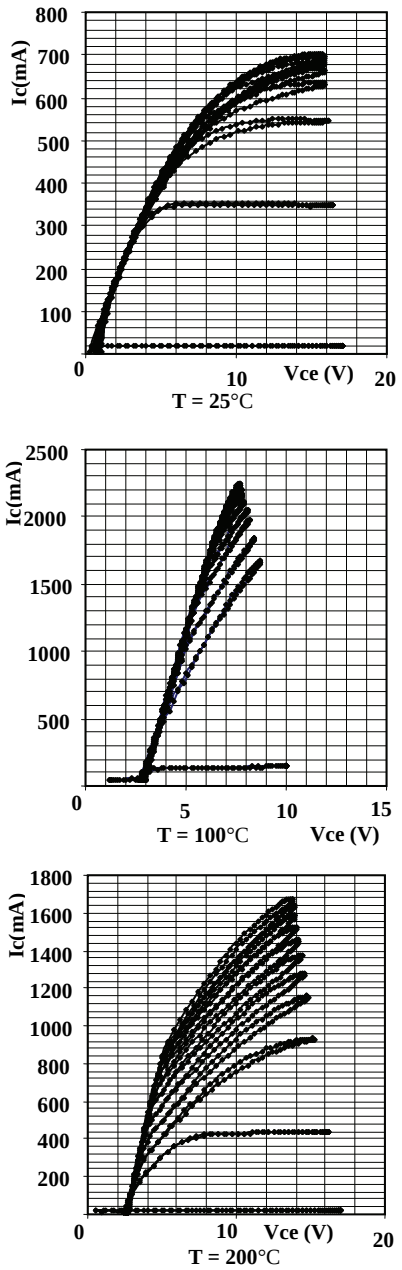

Figure 4. Darlington pair forward *V*ce-*I*c characteristics at 25°C, 100°C, & 200°C.

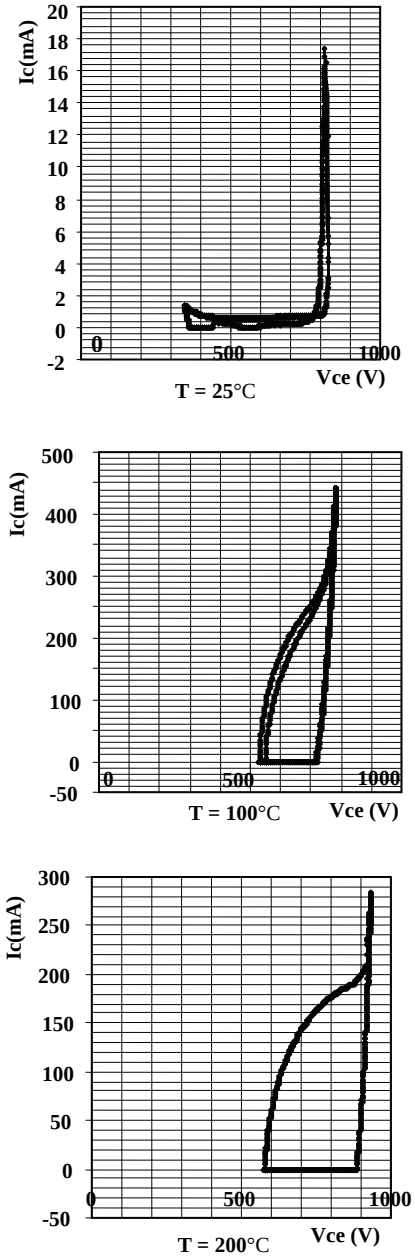

Figure 5. Darlington Pair reverse *V*ce-*I*c characteristics at 25°C, 100°C, & 200°C.

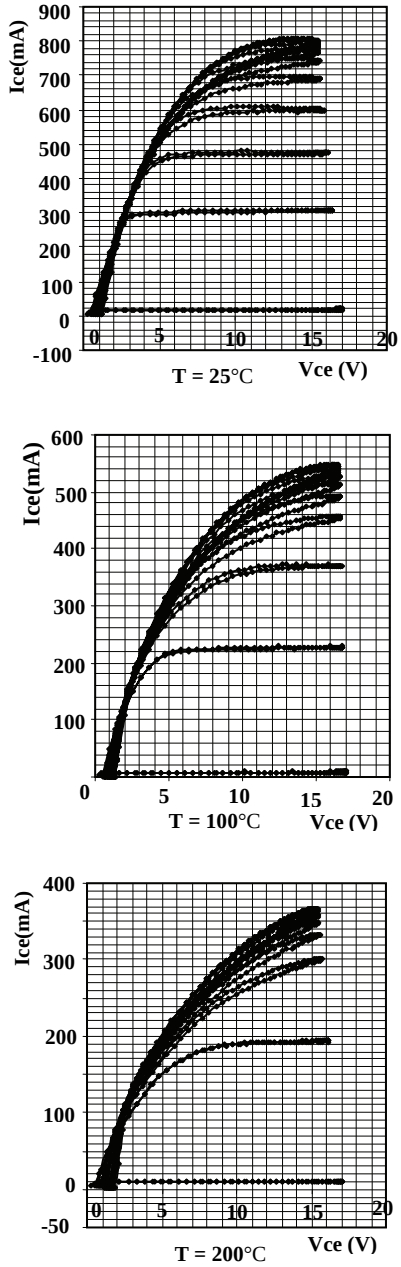

Figure 6. BJT Pair forward *V*ce-*I*c characteristics at 25°C, 100°C, & 200°C.

injection efficiency decreases. As a consequence of this, increases with temperature to the minority carrier lifetimes are offset. The result is that the common-emitter current gain, β decreases with temperature (a negative temperature coefficient not observed in silicon (Si) devices). This prevents thermal runaway and makes the SiC power device very attractive for paralleling. Also, the on-resistance will increase because of a decrease in collector layer electron mobility. In general, all the common-emitter current gain characteristics were in the range shown in **Figure 8**.

4.1.3. Early Voltage

Table 4 shows representative values of device Early Voltages (*V*A) at room temperature from three different Reticles. The devices showed *V*A ranging from 115 V to 2000 V. The *V*A of a typical Darlington Pair ranges from 115 to 165 V. The *V*A of Darlington Pairs on some of the Reticles was much higher; ranging from 118 V to 1900 V. The *V*A of a typical BJT ranges from 325 V to 347 V. The *V*A of BJTs on some of the Reticles was much higher; ranging from 267 V to 2000 V.

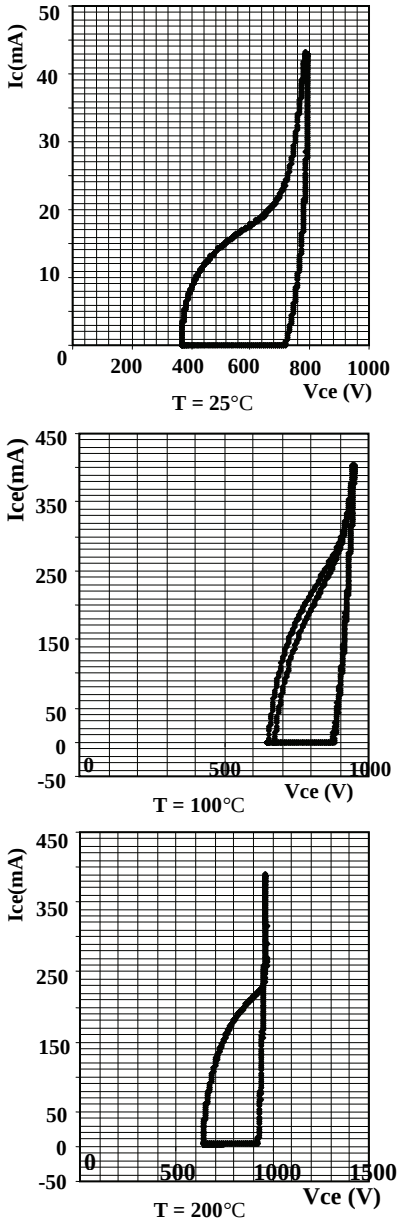

Figure 7. BJT Pair reverse *V*ce-*I*c characteristics at 25°C, 100°C and 200°C.

Table 4. Early voltage.

Images		VA1	VA2	VA3
Image 1	Darling Pair	165.912	156.711	155.189
Image 3	BJT	325.383	347.990	330.968

The *V*A values are very high, which could imply that the effective base width is large, possibly due to carrier trapping at deep level defects and compensated base doping. This would be consistent with the low current gains (low base carrier lifetimes) and high Early Voltages observed.

4.2. Experimental Results – TO-220 BJTs

4.2.1. Forward and Reverse (Block) Characteristics, and Current Gain

The **Figures 9** and **10** show typical forward (*I*b = 20 mA in steps) and reverse characteristics representative of the 4H-SiC BJTs in the TO-220 casing. **Figure 11** shows the *I*b vs. β characteristics for the same devices. Typical values of β vary from 5 to 29, with maximum current gain (βmax) of about 30 at room temperature and 200 mA base current. The decrease in the current gain at room temperature and at 200°C is relatively small. The maximum collector current at room temperature was about 6 A but reduces to about 5 A at 200°C. These improved characteristics, compared to the wafer devices, reflect an improved base layer epitaxy process yielding enhanced transport characteristics.

At high temperatures the emitter injection efficiency is reduced, due to the increase in majority carrier concentration in the base from an increased deep acceptor ionization fraction. The expected variation in the forward characteristics between room temperature and at 200°C is due to the positive temperature coefficient of $R_{DS,ON}$. The epitaxial growth process was optimized to increase the minority carrier lifetime in the emitter and base layers, which in turn leads to higher dc current gain. This was accomplished by performing the growth at lower

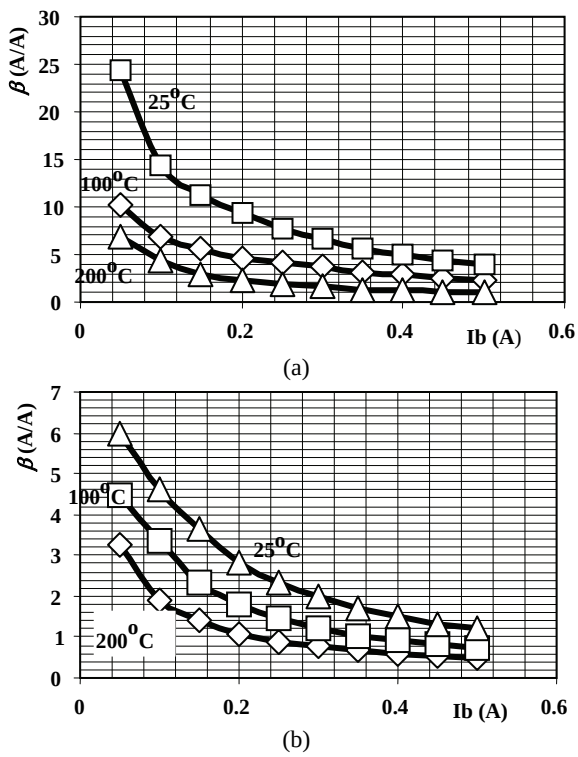

Figure 8. (a) Darlington Pair Current (I_b) vs. Gain (β); (b) BJT Current (*I*b) vs. Gain (β).

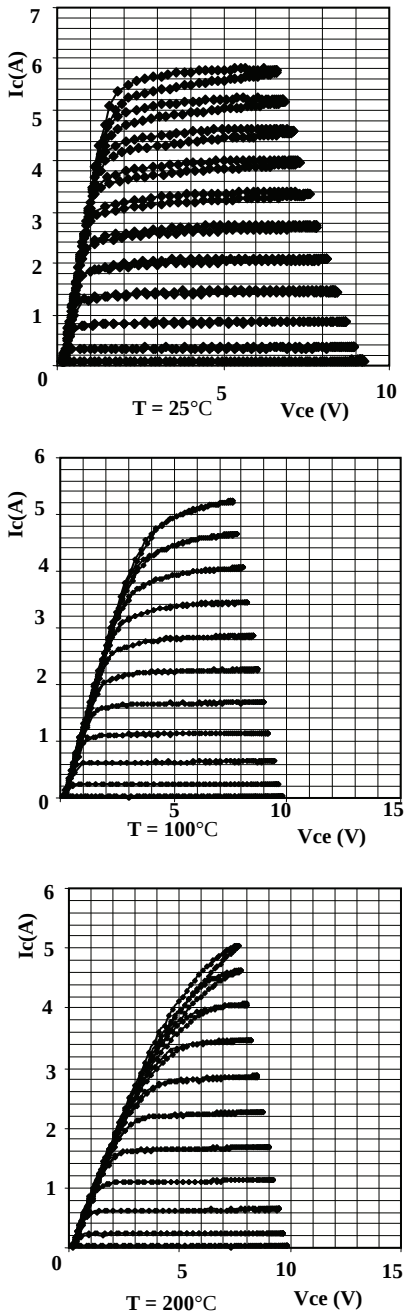

Figure 9. TO-220 BJT forward *V*ce-*I*c characteristics at 25°C, 100°C and 200°C.

temperatures, reducing point defects and impurities, and maintaining stoichiometry of the highly doped emitter layer.

Due to SiC's higher on-state conductivity and lower off-state leakage current at high operating temperatures compared to Si, superior performance at high operating junction temperatures, including lower power dissipation in the active area of the device is realized.

4.2.2. Dynamic Characteristics

Figure 12 shows the experimental setup used to study the dynamic characteristics of the 4H-SiC BJTs (TO-220 casing) and the sustaining voltage between the collector terminal and the emitter terminal (*V*CE0(sus)). The dynamic characteristics are performed at room temperature.

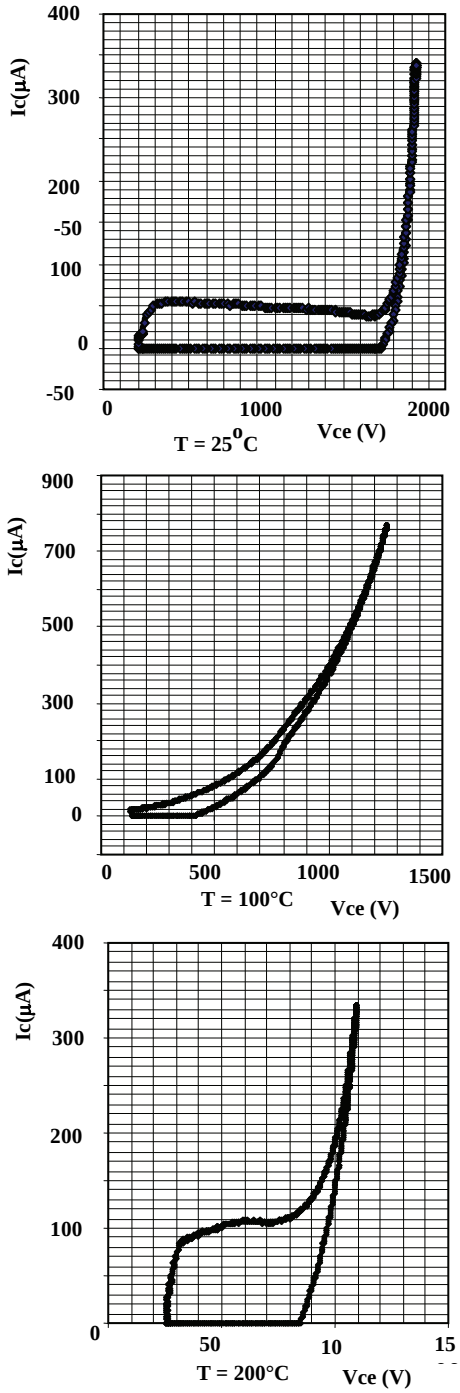

Figure 10. TO-220 BJT reverse V_{ce}–I_c characteristics at 25°C, 100°C, and 200°C.

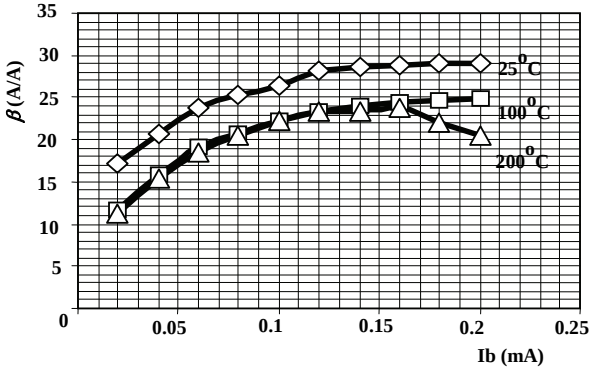

Figure 11. TO-220 BJT Current (I_b) – Gain (β).

The dynamic characteristics analysis was performed at low voltage due to restrictions of the test equipment. The circuit was constructed using a power supply of 15 V, low-power resistors, current probes, and operated from a pulse generator at two switching frequencies (100 kHz and 1 MHz with a duty-cycle ratio of 50%). The load resistance was approximately 20 ohm (rated 20 W) connected in the common-emitter configuration mode.

The SiC power BJT was turned on and off by applying the pulses of the generator to the base of the transistor. The turn-on and turn-off measurements were taken at room temperature.

Figure 13(a) shows typical turn-on characteristics of a 4H-SiC BJT with the pulse generator operated at 100 kHz. The turn-on rise time is much faster than a typical Si BJT. A typical turn-on rise time of 312 ns was observed at room temperature. **Figure 13(b)** shows the turn-off characteristics of the 4H-SiC BJT at room temperature. The turn-off fall time is observed to be nominally 92.5 ns at room temperature. Turn-on rise time can be improved by decreasing the base contact resistance and by increasing carrier extraction in the base-emitter junction.

Switching speeds in this range are indicative of well controlled minority carrier lifetimes in the base. Very short turn-off times are obtained even though the junction breakdown voltage *V*BE is less than 10 V. The dynamic characteristics shows that the switching features of the SiC power devices can be very fast but at high frequencies the controlling external circuit must have high switching speed (rise time). The very fast switching characteristics show that a SiC-based BJT device has low effective stored charge even when operated at high temperatures. Therefore, the switching losses in SiC devices caused by the stored charges are negligible in these devices; whereas about 30% of losses in Si power devices and ICs occur during switching [9]. The switching circuits required can be totally integrated into the switching scheme, and can be dynamically adaptive, fast, ultra low losses, and very small size. The SiC-devices have excellent high short circuit capability, especially suitable for commuting applications in power electronics and switching circuits.

Maximum sustaining voltage characteristics, between the collector terminal and the emitter terminal, at a collector current of 100 mA is shown in **Figure 14**. A 392 μH inductance was placed in the collector leg of the circuit shown in **Figure 12**.

The transistor was subjected to a transient voltage forcing the transistor to go into avalanche breakdown for a short time. The sustaining collector-emitter voltage *V*CE0(sus) was observed to be 40 V (at collector current of 100 mA) at room temperature.

Figure 15(a) shows typical turn-on and turn-off characteristics of a 4H-SiC BJT, with the pulse generator operated at 1 MHz. It was observed that the voltage at the collector collapsed. Even though the BJT turn-on rise time has been shown to be 312 ns (3.205 MHz), the power supply failed because the switching speed (the rise time) of the power supply is lower than 1 MHz (restrictions of the test equipment).

Figure 15(b) shows the characteristics of the maximum sustaining collector-emitter voltage at a switching frequency of 1 MHz. The sustaining voltage *V*CE0(sus) was observed to be 25 V (at collector current of 100 mA) at room temperature. The sustaining voltage should have remained relatively constant at collector current of 100 mA for all the switching frequencies. However, the switching speed (the rise time) of the power supply is less than 1 MHz and contributed to this anomaly.

5. Conclusions

The experimental data collected confirms some of the

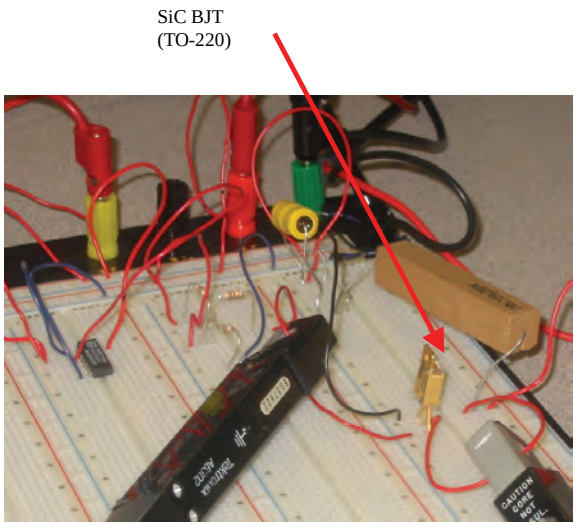

Figure 12. Experimental setup for dynamic characteristics.

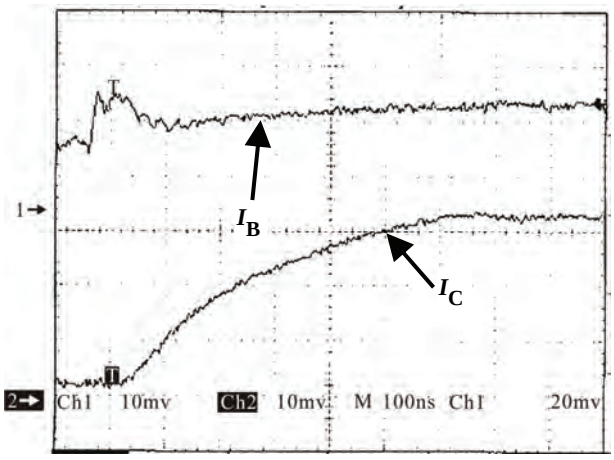

(a)

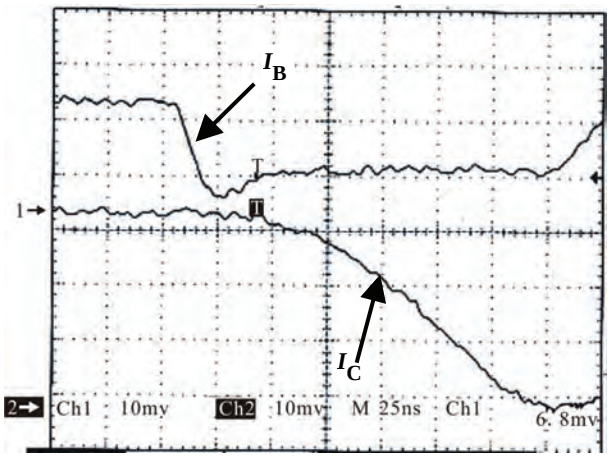

(b)

Figure 13. (a) Turn-on characteristics at 100 kHz; (b) Turn-off characteristics at 100 kHz.

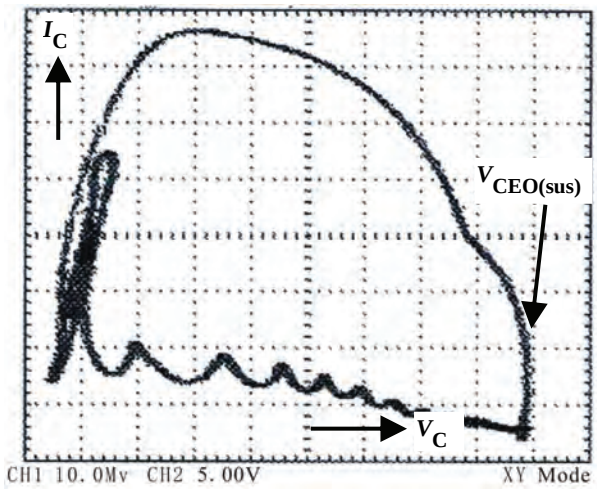

Figure 14. Maximum sustaining voltage (at collector current of 100 mA) at 100 kHz.

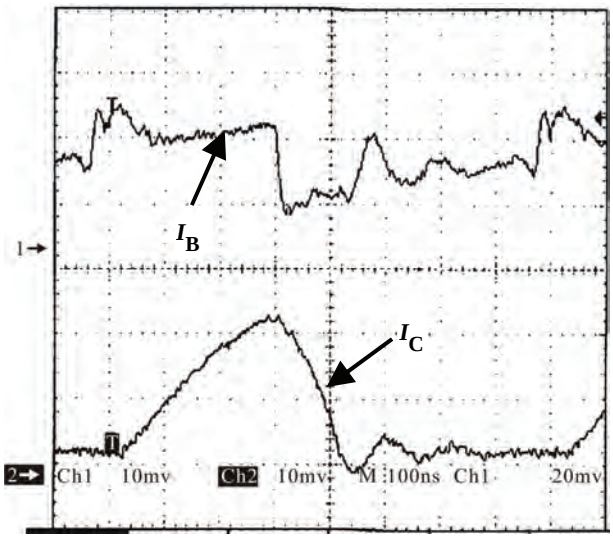

(a)

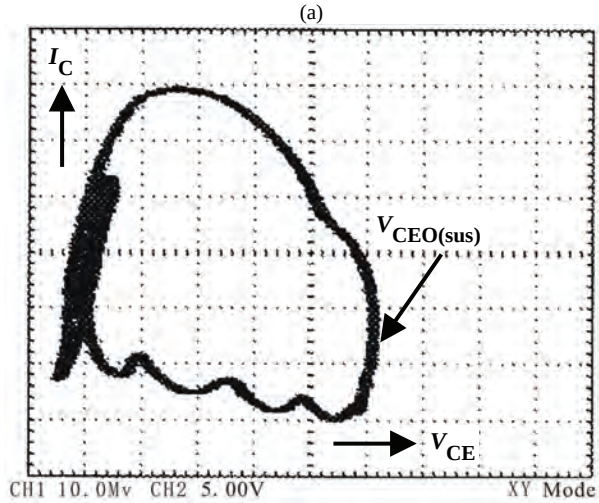

(b)

Figure 15. (a) Dynamic characteristics at 1 MHz; (b) Maximum sustaining voltage (at collector current of 100 mA) at 1 MHz.

superior properties of the SiC material when used to fabricate electrical and electronics devices for applications in power electronics, instrumentation and measurements. The forward characteristic exhibited stability at high temperatures because of the higher percentage of deep level acceptor ionization in the base region. The gain also decreases as the temperature increases. This negative temperature coefficient property prevents thermal runaway and makes SiC power BJT devices very attractive for paralleling. The BJTs also show high reverse (blocking) voltages considering the fact that the effective on-resistances (6 mΩ-cm^2 at 25°C) of these devices are very small. The current gain, however, was observed to decrease for BJTs with smaller pitches, possibly caused by limited recombination in the base region and low emitter injection efficiency due to emitter crowding ef-

fects. Base layer ohmic contacts need improvement to reduce the ~5E-3 Ω-cm^2 specific base contact resistivity measured. The Early Voltage values were very high which likely is due to large effective base widths. This is consistent with low current gain and high Early Voltage effect. The other very prominent features of the SiC BJT include the fast turn-on switching speed, very fast turn-off time, and the robust behavior under critical thermal conditions.

Two key observations can be made from the data collected. First, for example, a 1000-volt SiC power device will be 5X smaller or 5X more efficient than comparable Si device operating at twice the environmental temperature. Secondary, SiC power devices will reduce switching power losses in many applications.

6. References

[1] J. A. Asumadu and J. D. Scofield, "Characteristics of High-Speed Silicon Carbide (SiC) Transistor," *Proceedings of the* 24*th IEEE Instrumentation and Technology Conference*, Warsaw, Vol. 2, 1-3 May 2007, p. 36.

[2] A. K. Agarwal, S. H. Ryu, J. Richmond, C. Capell, J. W. Palmour, Y. Tang, S. Balachandran and T. P. Chow, "Large Area, 1.3 kV, 17 A, Bipolar Junction Transistor in 4H-SiC," *ISPSD*, 2003.

[3] W. J. Choyke and E. D. Palik, "Silicon Carbide (SiC), Handbook of Optical Constants of Solids," Academic Press, Inc., New York, 1985, pp. 587-595.

[4] H. R. Philip and E. A. Taft, "Intrinsic Optical Absorption of in Single Crystal Silicon Carbide," *Silicon Carbide*, Eds., J. R. O'Connor and J. Smiltens, New York, Pergamon, 1960, pp. 366-370.

[5] S. Liu and J. D. Scofield, "Thermally Stable Ohmic Contacts to 6H- and 4H- p-Type SiC," *High Temperature Electronics Conference*, 1998, *HITEC* 4*th International*, San Diego, 14-18 June 1998, pp. 88-92.

[6] M. Bhatnagar and B. J. Baliga, "Comparison of 6H-SiC, 3C-SiC, and Si for Power Devices," *IEEE Transactions on Electron Devices*, Vol. 40, No. 4, March 1993, pp. 645 -655.

[7] C. E. Weitzel, J. W. Palmour, C. H. Carter Jr., K. Moore, K. J. Nordquist, S. Allen, C. Thero and M. Bhatnagar, "Silicon Carbide High-Power Devices," *IEEE Transactions on Electron Devices*, Vol. 43, No. 10, October 1996, pp. 1732-1741.

[8] W. J. Schaffer, G. H. Negley, K. G. Irvine and J. W. Palmour, "Conductivity Anisotropy in Epitaxial 6H and 4H SiC, in Diamond, and Nitride Wide Bandgap Semiconductors," *Material Research Society Proceedings*, Vol. 339, MRS, Pittsburgh, 1994, pp. 595-600.

[9] S. H. Ryu, A. K. Agarwal, R. Singh and J. W. Palmour, "1800 V NPN Bipolar Junction Transistors in 4H-SiC," *IEEE Electron Device Letters*, Vol. 22, No. 1, March 2001, pp. 119-120.

[10] P. Fredricks, H. Mitlehner, K. O. Dohnke, D. Peters, R. Schorner, U. Weinert, E. Baudelot and D. Stephani, "SiC Power Devices With Low On-Resistance for Fast Switching Applications," *IPSD*2000, Toulouse, 22-25 May 2000, pp. 213-216.

[11] A. K. Agarwal, S. H. Ryu, C. Capell, J. Richmond, J. W. Palmour, B. Phan, J. Stambaugh, H. Bartlow and K. Brewer, "SiC BJT's for High Power Switching and RF Applications," *Materials Research Society Symposium Proceedings*, Vol. 742, 2003, pp. K7.3.1-K7.3.6.

[12] Y. Tang, J. B. Fedison and T. P. Chow, "An Implanted-Emitter 4H-SiC Bipolar Transistor with High Current Gain," *IEEE Electron Device Letters*, Vol. 22, No. 3, March 2001, pp. 119-120.

Engineering, 2010, 2, 683-689
doi:10.4236/eng.2010.29088 Published Online September 2010 (http://www.SciRP.org/journal/eng)

Arbuscular Mycorrhizal Technology in Reclamation and Revegetation of Coal Mine Spoils under Various Revegetation Models

Akhilesh Kumar[1], Richa Raghuwanshi[2*], Ram Sanmukh Upadhyay[3]
[1]*Government Degree College, Narnaul, India*
[2]*Department of Botany, Mahila Mahavidyalaya Banaras Hindu University, Varanasi, India*
[3]*Department of Botany, Banaras Hindu University, Varanasi, India*
E-mail: {*akhilesh*_100, *upadyay_bhu*}*@yahoo.co.uk, richabhu@yahoo.co.in*
Received November 25, 2009; *revised July* 21, 2010; *accepted August* 23, 2010

Abstract

Reclamation and revegetation of a coal mine spoils with various revegetation models utilizing the mycorrhizal technology were studied. The models with different combination of plant species were designed to test the hypothesis of speedy revegetation. Root colonization and spore density of arbuscular mycorrhizae (AM) were lowest in plants seeded directly on slopes of the overburden (coal mine dump). At flat surfaces, the mycorrhizal colonization in plant species was higher than that observed at slopes. In other revegetation models, *i.e.*, tree monoculture, tree monoculture + crop species (agroforestry), and two strata plantations (combination of different plant species), maximum AM colonization was recorded for tree species grown along with crop species. This was followed by two strata plantations and tree monoculture. In two strata plantations three categories of AM associations were recognized: 1) every plant in the combination, possessed high mycorrhizal association, 2) only one plant in the combination possessed high mycorrhizal association, and 3) none of the plants in the combination possessed high mycorrhizal association. *Azadirachta indica*, *Pongamia pinnata*, *Leucaena leucocephala* and *Acacia catechu* were most effective in catching mycorrhizae, and can be used as the effective tool in rehabilitation of the degraded ecosystems.

Keywords: Coal Mine Spoils, Reclamation, Revegetation and Mycorrhizae

1. Introduction

AM fungi form the fundamental linkage between the biotic and abiotic components of the ecosystem in addition to their being the primary colonizers of coal mine spoils [1-2]. The primary approach to revegetation of such spoils is the erosion control through plant cover in short-term and development of a self-sustaining community through colonization of native plants in the long-term [3]. The soil conservation practices not only make the soil resistant to erosion, but also directly affect the soil pore size distribution [4]. The soil aggregates and pore size collectively constitute 'soil structure' which in turn influences not only the physico-chemical but also the biological processes [5-6]. The contribution of AM fungi to soil aggregate formation can be grouped into three categories according to Miller and Jastrow [7]: These are: 1) growth of external AM hyphae in the soil matrix to create the skeleton that holds primarily the soil particles (*i.e.* sand, silt and clays) together via physical entanglement, 2) creation of conditions by roots and external hyphae conducive to formation of microaggregates whereby mineral particles and organic debris are held and cemented together by various physico-chemical events involving binding agents like the persistent gums and glues in the root exudates, the soil microbes and mycorrhizal hyphae in particular contribute hydrophobic glycoprotein glomalin [8], and 3) enmeshment of microaggregates and smaller macroaggregates by external hyphae and roots to form the macroaggregates that can be further stabilized by intermicoraggregate and intermacroaggregate cementation by polysaccharides and other organics from microorganisms and plant roots. These three processes operate simultaneously because of dynamic

nature of soil aggregation. The improvement in soil aggregation sustains ideal water infiltration, tilth and aeration for plant growth [9].

There are countless reasons to qualify mycorrhizae as bliss for revegetation programmes as infection of plant roots by such fungi induces tolerance against the abiotic and biotic stresses. Mycorrhizal fungi appear to partially protect plants against heavy metal toxicity through binding and thus limiting their translocation to shoots [10]. The host plant in turn may give the fungus a selective survival advantage on a contaminated site. The metal sequestration by AMF may alter their translocation in plants thus restricting metal accumulation in mycorrhizal roots and so also reduce metal transfer to the aboveground biomass [11]. The only direct evidence of mycorrhizal adaptation to metal pollutants is the exudation of complexing organic acids that alter pollutant availability in the rhizosphere [12]. Metallophytes have evolved various physiological adaptations to successfully compete with the harsh conditions in heavy metal loaded soils. In addition, AMF that colonize plant roots, considerably reduce the intake of heavy metals by plant cells that could be one of the strategies that allows metallophytes to thrive on heavy metal polluted sites [13-14]. Haselwandter [15] proposed that a metal-resistant plant breed susceptible to mycorrhizal symbiosis would be of great value for the rehabilitation of metal contaminated soils. AM fungi that modify the root system and play a critical role in the nutrient cycling in the ecosystem, can be taken as a crucial parameter to access reclamation success of degraded lands. Thus, restoration success depends on the augmentation of biological activity of the surface soil horizons [16]. In view of the above, the present study was carried out by developing a revegetation model site at the coal mine spoil site utilizing mycorrhizal technology.

2. Materials and Methods

Revegetation model site (RMS) was developed at Jayant Coal Mine situated in Singrauli district of Madhya Pradesh, India. An area of about 9 hectare of fresh overburden was smoothened and flattened by bulldozers for plantations in various models designed. Seedlings raised in nursery by either seeds or cuttings were transplanted at the RMS. In each revegetation model, the plot size was 20 m × 20 m where the plants were transplanted in pit size of 40 cm × 40 cm × 30 cm with the spacing of 2 m × 2 m. The density of the plants per plot was 100. Seeds of different plant species were seeded directly by broadcasting in case of direct seedling, whereas in rest of the cases the seedlings raised in nursery were transplanted at RMS. The combination of plants species in different plots at RMS were as follows:

***Direct seeding on slope surface*:** Seeds of different plant species used in direct seeding on slope surface were *Acacia catechu*, *Azadirachta indica*, *Leucaena leucocephala*, *Madhuca indica*, *Pongamia pinnata*, *Syzygium cumini*, *Terminalia arjuna* and *Terminalia bellirica*.

***Direct seeding on flat surface*:** The plant species selected were *A. catechu*, *Acacia nilotica*, *A. indica*, *L. leucocephala*, *M. indica*, *P. pinnata*, *S. cumini*, *T. arjuna* and *Zizyphus jujuba*.

***Tree monoculture*:** The species raised in monoculture plots were *A. catechu*, *Albizia lebbeck*, *A. indica*, *Dalbergia sissoo*, *Dendrocalamus strictus*, *Gmelina arborea*, *L. leucocephala*, *Phyllanthus emblica*, *P. pinnata*, *Tectona grandis* and *T. bellirica*.

***Tree monoculture + crop plant* (*Agroforestry*):** The leguminous *Cajanus cajan* was sown in combination with *A. lebbeck*, *A. indica*, *G. arborea*, *P. pinnata*, *T. bellirica* and *T. grandis*. *Pennisetum typhoides* a non-leguminous crop semi-arid tropics was seeded with combination of *A. indica*, *D. sissoo*, *L. leucocephala* and *P. pinnata*.

***Two strata plantation*:** Mixed plantations were raised with the following combinations of leguminous and non-leguminous species: *A. catechu* + *P. pinnata*, *A. lebbeck* + *A. catechu*, *A. indica* + *P. emblica*, *D. strictus* + *T. grandis*, *G. arborea* + *P. pinnata*, *P. pinnata* + *T. bellirica*, *T. bellirica* + *G. arborea* and *T. grandis* + *L. leucocephala*.

In all the above models, ground seeding with a leguminous forb *Stylosanthes hamata* and two grasses namely *Pennisetum pedicellatum* and *Heteropogan contortus* was done by broadcasting.

3. Assessment of AM Association

Composite samples of soil and roots were collected from each plot and isolation of AM spores was done by wet sieving and decanting methods of Gerdemann and Nicolson [17] and sucrose centrifugation method of Jenkins [18]. The number of AM spores per hundred gram of dry soil was estimated.

The root samples were washed, cut into one cm segments, and placed in tissue capsule [19]. These were cleared and stained with Chlorazol Black E (CBE) in lactoglycerol following the procedure of Phillips and Hayman [20]. One hundred root segments were randomly selected and mounted on microscopic slides for observation. Quantification of the root colonization is based on percentage of AM colonization. Association of mycorrhizae was based on the presence or absence of

arbuscules, vesicles and internal hyphae in the root tissue.

4. Results

Dynamics of AM in plant roots and rhizosphere soil was studied in various models at the revegeatation site. The models with plantation of various combinations of plant species were designed to test the extent of speedy revegetation of coal mine spoils. The lowest level of mycorrhizal association was found in plants seeded directly on slopes (**Figure 1**). At flat surfaces, AM colonization in plant roots was higher than that observed at slope surfaces (**Figure 2**), but it was lesser as compared to other models. *A. indica, L. leucocephala, M. indica* and *P. pinnata* harboured significantly higher level of AM at slopes while it was significantly higher in *A. catechu, A. nilotica, A. indica, L. leucocephala* and *P. pinnata* at flat surfaces. In other plants the AM association was poor both at slopes and flat surfaces.

In rest of three revegetation models (*i.e.*, tree monoculture, tree monoculture + crop species and two strata plantations) nursery raised seedling were transplanted at RMS in pits in various combinations. The highest level of AM colonization was recorded for the tree species grown with crop species (agroforsetry) followed by the two strata plantations and tree monoculture. Two species namely *A. indica*, and *D. sissoo* possessed significantly ($p = 0.01$) higher level of AM colonization than others rose in monoculture (**Figure 3**). The rhizosphere soil of *L. leucocephala* and *P. pinnata* possessed higher AM spore count than others. When the tree species were seeded along with crop species, the combinations *A. indica* + *C. cajan*, *A. indica* + *P. typhoides* and *D. sissoo* + *P. typhoides* possessed significantly higher ($p = 0.01$) AM colonization. In the same model, rhizosphere soil of the tree species in combinations *G. arborea* + *C. cajan* and *P. pinnata* + *C. cajan* contained higher AM spore number compared to other combinations (**Figure 4**). In two strata plantations (**Figure 5**) three categories of combinations were recognized: 1) each of the plant in the combination possessed high mycorrhizal association (e.g. *G. arborea* + *P. pinnata* and *T. grandis* + *L. leucocephala*, 2) only one plant of the combination possessed high mycorrhizal association (e.g. *A. indica* + *P. embilica* and D. *strictus* + *T. grandis*), and 3) none of the plants in the combination possessed high mycorrhizal association (e.g. *A. lebbeck* + *A. catechu* and *T. bellirica* + *G. arborea*). In two strata plantation, the best combinations with high mycorrhizal association were *G. arborea* + *P. pinnata* and *T. grandis* + *L. leucocephala*.

AM spore number was higher in the rhizosphere soils of *P. pinnata* and *G. arborea* when grown together on the dumps (**Figure 5**). In other combinations, either both the plants or one of them possessed lesser degree of AM association. The spore number was higher in the rhizosphere soil of *P. pinnata* as compared to other combinations. *A. lebbeck* + *A. catechu, P. pinnata* + *T. bellirica* and *T. bellirica* + *G. arborea* were a few of other combinations having poor AM spore counts in their rhizosphere.

Generally, the AM colonization was higher in the roots of leguminous tree species grown with non-leguminous ones in combination (**Figure 5**). The examples of such combinations were: *T. grandis* + *L. leucocephala, G. arborea* + *P. pinnata* and *D. strictus* + *T. grandis.* A moderate to high AM colonization was recorded in *P. pinnata* for all the combinations tested. Low mycorrhizal colonization was recorded for *A. lebbeck* + *A. catechu* and *T. bellirica* + *G. arborea* combinations.

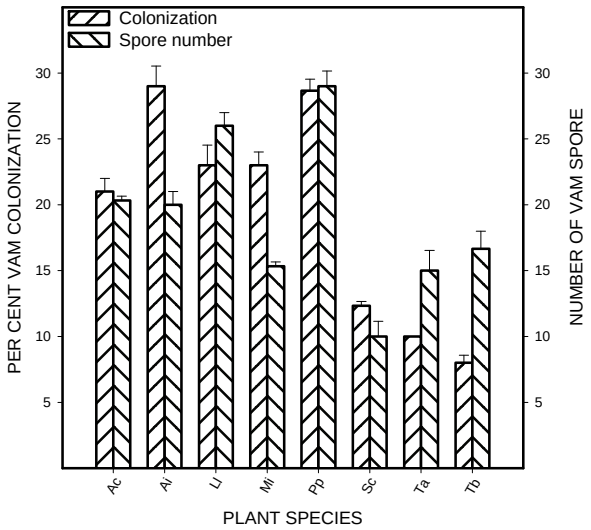

Figure 1. VAM association in plant species grown at slopes by direct see ding at revegetion medel site.

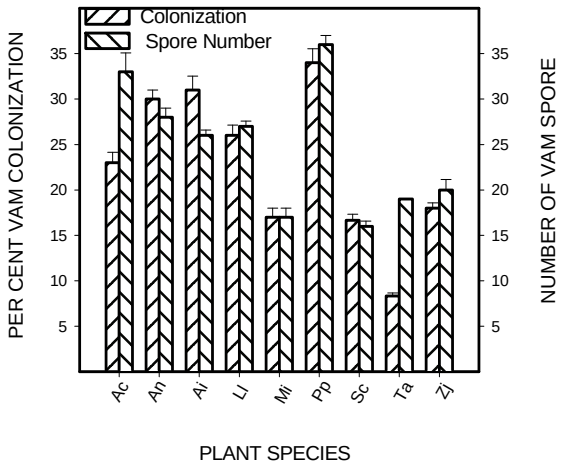

Figure 2. VAM association in plant species grown at flat surface by direct seeding at revegetation model site.

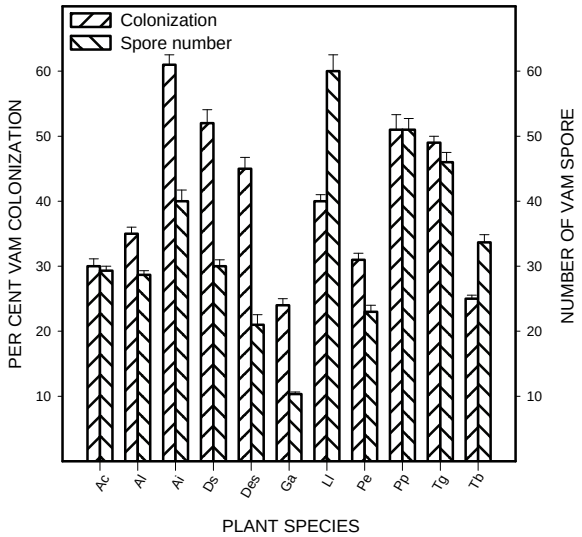

Figure 3. VAM association in plant species in monocuiture at revegetation medel site.

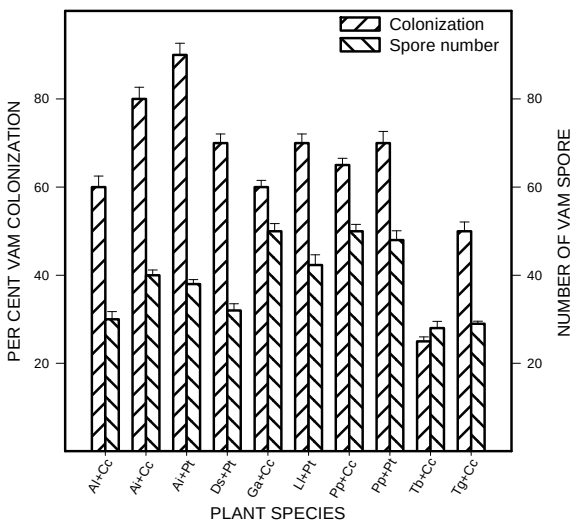

Figure 4. VAM association in plant species planted along with crop species at revegetation model site.

No significant correlation could be established between AM colonization and the spore number. In *T. grandis* (grown with *D. strictus*), *P. embilica* (grown with *A. indica*), the spore count in the rhizosphere was high but the AM colonization was low. However, in case of *A. indica* (with *P. emblica*), *P. pinnata* (with *A. catechu*), *L. leucocephala* (with *T. grandis*) and *T. bellirica* (with *P. pinnata*), the spore count was low in the rhizosphere in contrary to high AM colonization in roots. In some species such as *P. emblica* (with *A. indica*), *T. grandis* (with *L. leucocephala*), *A. lebbeck* (with *A. catechu*) and *T. bellirica* (with *G. arborea*), the AM colonization as well as spore number both were low. In a few plants, AM colonization as well as spore number was high. These were *G. arborea* and *P. pinnata* (grown together) and *P. pinnata* (grown along with *T. bellirica*). Two combinations namely *A. lebbeck* + *A. catechu* and *T. bellirica* + *G. arborea* possessed low level of AM association.

5. Discussion

The present study involved various RMS models for assessment of mycorrhizal status of the plants. AM colonization was poor in plants grown by seeding on overburden both at flat surface and slopes. This may be attributed to poor emergence of roots, as a result of erosion, the detrimental factor affecting survival of plants and poor presence of AM as well. This is supported by the fact that at slopes, where soil erosion was severe, the AM-plant association in plants was poor. The nursery raised seedlings as monoculture favored mycorrhization than the direct seeding. High AM colonization was recorded in *P. pinnata*, *L. leucocephala* and *D. strictus* in two strata plantation. Seeding or planting of species not only controls erosion but also enhances species diversity and speeds up succession that meets the revegetation goal. Nicholasan and McGinnies [21] reported that establishment of good plant cover can stabilize mine spoil and consequently improve soil conditions to promote plant succession [22]. Direct seeding of plants has been recommended in many reports [23-25]. There are reports that seedling growth and survival of tree species is affected by seeding of grasses and legumes [26]. The grasses are beneficial in checking erosion while legumes improve soil nutrient status. AM fungi benefit plant establishment and survival in many ways in degraded lands [27-30], and restoration programs with application mycorrhizal technology have been successful [31-32].

Agroforestry is the collective term for land use system wherein woody perennials are grown in association with agricultural herbaceous plants, following spatial arrangement or temporal sequence that facilitates both ecological and economic interactions between the tree and non-tree components. In mixed plantations, it appeared that leguminous plants were more advantageous than non-leguminous trees except *A. indica*. Tree + crop plantation appeared to be the best model in terms of mycorrhizal technology at least for the selected species. *A. indica*, *P. pinnata*, *L. leucocephala* and *A. catechu* were most effective in attracting luxuriant mycorrhizae (even when seeded directly), and thus can be used as the suitable rehabilitating species in such degraded ecosystems. It seems that seeding with grasses and leguminous forbes increased AM inoculums, as these grew luxuriantly with fibrous roots that favored mycorrhizal association. Leguminous shade trees contribute substantial N to the understory crop growth and also favors N uptake by tropi-

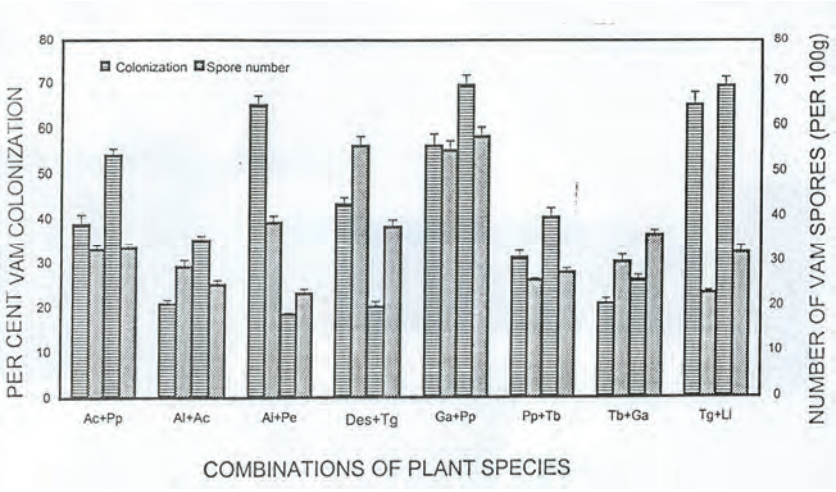

Figure 5. VAM association in plant species grown in two strata plantation at revegetating model site. Abbreviationa: Ac, *A*. catechu; Al, *A*. lebbeck; Ai, *A*. indica; Ds D. *sissoo*; Des, *D*. strictus; Ga, *G*. arborea; Li, *L lencocephala*; Pe, *P*. emblicar; Pp, *P. pinnata*; Tg, *T. grandis*, Tb, *T. bellerica.*

cal grasses [33-34]. Further, the results confirm the fact that mycorrhizae also help the plant-soil-plant system by inter-bridging between the roots of different plants [35-37].

Most legumes are fairly responsive to and extensively colonized by mycorrhizae especially in soils where an insufficiency of available P limits plant growth. Hence, the influence of mycorrhizae on legumes is potentially greater over any other group because of alleviation of P-stress by symbiotic fungi and indirectly by enhancing N status soil contributed by the legumes. Since plants do not contain their own polyphosphate hydrolase, they rely on the activity of soil microorganisms to release free phosphate from minerals or organic P resources. Mycorrhizal plants can utilize more phosphorus than the non-mycorrhizal ones, mainly from the same soluble phosphate pool as AM fungi harbor phosphate transfer [38]. Davies and Call [39] reported that AM significantly enhance the nutritional status in perennial grasses growing at lignite overburden. The successful restoration depends on the capacity of the plants to capture resources at an early stage. On degraded lands, which may be droughty, nutritionally poor or otherwise stressed, there exists only a brief period favorable period for plant growth and the plants which do not establish within that time window fail to survive.

Jeffries *et al.* [40] also supported the persistence of an acceptable amount of weeds within crops; providing a reservoir of mycorrhizal inoculum. Established mycorrhizal vegetation can facilitate the probability or extent of mycorrhizal infection of seedlings and thus mycorrhizal interaction among distantly related plants might be of particular ecological interest, as this may permit early succession of plants [41].

6. Acknowledgements

The research project was funded by the Ministry of Coal, Government of India through Central Mine Planning and Design Institute Limited (CMPDI), Ranchi, India. The financial assistance in the form of Junior and Senior Research Fellowship is gratefully acknowledged.

7. References

[1] E. G. O' Neill, R. V. O' Neill and R. J. Norby, "Hierarchy Theory as a Guide to Mycorrhizal Research on Large-Scale Problems," *Environmental Pollution*, Vol. 73, No. 3-4, 1991, pp. 271-284.

[2] B. F. Rodrigues, "Diversity of Arbuscular Mycorrhizal (AM) Fungal Species from Iron Ore Mine Wastelands in Goa," *The Indian Forester*, Vol. 126, No. 11, 2000, pp. 1211-1215.

[3] W. W. Mitchell, "Revegetation Research on Coal Mine Overburden Materials in Interior to Southeastern Alaska," *Agriculture and Forest Experimental Station Bulletin*, Vol. 79, 1987, pp. 72-86.

[4] W. W. Emerson, R. C. Foster and J. M. Oades, "Organo-Mineral Complexes in Relation to Soil Aggregation and Structure," In: P. M. Huang and M. Schnitzer, Eds., *Interactions of Soil Mineral with Natural Organics and Microbes*, *SSSA Special Publication*, Madison, Vol. 17, 1986, pp. 521-548.

[5] D. C. Coleman, "The Role of Microfloral and Faunal Interactions in Affecting Soil Processes. In: M. J. Mitchell and J. P. Nakes, Eds., *Microfloral and Faunal Interactions in Natural and Agro-Ecosystems*, W. Junk Publishers, Boston, 1986, pp. 317-348.

[6] T. T. Elliot and D. C. Coleman, "Let the Soil Work for us," *Ecological Bulletin*, Vol. 39, No. 2-3, 1988, pp. 23-32.

[7] R. M. Miller and J. D. Jastrow, "Mycorrhizal Fungi Influence Soil Structure," In: Y. Kapulnik and D. D. Douds, Eds., *Arbuscular Mycorrhizas*: *Physiology and Function*, Kluwer Academic, Dordrecht, The Netherlands, 2000, pp. 3-18.

[8] M. C. Gonzalez-Chavez, R. Carrillo-Gonzalez, S. F. Wright and K. Nichols, "The Role of Glomalin, a Protein Produced by Arbuscular Mycorrhizal Fungi in Sequestering Potentially Toxic Elements," *Environmental Pollution*, Vol. 130, No. 3, 2004, pp. 317-323.

[9] S. F. Wright and A. Upadhyaya, "A Survey of Soils for Aggregate Stability and Glomalin, a Glycoprotein in Produced by Hyphae of Arbuscular Mycorrhizal Fungi," *Plant and Soil*, Vol. 198, No. 1, 1998, pp. 97-107.

[10] T. Selvaraj, P. Chellapan, Y. J. Jeong and H. Kim, "Occurrence and Quantification of Vesicular Arbuscular Mycorrhizae Fungi in Industrial Polluted Soils," *Journal of Microbiology and Biotechnology*, Vol. 15, No. 1, 2005, pp. 147-154.

[11] T. E. Pawlowska, L. C. Rufus, M. Chin and I. Charvat, "Effects of Metal Phytoextraction Practices on the Indigenous Community of Arbuscular Mycorrhizal Fungi at a Metal Contaminated Landfill," *Applied Environmental Microbiology*, Vol. 66, No. 6, 2000, pp. 2526-2530.

[12] A. A. Meharg, "The Mechanistic Basis of Interactions between Mycorrhizal Associations and Toxic Metal Cations," *Mycological Research*, Vol. 107, No. 11, 2003, pp. 1253-1265.

[13] F. Quizad, U. Hilderbrandt, E. Schmelzer and H. Bothe, "Differential Gene Expressions in Arbuscular Mycorrhizal-Colonized Tomato Grown under Heavy Metal Stress," *Journal of Plant Physiology*, Vol. 162, No. 3, 2005, pp. 634-649.

[14] K. Vogel-Mikus, P. Pongrac, P. Kump, M. Necemer and M. Regvar, "Colonization of a Zn, Cd and Pb Hyperaccumulator *Thlaspi praecox* Wulfen with Indigenous Arbuscular Mycorrhizal Fungal Mixture Induces Changes in Heavy Metal and Nutrient Uptake," *Environmental Pollution*, Vol. 139, No. 2, 2006, pp. 362-371.

[15] K. Haselwandter, "Soil Microorganisms, Mycorrhiza and Restoration Ecology," In: K. M. Urbanska, N. R. Webb and P. J. Edwards, Eds., *Restoration Ecology and Sustainable Development*, Cambridge University Press, Cambridge, 1997.

[16] P. W. Arnold, A. Gildon and D. L. Rimmer, "The Use of Soil in the Reclamation of Coal Mine Wastes," *Proceedings of the Symposium on the Reclamation, Treatment and Utilization of Coal Mining Wastes*, Durham, England, 1984, pp. 26.1-26.10.

[17] J. W. Gerdemann and T. H. Nicolson, "Spores of Mycorrhizal *Endogone* Species Extracted from Soil by Wet Sieving and Decanting," *Transactions of British Mycological Society*, Vol. 46, No. 2, 1963, pp. 235-244.

[18] B. A. Daniels and H. D. Skipper, "Methods for the Recovery and Quantitative Estimation of Propagules from Soil," In: N. C. Schenck, Ed., *Methods and Principles of Mycorrhizal Research*, *American Phytopathological Society*, Vol. 29, St. Paul, Minnesota, 1982, pp. 29-36.

[19] P. P. Kormanik, W. C. Bryan and R. C. Schultz, "Increasing Endomycorrhizal Fungus Inoculum in Forest Nursery Soil with Cover Crops," *South African Journal of Applied Forestry*, Vol. 4, 1980, p.151.

[20] J. M. Phillips and D. S. Hayman, "Improved Procedures for Clearing and Staining Parasitic and Vesicular Arbuscular Mycorrhizal Fungi for Rapid Assessment of Infection," *Transactions of British Mycological Society*, Vol. 55, 1970, pp. 158-161.

[21] E. J. Nicholasan and W. J. Mc Ginnies, "An Evaluation of Seventeen Grasses and Two Legumes for Revegetation of Soil and Spoil on a Coal Strip-Mine," *Journal of Range Management*, Vol. 35, No. 1, 1982, pp. 288-293.

[22] W. M. Schafer and G. A. Nielsen, "Soil Development and Plant Succession on 1-to-50-yr-Old Strip Mine Spoils in Southern Montana," In: M. K. Wali, Ed., *Ecology and Coal Resource Development*, Vol. 2, Pergamon Press, New York, 1979, pp. 541-549.

[23] W. H. Davidson, "Direct Seeding for Reforestation," In: *Trees for Reclamation*, *USDA Forest Service General Technical Report*, NE-61, 1980, pp. 93-97.

[24] R. F. Wittwer, S. B. Carpenter and D. H. Graves, "Survival and Growth of Oakes and Virginia Pine Three Years after Direct Seeding on Mine Spoils," In: *Proceedings of the Symposium on Surface Mining Hydrology, Sedimentology and Reclamation*, University of Kentucky, Lexington, Kentucky, 1981, pp. 1-4.

[25] J. L. Creighton, R. N. Muller and R. F. Wittwer, "Biomass and Nutrient Assimilation of Intensively-Cultured Black-Locust on Eastern Kentucky Mine Spoil," *Proceedings of the Symposium on Surface Mining, Hydrology, Sedimentology and Reclamation*, University of Kentucky, Lexington, Kentucky, 1983, pp. 503-508.

[26] T. R. Cunningham and R. F. Wittwer, "Direct Seeding of Oaks and Black Walnut on Mine Soils in Eastern Kentucky," *Reclamation and Revegetation Research*, Vol. 3, 1984, pp. 173-184.

[27] M. C. Brundrett, "Mycorrhizas in Natural Ecosystem," *Advances in Ecological Research*, Vol. 21, 1991, pp. 171-173.

[28] A. Varma, "Ecophysiology and Application of Arbuscular Mycorrhizal Fungi in Arid Soils," In: A. Varma and B. Hock, Eds., *Mycorrhiza, Structure, Function, Molecular Biology and Biotechnology*, Sprintger-Verlag, Berlin, Heidelberg, 1995, pp. 561-591.

[29] A. Gaur and A. Adholeya, "Prospects of AM Fungi in Phytoremediation of Heavy Metal Contaminated Soils: Mini Review," *Current Science*, Vol. 86, No. 4, 2003, pp. 528-534.

[30] R. Raghuwanshi and R. S. Upadhyay, "Performance of Vesicular-Arbuscular Mycorrhizae in Saline-Alkali Soil in Relation to Various Amendments," *World Journal of Microbiology and Biotechnology*, Vol. 20, No. 1, 2004, pp. 1-5.

[31] D. H. Marx, "Trials and Tribulations of an Ectomycorrhizal Fungus Inoculation Program," *Proceedings of 6th North American Conference on Mycorrhizae*, Forest

Research Laboratory, Oregon State University, Corvallis, 1985, pp. 62-63.

[32] C. E. Cordell, "The Application of *Pisolithus tinctorius* Ectomycorrhizae in Forest Land Management," *Proceedings of* 6*th North American Conference on* "*Mycorrhizae*", Forest Research Laboratory, Oregon State University, Corvallis, 1985, pp. 69-72.

[33] C. C. Wong and J. R. Wilson, "The Effect of Shading on the Growth and Nitrogen Content of Green Panic and Sirato in Pure and Mixed Swards Defoliated at Two Frequencies," *Australian Journal of Agricultural Research*, Vol. 31, No. 2, 1980, pp. 269-285.

[34] F. I. Eriksen and A. S. Whitney, "Effect of Light Intensity on Growth of Some Tropical Forage Species 1. Interactions of Light Intensity and Nitrogen Fertilization on the Six Forage Grasses," *Agronomy Journal*, Vol. 73, No. 3, 1981, pp. 427-433.

[35] E. I. Newman, "Mycorrhizal Links between Plants: Their Functioning and Ecological Significance," *Advances in Ecological Research*, Vol. 18, 1988, pp. 243-270.

[36] E. I. Newman and W. R. Eason, "Cycling of Nutrients from Dying Roots to Living Plants Including the Role of Mycorrhizas," In: L. Clarholm and L. Bergstrom, Eds., *Ecology of Arable Land*, Kluwer, Dordrech, 1989, pp. 133-137.

[37] W. R. Eason and E. I. Newman, "Rapid Cycling of Nitrogen and Phosphorus from Dying Roots of *Lolium perenne*," *Oecologia*, Vol. 82, No. 4, 1990, pp. 432-436.

[38] T. Selvaraj and P. Chellapan, "Arbuscular Mycorrhizae: A Diverse Personality," *Journal of Central European Agriculture*, Vol. 7, No. 2, 2006, pp. 349-358.

[39] F. T. Davies, Jr. and C. A. Call, "Survival and Growth of Mycorrhizal Woody Revegetation Species in Texas Lignite Overburden," *Proceedings of the* 7*th North American Conference on Mycorrhizae in the Next Decade*, Gainesville, Florida, 1987, p. 148.

[40] P. Jeffries, S. Gianinazzi, S. Perotto, K. Turnau and J. M. Barea, "The Contribution of Arbuscular Mycorrhizal Fungi in Sustainable Maintenance of Plant Health and Soil Fertility," *Biology and Fertility of Soils*, Vol. 37, 2003, pp. 1-16.

[41] I. A. Dickie, J. Oleksyn, P. B. Reich, P. Karolewski, R. Zytowiak, A. M. Jagodzinski and E. Turzanska, "Soil Modification by Different Tree Species Influences the Extent of Seedling Ectomycorrhizal Infection," *Mycorrhizae*, Vol. 16, No. 2, 2006, pp. 73-79.

Engineering, 2010, 2, 690-697
doi:10.4236/eng.2010.29089 Published Online September 2010 (http://www.SciRP.org/journal/eng)

Development of Multi-Channel Data Logger for Indoor Environment

Anuj Kumar, Indu Prakash Singh, Suresh Kumar Sud
Instrument Design Development Centre, Indian Institute of Technology Delhi, Hauz Khas, India
E-mail: *anujkumariitd@gmail.com,{ipsingh, sksud}@iddc.iitd.ac.in*
Received March 12, 2010; *revised June* 2, 2010; *accepted June* 16, 2010

Abstract

Environment monitoring has become a necessity because of global warming and climate change. All across the globe researchers are trying to monitor the environmental parameters of temperature, humidity and pollutants gases mere precisely in real time. Sensing system using sensor arrays has been developed to monitor indoor environment, however, these systems are costly and have not gained wide acceptance. Precise monitoring of building environment has a huge potential in terms of energy savings. In this paper, an effort has been made to develop a 4-channel energy efficient and low cost data logger for indoor environment. The Data logger is proposed to be developed with the use of PIC 18F4458. Real Time Clock and EEPROM are interfaced for sampled data with the instance of sampling time and month/date/year; these sampled data will be stored in the EEPROM to the note pad tabular form with the help of graphical user interface (GUI).

Keywords: Gas Sensors, GUI, (Real Time Clock) RTC, ADC, Smart Transducer Interface

1. Introduction

Indoor environment and built-architecture are closely associated. The built environment affects indoor physical environments, and subsequently health and quality of life of occupants. There is evidence showing the pathways and mechanisms by which the built environment affects health and factor associated with specific aspects of physical and mental health. The problem has become acute in recent past because of the rapid industrial growth in last half century and has led to change in lifestyles (Become more dependent on indoor environment) [1]. The main factors of the environmental condition are the air quality and environmental parameter of the inside unconditioned environment. Across the world indoor air quality monitoring is gaining hotspot in present research works because recent study has put forth that 30 – 40% of total natural resources are exploited by the buildings and almost 50% of energy resources is used to condition buildings in industrialized countries. The reality is that indoor air can be up to 10 times more polluted than outdoor air [2]. The major contaminants of indoor environment pollution are CO_2, CO, O_3, SO_2 and NO_2. Many researchers are collect the data for different techniques, in different fields are facing similar difficulty in data collection *i.e.*, needs a user friendly system is able to collect data from the work place and buildings environment. Pardo *et al.* developed a gas measurement system based on the IEEE 1451.2 standard. They have used the 4-gas sensors (tin oxide), 1-temperature and 1-humidity sensor; this prototype system will be work as electronic nose [3]. Camara *et al*. developed a STIM (smart transducer interface module) based on the IEEE 1451 standard. This prototype system will be work with a lot of different transducers without the necessity of change of the control hardware and software [4].

Available technologies for sensing these environmental parameters are developed by Onseat HOBO, Spectrum Technologies (Watch Dog weather conditions), TandD, Telaire (Wireless Monitoring Systems), Testo, Log Tag, Measurement Computing Corporation, Monarch Instruments, MSR Electronics GmbH, P3 International, Quality Thermistor, S3 Crop, Sensaphone, Sansatronics, Lascar, ICP, Graphtech, Extech Instruments, Dickson, Dent Instruments, Davis, ACR System Inc, 3M International, and Acumen [5].

But we found the developed system is not suitable for the real time monitoring of the indoor environment and

will be required to store the information and data collection for the long duration.

To focus on this problem we are trying to develop a low cost and energy efficient multi channel data logger for indoor environment. We face only 4-parameter such as temperature, relative humidity, SO_2, and NO_2. It can be summarized as follows-interface of LCD (to display the output of various modules), RTC and EEPROM with microcontroller and interface of the data logger to the personal computer by using the serial (RS-232) port, minimization of power consumption in order to enhance battery life and preparing the user friendly graphical user interface in visual language to operate the data logger.

2. Sensors

A sensor is a device that measures a physical quantity and converts it into an equivalent analog or digital signal which can be read by an observer or by an instrument. Monitoring of an indoor environment involves sensing the changes occurring inside it. The parameters which are of importance are the temperature, relative humidity, and concentration level of air pollutant SO_2, and NO_2 inside the building [6,7]. In this paper we have used a p type or n type resistive based semiconductor gas sensor.

A gas sensor detects particular gas molecules and produces an electrical signal whose magnitude is proportional to the concentration of the gas [8]. No single type of gas sensor is 100% selective to a single gas. A good sensor is sensitive to the measured quantity but less sensitive to other quantities. Available gas sensors are based on five basic principles. These can be electrochemical, infrared, catalytic bead, photo ionization and solid-state [9,10]. We have selected these sensors because they produce a strong signal for the selected variable especially at high gas concentrations with adequate sensitivity. They have a fast response time, high stability, long life, low cost, low dependency on humidity, low power consumption, and compact size [8]. **Table 1** represents the Specifications of the Sensors Used in the Multi-Channel Data Logging System and **Table 2** represents the measurement range of the developed system.

3. Signal Processing of the Sensors

Four sensors along with their signal conditioning circuit are used to sense the desired parameter. One is temperature, second is humidity, third is SO_2, and fourth is NO_2. Signal conditioning circuit for that sensor needs to be connected externally. In software we can select any of the analog channel and hence the sensor. Interfacing of temperature, humidity, SO_2, and NO_2 sensor with microcontroller PIC 18F4458 is as follows.

Table 1. Specifications of the sensors used in the multi-channel data logging system [8-10].

Sl. No.	Sensor Name/	Manufacturer	Range	Sensitivity	Response Time
1.	LM35CZ Precision Temp. sensor	National semiconductor, USA	−40 to 110°C	10 mV/°C	< 2 sec
2.	HIH–4000 Humidity sensor	Honeywell, USA	0 to 100%	0.60 pF/%RH	15 sec
3.	SO_2-BF	Alphasense, UK	0 to 100 ppm	300 to 440 nA/ppm (20 ppm SO_2)	< 30 sec
4.	NO_2-A1	Alphasense, UK	0 to 20 ppm	−400 to −750 nA/ppm (10ppm NO_2)	< 40 sec

Table 2. Represents the measurement range of the developed system.

Sl. No.	Measured	Minimum Range	Maximum Range
1.	Temperature	0°C	70°C
2.	Relative Humidity	0%	100%
3.	SO_2	0 ppm	3 ppm
4.	NO_2	0 ppm	2.5 ppm

3.1. Temperature Sensor

National semiconductor's LM 35 IC has been used for sensing the temperature. It is an integrated circuit sensor that can be used to measure temperature with an electrical output proportional to the temperature (in °C). The temperature can be measured more accurately with it than using a thermistor. The operating circuit of temperature sensor is shown in **Figure 1**. The output voltage of LM 35 is converted to temperature in °C is [10] as shown in Equation (1).

$$Temp.(°C) = \left(V_{out} \times 100\right) / 7°C \quad (1)$$

V_{OUT} = output voltage of the sensor (volts)

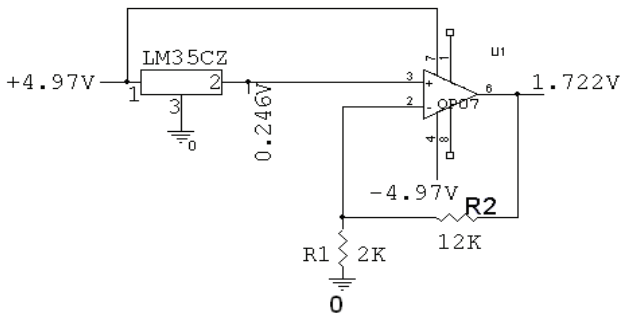

Figure 1. Operating circuit of temperature sensor (LM35 CZ).

3.2. Humidity Sensor

The sensor circuit develops a linear voltage vs. RH output that is ratio metric to the supply voltage. That is, when the supply voltage varies, the sensor output voltage follows in the same proportion. It can operate over a supply voltage range between 4.0 V to 5.8 V. At 5 V supply voltage (at room temperature) *i.e.*, the output voltage ranges from 0.8 to 3.9 V as the humidity varies from 0% to 100% (non-condensing). The humidity sensor functions with a resolution of up to 0.5% of relative humidity (RH), with a typical current draw of only 200 μA, the HIH-4000 series is ideally suited for low drain, battery operated systems. The pin configuration of humidity sensor is shown in **Figure 2**. The change in the RH of the surroundings causes an equivalent change in the voltage output. The output is an analog voltage proportional to the supply voltage. Consequently, converting it to relative humidity (RH) requires that both the supply and sensor output voltages (At 25°C) [10] as shown in Equation (2).

$$RH = \left(\left(V_{out} / V_{supply}\right) - 0.16\right) / 0.0062 \quad (2)$$

RH = Relative humidity (%); V_{supply} = Input voltage

3.3. Operating Circuit of the SO_2 and NO_2 Sensor

The SO_2 and NO_2 sensor operating circuit is shown in **Figure 3**. In general the output of the IC1 is connected to the microcontroller pin AN2 and AN1 respectively [9].

4. Analog to Digital Conversion and Interfacing of LCD with Microcontroller

We are using the on chip analog to digital converter which is on the microcontroller PIC 18F4458. This analog to digital converter is having the 12 bit resolution with programmable acquisition time. It is sensing the analog signal from the sensor at the variable sampling rate (1 sec - 1 hour), the sensed value is converted to its digital equivalent. This digital value is displayed on the LCD (liquid crystal display) which is interfaced to the microcontroller [11-18]. Circuit diagram of LCD interfacing to the microcontroller is shown **Figure 6**.

5. Interfacing of Real Time Clock with Microcontroller

The DS1307 operates as a slave device on the I^2C bus. Access is obtained by implementing a START condition and providing a device identification code followed by a register addresses. Subsequent registers can be accessed sequentially until a STOP condition is executed. When V_{CC} falls below 1.25 V_{BAT}, the device terminates an access in progress and resets the device address counter.

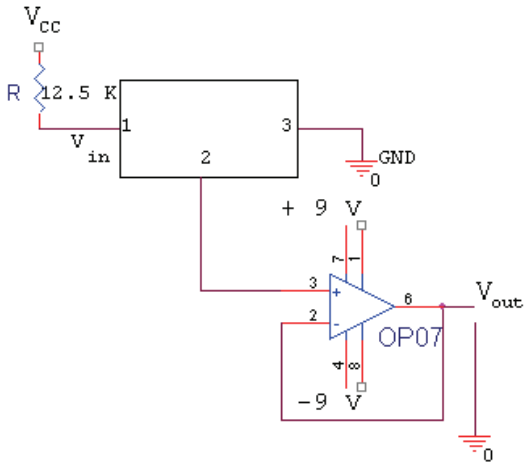

Figure 2. Operating circuit of humidity sensor (HIH4000).

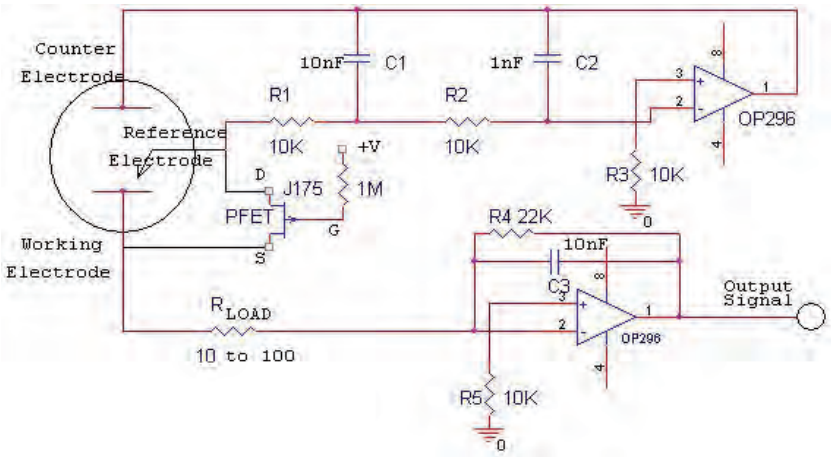

Figure 3. Operating circuit of the SO_2 and NO_2 gas sensor [9].

Inputs to the device will not be recognized at this time to prevent erroneous data from being written to the device from an out of tolerance system. When V_{CC} falls below V_{BAT}, the device switches into a low-current battery-backup mode. Upon power-up, the device switches from battery to V_{CC} when V_{CC} is greater than V_{BAT} +0.2 V and recognizes inputs when V_{CC} is greater than 1.25 V_{BAT}. **Figure 6** shows the interfacing of real time clock (RTC). We are using the DS1307 real time clock which is having the following features - real time clock counts Hours, Minutes, Seconds, of the Month, Day, Year with Leap-Year Compensation valid up to 2100, 56-Byte, Battery-Backed, Nonvolatile (NV) RAM for data storage, I^2C serial interface, programmable square-wave output signal, automatic power fail detect and switch circuitry, consumes less than 500 nA in battery-backup mode oscillator running, and temperature range −40°C to +85°C [14,15].

6. Interfacing of EEPROM with Microcontroller

The EEPROM will store the digital value which is coming from analog to digital converter. We will require the 52.73 MB of EEPROM if we are sampling all analog channels at the rate of 1 sample/Second. We are using the EEPROM AT24C256 of ATMEL. This will store the sample data at different instants. This EEPROM having the following features - low voltage and standard voltage operation 5.0 (V_{CC} = 4.5 V to 5.5 V), 2.7 (V_{CC} = 2.7 V to 5.5 V), and 1.8 (V_{CC} = 1.8 V to 5.5 V); 1 MHZ (5 V), 400 KHZ (2.7 V) and 100 KHZ (1.8 V) compatibility, and 64-Byte page write mode [15,17,18]. **Figure 6** shows the interfacing of EEPROM. We are using the I^2C to interface the real time clock (RTC) and EEPROM to the microcontroller. The IC bus is the most popular of the 3 serial EEPROM protocols. **Figure 6** shows the typical pin out of an I^2C device, showing pins 1-3 as address pins A0, A1 and A2. Pin 4 is V_{SS}, or ground. Pin 5 is SDA, the data line. Pin 6 is SCL, the clock signal. Pin 7 is write protect, and pin 8 is voltage, or V_{CC}. Finally, many I^2C chips include address pins as an easy way to have multiple chips on a single bus while still only using two connections to the microcontroller [14].

7. PC Interfacing with Microcontroller Using RS232 Serial Communication

Personal computer is interfaced with PIC 18F4458 using MAX232. It is the IC used to convert the TTL logic level to the RS232 logic level. RS232 is the serial communication protocol that does not require the clock along with data lines. Two data lines are there one is T_X and another is R_X for serial communication. MAX432 has two receivers (converts RS-232 logic level to TTL logic) and two drivers (converts TTL logic to RS232 level). Following **Figure 6** shows the hardware interface of PIC with personal computer. Separate power supply has been provided because minimum power supply needed is 5 V and MAX232 consumes a lot of current for operation. External capacitors are required for internal voltage push to convert TTL logic level to RS232 level. For battery operated application MAX232 can be used as level converter instead of MAX232, it is low power consumption logic converter IC for RS232. It is pin compatible with MAX232 [14].

8. Graphical User Interface

A program interfaced that takes advantage of the computer graphics capabilities to make the program easier to use. In this paper, the GUI is one of the important parts it displays the data from microcontroller for data monitoring and analysis. However, the main objective is to display data received in graphical form. As a transducer detects and translate an analog signal, the data will go through a conversion at the ADC and become a digital format. This digital data is converted in a 12 bit data. This data will be stored to the EEPROM chip with the help of Visual Basic 6.0 software. Since the data used the serial RS232 communication, therefore an initialization needs to be done which are the baud rate, data bits, parity, stop bit and the COM port at the PC. The baud rate is the number of signal changes per second or transition speed between Mark (negative) and Space (positive) which range from 110 to 19200, data bits is the length of data in bit which has one least significant bit (LSB) and one most significant bit (MSB), the parity bit is an optional bit mainly for bit error checking. It can be odd, even, none Mark and Space. Stop bit is used to frame up the data bits and usually combined with the start bit. These bits are always represented by a negative voltage and can be 1, 1.5 and 2 stop bits. The commonly used setting to establish a serial RS232 communication is 9600 baud rate, none parity, 8 data bits, and 1 stop bit. As this paper relates with data collection, thus the data obtained from the microcontroller needs to be collected and saved. This can be done by using the GUI monitoring system where it automatically saves the data received in a note pad. The data being saved is the date and time during the data collected and data value it self. **Figures 4** and **5**, represents the graphical user interface and logged data in file [17,18].

9. Schematic of the Data Logger

Figure 6 shows, the full schematic diagram of the data logger for indoor environment. This data logger has four

embedded sensor module and other four channels are open to be used for the measurement of other environmental parameters.

10. Software Design of Data Logger

This subsection includes the software design for all the modules interfaced with PIC 18F4458. It covers complete software design for data logger. The programs have been written to the environmental parameters and concentration level of SO_2 and NO_2 gases are monitored for 24 hours and save the data of EEPROM corresponding to the time and date.

10.1. Programming Steps for I^{2}C Interface

I^{2}C is also bi-directional. This is implemented by an "Acknowledge" system or "ACK" system allows data to be sent in one direction to one item on the I^{2}C bus, than, that item will "ACK" to indicate the data was received. Normally, the master device controls the clock line, SCL. This line dictates the timing of all transfers on the I^{2}C bus. Other devices can manipulate this line, but they can only force the line low. This action means that item on the bus cannot deal with more data in to any device.

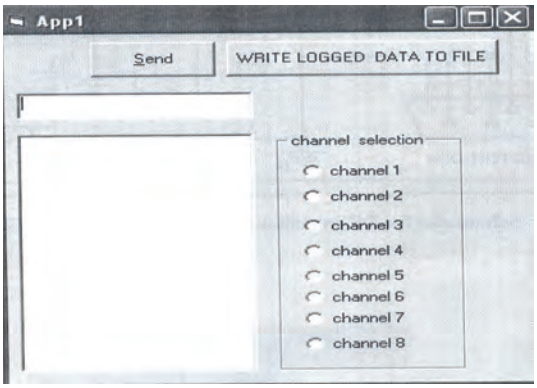

Figure 4. GUI for the data logger.

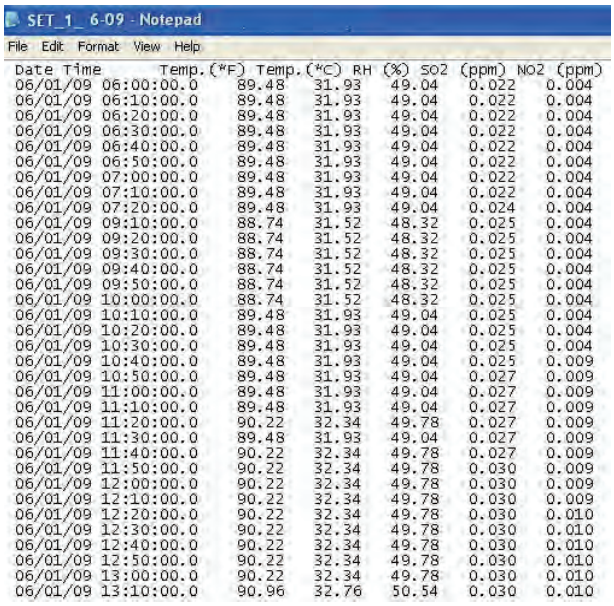

SET_1_6-09 - Notepad

File Edit Format View Help

Date Time	Temp. (*F)	Temp. (*C)	RH (%)	SO2 (ppm)	NO2 (ppm)
06/01/09 06:00:00.0	89.48	31.93	49.04	0.022	0.004
06/01/09 06:10:00.0	89.48	31.93	49.04	0.022	0.004
06/01/09 06:20:00.0	89.48	31.93	49.04	0.022	0.004
06/01/09 06:30:00.0	89.48	31.93	49.04	0.022	0.004
06/01/09 06:40:00.0	89.48	31.93	49.04	0.022	0.004
06/01/09 06:50:00.0	89.48	31.93	49.04	0.022	0.004
06/01/09 07:00:00.0	89.48	31.93	49.04	0.022	0.004
06/01/09 07:10:00.0	89.48	31.93	49.04	0.022	0.004
06/01/09 07:20:00.0	89.48	31.93	49.04	0.024	0.004
06/01/09 09:10:00.0	88.74	31.52	48.32	0.025	0.004
06/01/09 09:20:00.0	88.74	31.52	48.32	0.025	0.004
06/01/09 09:30:00.0	88.74	31.52	48.32	0.025	0.004
06/01/09 09:40:00.0	88.74	31.52	48.32	0.025	0.004
06/01/09 09:50:00.0	88.74	31.52	48.32	0.025	0.004
06/01/09 10:00:00.0	88.74	31.52	48.32	0.025	0.004
06/01/09 10:10:00.0	89.48	31.93	49.04	0.025	0.004
06/01/09 10:20:00.0	89.48	31.93	49.04	0.025	0.004
06/01/09 10:30:00.0	89.48	31.93	49.04	0.025	0.004
06/01/09 10:40:00.0	89.48	31.93	49.04	0.025	0.009
06/01/09 10:50:00.0	89.48	31.93	49.04	0.027	0.009
06/01/09 11:00:00.0	89.48	31.93	49.04	0.027	0.009
06/01/09 11:10:00.0	89.48	31.93	49.04	0.027	0.009
06/01/09 11:20:00.0	90.22	32.34	49.78	0.027	0.009
06/01/09 11:30:00.0	89.48	31.93	49.04	0.027	0.009
06/01/09 11:40:00.0	90.22	32.34	49.78	0.027	0.009
06/01/09 11:50:00.0	90.22	32.34	49.78	0.030	0.009
06/01/09 12:00:00.0	90.22	32.34	49.78	0.030	0.009
06/01/09 12:10:00.0	90.22	32.34	49.78	0.030	0.009
06/01/09 12:20:00.0	90.22	32.34	49.78	0.030	0.010
06/01/09 12:30:00.0	90.22	32.34	49.78	0.030	0.010
06/01/09 12:40:00.0	90.22	32.34	49.78	0.030	0.010
06/01/09 12:50:00.0	90.22	32.34	49.78	0.030	0.010
06/01/09 13:00:00.0	90.22	32.34	49.78	0.030	0.010
06/01/09 13:10:00.0	90.96	32.76	50.54	0.030	0.010

Figure 5. Representation of the logged data in file.

10.1.1. Writing to a I^{2}C Chip

The function of writing to the EEPROM is shown here as "Control IN", which represents putting the EEPROM in an "input" mode. Since we are only sending data to the EEPROM, we use the "Control IN" byte. We will use "Control OUT" later. **Figure 7** shows the display of data saver memory (data writing of the memory).

Next, the EEPROM acknowledges this byte; this is shown by the "A" after the byte. It is put on the next line to indicate this is transmitted by the EEPROM. Next the PIC microcontroller sends the address byte. The address byte contains the address of the location of the EEPROM; we want to write data. Since the address is valid the data is acknowledged by the EEPROM. Finally, we send the data we want to write. The data is then acknowledged by the EEPROM. When that finishes, we send a stop condition to complete the transfer. Remember the "STOP" is represented as the "T" block on the end. Once the EEPROM gets the "STOP" condition it will begin writing to its memory. The write will not occur until it receives the "STOP" condition.

10.1.2. Reading from an I^{2}C Chip

The transfer will use the "Control IN" byte to load the address into the EEPROM. This sends data to the EEPROM which is why we use the "Control IN" byte. Once the address is loaded, we want to retrieve the data. So, we send a "Control OUT" byte to indicate to the EEPROM that we want data from it. The EEPROM will acknowledge this and then send the data we requested. When we are done getting data, we send a "NACK" to tell the EEPROM that we do not want more data. If we were to send an ACK at this point, we could get the next byte of data from the EEPROM. Since we only want to read one byte, we send a "NACK". This is detailed in the specifications for the EEPROM. **Figure 8** shows the display of outcome data saver memory (data reading and save outcome data in note pad form).

10.2. Programming Steps for LCD Interface

10.2.1. LCD Module is Initialization and Configuration to Work in 4 Bit Module

Set RS = 0 to send command; send 0b0010 to data lines

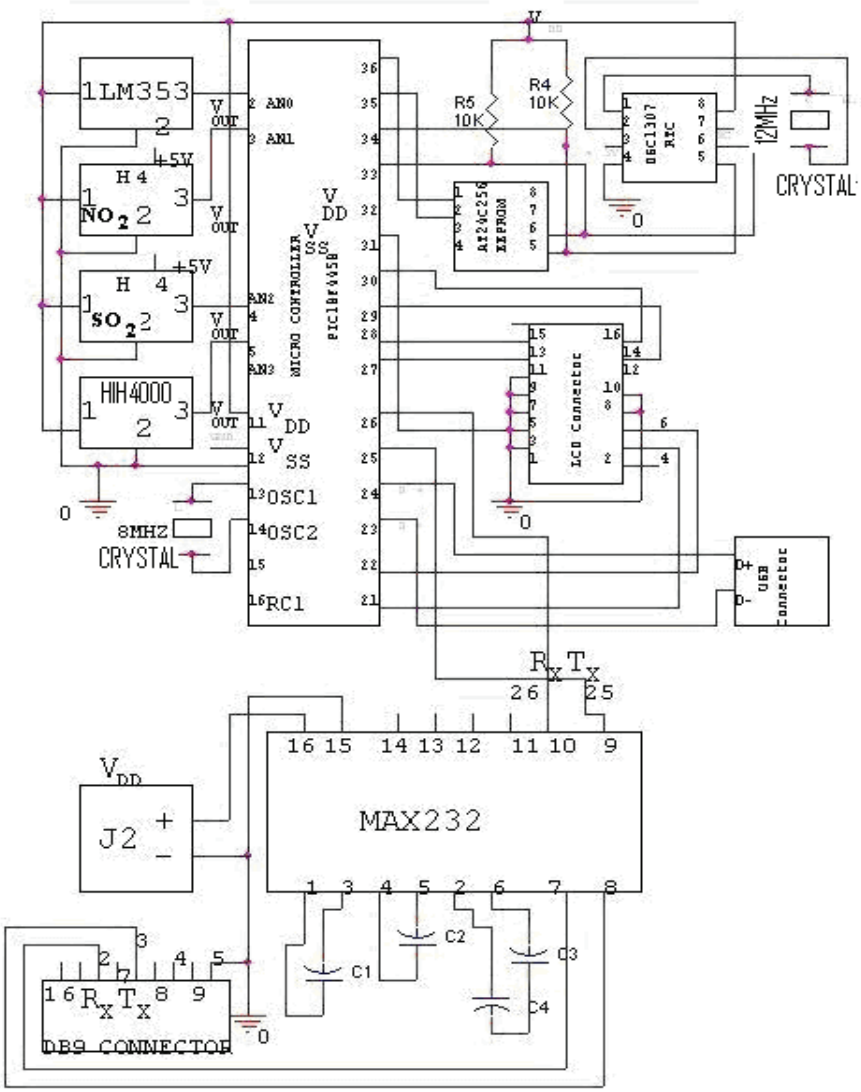

Figure 6. Full schematic of the data logger.

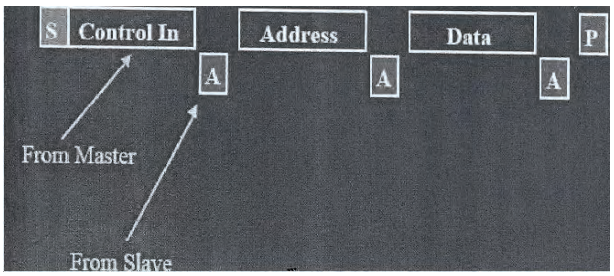

Figure 7. Display of data saver memory.

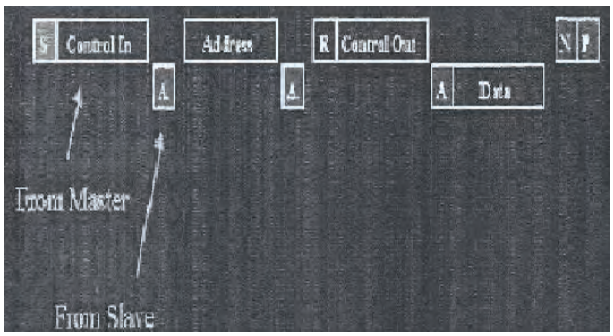

Figure 8. Display of outcome data saver memory.

three times with a delay of 2 ms; to send a byte on 4 data line. Send higher nibble first and give a RE pulse of 100 us at RE. Send a set of instruction one after another with a delay of 2 ms between each command to configure various setting as given in instruction set of LCD data-sheet. Send instruction set again.

10.2.2. Display a Character

Set RS = 1; send higher nibble at 4 data lines. Send 100uS RE pulse; send lower nibble at data lines. Send RE pulse; keep track of number of character already dis-

played on display panel using LCD count up. Go to line 2 or line 1 according to that.

10.3. Programming Steps for Sensor Data Collection

There are connected four sensors temperature, humidity, SO_2, and NO_2. Data is collected by the ADC inbuilt in PIC. ADC provides 10 bit of data after the conversion is completed.

10.3.1. Data Collection of Temperature Sensor

Select the analog channel AN0, alignment of bits for ADRESH and ADRESL, sampling frequency, Vref, power on the ADC module by setting ADCON0, ADCON1 and ADCON2 registers. Start A to D conversion by setting ADGO bit high and wait till ADIF flag will not indicate the completion of conversion and copy the results from ADRESH and ADRESL to variables.

10.3.2. Data Collection of Humidity Sensor

Select the AN3 and set other features of ADC as temperature sensor and after completion of conversion copies the result in variable.

10.3.3. Data Collection of NO_2 and SO_2 Sensor

Data collection from the NO_2 sensor needs following actions to be carried out 1) Selecting the analog channel AN_1, sampling frequency, and alignment of bits for ADRESH and ADRESL, 2) Vref and power on the ADC module by setting $ADCON_0$, $ADCON_1$ and $ADCON_2$ registers, 3) starting analog to digital conversion by setting ADGO bit high (wait till ADIF flag will not indicate the completion of conversion), and 4) copy of results from ADRESH and ADRESL to variables.

Now repeat the same process to collect the SO_2 data on the channel number AN_2.

11. Results and Discussion

Sensors module, EEPROM, RTC, and LCD have been successfully interfaced to the microcontroller. EEPROM is successfully storing the logged data with time and date tag. The sensors data is being displayed on LCD module. A simple GUI has been designed to store a logged data to a text file, so that it can be analyzed further. The developed system is lowest cost and energy efficient system. The power consumption of the developed system is minimum (< 250 mA).

12. Conclusions

We have developed a low cost, 12 bit resolution data logger and successfully measured temperature, humidity, and concentration of SO_2 and NO_2 gases. The GUI designed gives a lucratively look to the functioning of data logger. Initial results of the data logger are encouraging and we are working on to improve the GUI model as well as the accuracy of data logger.

13. Future Scope

We can improve the data logger by incorporating the wireless communication in it. There fore, by combining the term data acquisition and wireless communication, it becomes wireless data acquisition. This new innovation technology has become the trend for most industries and companies around the world to gather information due to its reliability and outstanding outcome. The advantage of this technology is that it did not use any physical components or wires to transfer the data obtained from sensor at transmitter side to the receiver side. As a result, an effective system is developed where it is not only removes all the conventional hardware and replace with a transceiver modem for data transfer but also a cost effective system as well. Moreover, the data transmission range can be extended into longer range depending on the transceiver modem capability. With this feature, information from the transducer could be transmitted faster and acts as an early alert in case of accident or disaster such as fire, food and earthquake. By modifying the GUI we can display the waveforms of the data on the computer console where as presently we are logging the data to the file. We also can incorporate the USB communication so that we can transfer the data at high data rates.

14. References

[1] E. Samakovlis, A. Huhtale, T. Bellander and M. Svartengren, "Valuinghealth Effects of Air Pollution Focus on Concentration-Response Functions," *Journal of Urban Economics*, Vol. 58, No. 2, 2005, pp. 230-249.

[2] J. D. Richard and G. S. Brager, "Thermal Comfort in Naturally Ventilated Buildings: Revisions to ASHRAE Standard 55," *Energy and Buildings*, Vol. 34, No. 6, 2002, pp. 549-561.

[3] A. Pardo, L. Camara, J. Cabre, A. Perera, X. Cano, S. Marco and J. Bosch, "Gas Measurement System Based on IEEE 1451.2 Standard," *Sensors and Actuators B*, Vol. 116, No. 1, 2006, pp. 11-16.

[4] L. Camara, O. Ruiz, A. Herms, J. Samitier and J. Bosch, "Automatic Generation of Intelligent Instruments for IEEE1451," *Measurement*, Vol. 35, No. 1, 2004, pp. 3-9.

[5] Microdaq, 3 March 2009. http://www.microdaq.com/data-logger/

[6] N. Ulivieri, C. Distante, T. Luca, S. Rocchi and P. Siciliano, "IEEE 1451.4: A Way to Standardize Gas Sensor,"

Sensors and Actuators B, Vol. 114, No. 1, 2006, pp. 141-151.

[7] D. D. Lee and D. S. Lee, "Environment Gas Sensors," *IEEE Sensors Journal*, Vol. 1, No. 3, 2001, pp. 214-215.

[8] N. Kularatna and B. H. Sudantha, "An Environmental Air Pollution Monitoring System Based on the IEEE 1451 Standard for Low Cost Requirements," *IEEE Sensors Journal*, Vol. 8, No. 4, 2008, pp. 415-422.

[9] http://www.alphasense.com

[10] http://be02.rsonline.com/web/search/searchBrowseAction.html?method=searchProducts&searchTerm

[11] G. Song, A. Song and W. Huang, "Distributed Measurement System Based on Network Smart Sensors with Standardize Interface," *Sensors and Actuators A*, Vol. 120, No. 1, 2005, pp. 147-153.

[12] T. Schneider, D. Richter, S. Doerner, H. Fritze and P. Hauptmann, "Novel Impedence Interface for Resonant High-Temperature Gas Sensors," *Sensors and Actuators A*, Vol. 111-112, No. 11, 2005, pp. 187-192.

[13] R. Luharuka and R. X. Gao, "A Microcontroller-Based Data Logger for Physiological Sensing," *IEEE Proceeding IMTCi* 2002, pp. 175-180.

[14] Data Acquisition Logging Circuits. http://www.hobby-projects.com/A/acquistions_data_circuits

[15] Data Sheet of Real Time Clock DS1307. http://www.glacialwanderer.com/_blog/blog2008/04_April/DS1307.pdf

[16] www.microchip.com

[17] Introduction to Data Acquisition. http://zone.ni.com/devzone/cocepted.nsf/webmain/AE2A7B85BD4785D586256F620066EFF4

[18] G. Mason, "A Handheld Data Acquisition System for Use in an Undergraduate Data Acquisition Course," *IEEE Transaction on Education*, Vol. 45, No. 4, 2008, pp. 388-393.

Engineering, 2010, 2, 698-704
doi:10.4236/eng.2010.29090 Published Online September 2010 (http://www.SciRP.org/journal/eng)

A General Calculating Method of Rotor's Torsional Stiffness Based on Stiffness Influence Coefficient

Danmei Xie[1], Wangfan Li[1], Ling Yang[2], Yong Qian[2], Xianbo Zhao[2], Zhigang Gao[3]
[1]*School of Power and Mechanical Engineering, Wuhan University, Wuhan, China*
[2]*Dongfang Turbine Co., Ltd., Deyang, China*
[3]*Daya Bay Nuclear Power Operation Ltd., Shenzhen, China*
E-mail: *dmxie@whu.edu.cn*
Received May 11, 2010; *revised July* 21, 2010; *accepted July* 23, 2010

Abstract

In order to develop a general calculating rotor's torsional stiffness based on stiffness influence coefficient for different rotor assembling, the calculation method of the torsional stiffness influence coefficient of equal thickness disc is researched in this paper at first. Then the torsional stiffness influence coefficient λ of equal thickness disc is fit to a binary curved face and a calculation equation is obtained based on a large quantity of calculating data, which lays the foundation for research on a general calculating method of rotor torsional stiffness. Thirdly a simplified calculation method for equivalent stiffness diameter of stepped equal thickness disc and cone disc in the steam turbine generators is suggested. Finally a general calculating program for calculating rotor's torsional vibration features is developed, and the torsional vibration features of a verity of steam turbine rotors are calculated for verification. The calculating results show that stiffness influence coefficient λ of equal-thickness disc depends on parameters of B and H, as well as the stiffness influence coefficient λ; and discs with complex structure can be simplified to equal-thickness discs with little error by using the method suggested in this paper; error can be controlled within 1% when equivalent diameter of stiffness is calculated by this method.

Keywords: Rotor, Disc, General Calculating Method, Torsional Stiffness, Stiffness Influence Coefficient

1. Introduction

The rotor's torsional vibration is one of the most important issues for safety operation of steam turbine generator units. And the electromagnetic torque of the generator and the driving torque of steam turbine reach to a balance state when the turbo-generator is in normal operation with certain load. Then the torque is stably distributed along the rotor. But once there are any disturbances caused by driving torque or electromagnetic torque, the balance will be destroyed, and inducing the rotor torsional vibration [1, 2]. Heavy torsional vibration will cause accidents and fatigue of the mechanical parts, so as to shorten the life span of the rotor, and even worse will cause the rotor broken. So the torsional vibration of rotor has aroused the attentions of the electricity production and the management departments widely [3,4].

Calculating the characteristics of rotor torsional vibration is one of the most important jobs in the strength design stage of turbine rotor, its accuracy has a great influence on the structure design and fabrication of the rotor and affects the prevention and control of the torsional vibration [5]. In solving the characteristics of rotor torsional vibration, one of the most important things is to define the torsional stiffness, because it will directly influence the results of the inherent frequency, vibration mode and critical speed and so on.

The integral-disc rotors have been widely used on the large steam turbine units. In general, there are two ways to solve the rotor stiffness, one is to calculate the exact solution with ANSYS software [6], and the other is to simplify the related disc at first and then to solve it with the empirical equation [7]. However, when the ANSYS is used, only one specific structure of rotor can be calculated at one time. When the structure of the rotor is changed, new modeling is needed, and as the modeling is so complex procedure that it wastes time. That is to say the versatility of this method is not so good. And the weakness for the second method is low precision. The purpose of this paper is to develop a general method to calculate the

characteristics of rotor's torsional vibration with a given data format for different kinds of rotor automatically, and with high accuracy. In this paper, the stiffness influence coefficient of single equal thickness disc is resolved at first. Then the torsional stiffness influence coefficient λ of equal thickness disc is fit to a binary curved face and calculation equation is corresponded with the curved face. Thirdly a simplified calculation method for calculating equivalent stiffness diameter of discs with complex structure as stepped equal thickness disc and cone disc in the steam turbine generators is researched. Finally the torsional vibration features of various steam turbine rotors are calculated for verification.

2. Calculation of Torsional Stiffness Influence Coefficient of Equal Thickness Disc

For the equal thickness disc in the integral-disc rotors (shown in the **Figure 1**), the disc and the shaft are integrated as a whole, the influence of the bulged part (or other complex parts) to stiffness must be considered when the stiffness of every section of the shaft is defined. The influence of the disc on the shaft is related to the thickness and the distance between the discs [8].

For lateral vibration, the influence of the disc on the shaft is usually represented by the cross-section polar moment of inertia I_n of every section on the shaft, and I_n is calculated by using the following equation:

$$I_n = \frac{I}{1-\frac{b}{L}(1-\lambda)} \tag{1}$$

where, I is the cross-section polar moment of inertia of the section shaft whose diameter is D, b is the thickness of the juncture of the disc and shaft, L is the length of the shaft, and λ is the influence coefficient considering the disc bending stiffness. λ is of monotonic decreasing with the ratio of b/D, so the influence of disc on stiffness can be

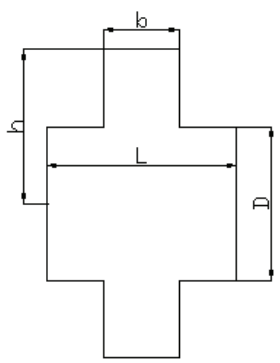

Figure 1. Longitudinal section of equal-thickness disc.

ignored when the ratio of b/D is very small (< 0.1), only the weight of the disc is considered.

To develop a general calculating method to calculate the characteristics of rotor's torsional vibration, the influence factors of the torsional stiffness influence coefficient λ is analyzed from following aspects, in the same way as lateral vibration:

1) I_n is supposed to be the cross-section polar moment of inertia of the shaft with the equivalent stiffness diameter D', and I, b, and L are calculated by using the disc physical dimension directly, so the torsional stiffness influence coefficient λ of a specific disc is solved according to (1).

2) As the stiffness influence coefficient λ of equal-thickness discs is mainly determined by the relative thickness B and the relative height H of the bulged part, where $B = b/D$, $H = (h-D/2)/(D/2)$. A large quantity of discs with different sizes are calculated, then their regularity is summarized and an equation about the λ is fit, which establishes the foundation of developing a general calculating method for calculating the rotor torsional stiffness of equal thickness discs.

2.1. The Regularity of Torsional Stiffness Influence Coefficient of Equal-Thickness Discs

The values of λ with different B (0~0.5), H (0.2, 0.4, 0.6, 0.8) are calculated at a certain diameter D (10 diameters chosen, from 0.1 m ~ 1 m), and their relationship is established. **Figure 2** shows the stiffness influence co-efficient curves of different diameters (D = 0.1 m and D = 1 m).

From **Figure 2**, it can be seen that the two curves for the left one and for the right one are accordant in spite of the fact that one diameter is ten times of the other (in fact the values agree with these curves when the diameter changes from 0.2 m to 0.8 m). It indicates that the value of λ is not related to the D, but is related to the B and H. The longer the B or the H is, the smaller the λ is. But when the H is over the 0.8, the λ is no longer related to the H. In addition, the influence of B on the λ is usually bigger than that of H.

2.2. The Binary Curved Face of Torsional Stiffness Influence Coefficient of Equal-Thickness Discs

In order to get a general equation to calculate the λ directly, the torsional stiffness influence coefficient λ of the equal thickness disc is fit to a binary curved face (shown in the **Figure 3**) and a calculation equation is obtained (their correlation rate is 99.9%).

$$\lambda = \frac{P_1 + P_3 B + P_5 H + P_7 B^2 + P_9 H^2 + P_{11} BH}{1 + P_2 B + P_4 H + P_6 B^2 + P_8 H^2 + P_{10} BH} \tag{2}$$

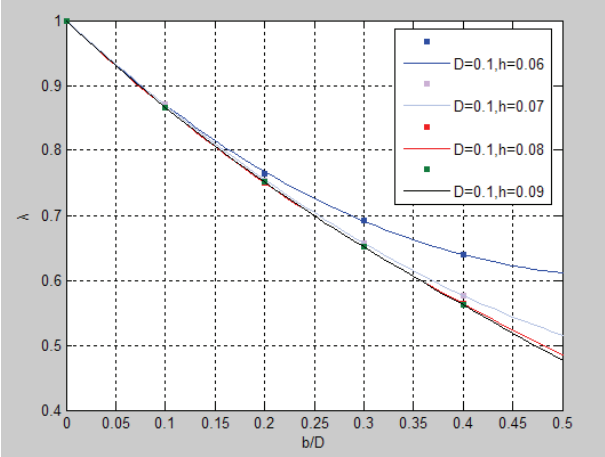

D = 0.1 m

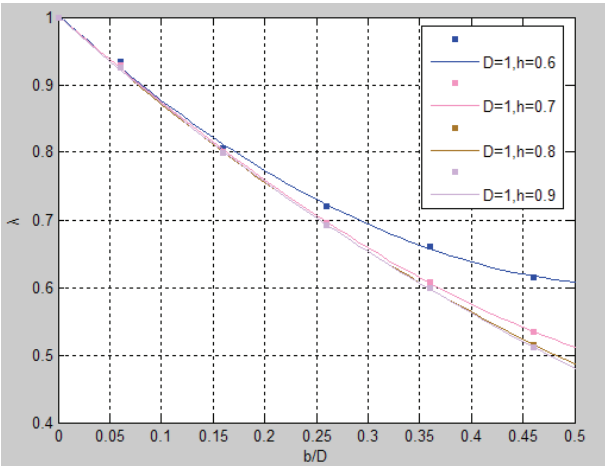

D = 1 m

Figure 2. Stiffness influence coefficient curves of different diameters.

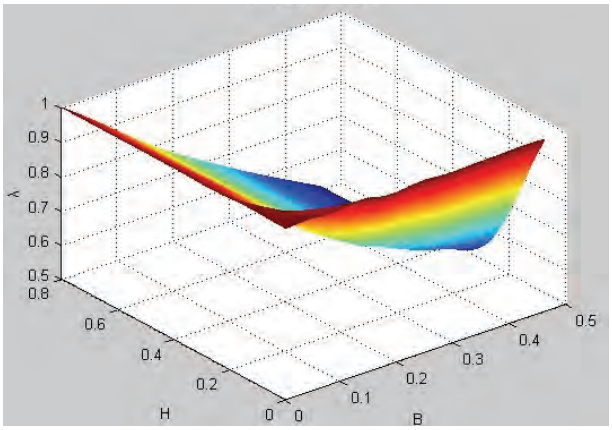

Figure 3. The binary curved face of torsional stiffness influence coefficient of equal-thickness discs.

where, $P_1 = 0.999903$, $P_2 = 0.351506$, $P_3 = 0.352325$, $P_4 = 30.34354$, $P_5 = 30.51446$, $P_6 = 14.73716$, $P_7 = 14.73629$, $P_8 = 7.060696$, $P_9 = 6.831384$, $P_{10} = 7.799944$, $P_{11} = -39.9495$

Then the equivalent stiffness diameter *D''* of the disc can be calculated by:

$$D'' = \frac{D}{\sqrt[4]{1-(1-\lambda)b/L}} \tag{3}$$

So as to verify the precision of (3), groups of data in the numeric area of the different rotors are randomly chosen to calculate their *D''*, which are compared to the exact value of *D'* got by using ANSYS. And the error produced by these two methods is shown in the **Table 1** (only five groups are listed here). From **Table 1**, it can be seen that the errors of the five groups are all less than 1% for any random disc geometric parameters. That is to say that the method proposed in this paper by using (3) can be used as a general calculating method for calculating the equivalent stiffness diameter D'' for different dimensional rotors with equal-thickness discs automatically and with high accuracy.

3. Calculation of the Equivalent Stiffness Diameter of Discs with Complex Structure

The types of the disc on large integral-disc rotors of the steam turbine differ from each other when the capability or the working principle of the units is diverse. The types of discs on most of steam turbine rotors calculated in this paper can be summed up as three kinds: the equal-thickness disc, the stepped equal thickness disc and the cone disc, shown in **Figures 1**, **4** and **5** respectively. Actually, almost all of the discs of steam turbine rotor can be simplified to this three. Obviously there must be some errors if the latter two are simplified as the equal-thickness discs to calculate the equivalent stiffness. So, the emphasis of the following paragraphs is placed on solving of the equivalent stiffness diameter of these two kinds of disc.

3.1. Stepped Equal-Thickness Disc

For the stepped equal-thickness disc, the equivalent stiffness diameter is calculated at first, by treating this kind disc as equal-thickness disc. Then the calculating results are compared with the accurate value (by ANSYS) to determine whether the error caused by such a simplification is permitted. **Table 2** shows the correlation between equal-thickness disc and stepped equal-thickness disc.

3.2. Cone-Shaped Disc

The cone-shaped disc (shown in **Figure 5**) can be treated

Table 1. Equivalent diameters of stiffness calculated by two ways and their error for equal-thickness discs.

SN	b/m	h/m	D/m	L/m	λ	D''/m	D'/m	Error/%
1	0.1191	0.8128	0.99	0.27	0.848546	1.007262	1.007325	0.00623
2	0.102	0.63285	0.1142	0.125	0.902886	1.165816	1.172588	0.57751
3	0.16	0.49315	0.92	0.22	0.846581	0.947617	0.94832	0.07409
4	0.123	0.4445	0.711	0.216	0.793544	0.733582	0.732856	0.099185
5	0.129	0.475	0.7305	0.18	0.785901	0.761562	0.761602	0.00516

Table 2. Correlation between equal-thickness disc and stepped equal-thickness disc.

	D/m	b/m	L/m	b_1/m	D'/m	Error/%
equal-thickness	0.99	0.23	0.27	0	1.0639	-
stepped	0.99	0.23	0.27	0.11	1.0650	0.10
	0.99	0.23	0.27	0.17	1.0648	0.08

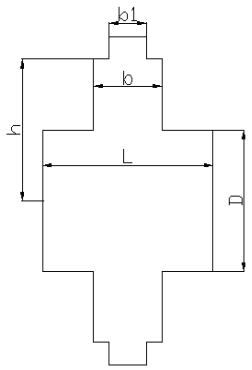

Figure 4. Longitudinal section of stepped equal-thickness disc.

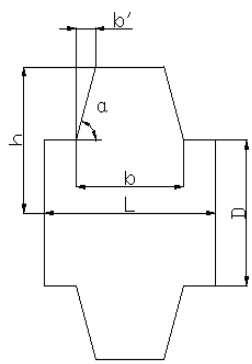

Figure 5. Longitudinal section of cone-shaped disc.

as a equal-thickness disc, from which two parts with right-angled triangles of 90-α degree angle are cut off. And the equivalent stiffness diameter of cone disc is related to the angle of inclination α according to the results of a large number of the calculations. Therefore, cone shaped disc is regarded as equal-thickness disc to get the equivalent stiffness diameter at first. Then the equivalent stiffness diameter is amended two times, by the angle of α and by the error with accurate solution respectively.

Table 3 shows the calculation errors of the equivalent stiffness diameters (the variation range of the angle α is limited from 60° to 90°).

From **Table 3** it can be seen that, when the structure sizes are limited to the areas mentioned above, the calculation errors of the equivalent diameters were less than 5%. Although the errors are within the engineering permissible value, it is amended by an error fitting curve (shown in **Figure 6**), which is obtained by accurate solutions (by ANSYS) to get high accuracy.

Similarly, other discs as cone disc with bulge (shown in **Figure 7**) and stepped equal-thickness cone disc (shown in **Figure 8**) can be treated as equal-thickness disc, while the bulge part can be treated as additional rotary inertia.

The error fitting curve (shown in **Figure 6**) can be fitted as following equation:

$$f(\alpha) = -0.0002117 \cdot \alpha^3 + 0.05342 \cdot \alpha^2 - 4.551 \cdot \alpha + 131.2 \quad (4)$$

With (4), the equivalent stiffness diameters of all kinds of cone discs can be calculated.

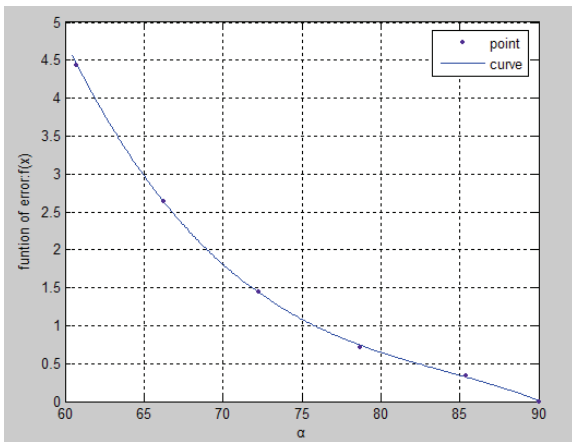

Figure 6. Error fitting curve.

Table 3. The calculation errors of the equivalent stiffness diameters between cone-shape disc and equal-thickness disc.

SN	b'/m	α/°	D'/m	Error/%
1	0	90	0.837561	0
2	0.02	85.43	0.834684	0.3447
3	0.05	78.69	0.831594	0.7175
4	0.08	72.26	0.825677	1.4393
5	0.11	66.256	0.816003	2.6419
6	0.14	60.756	0.801958	4.4395

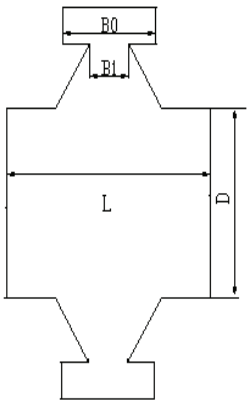

Figure 7. Cone disc with bulge.

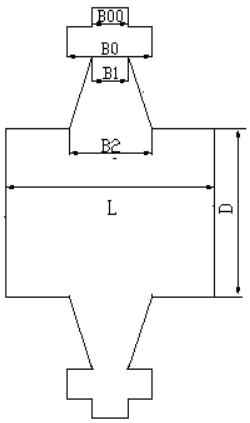

Figure 8. Stepped equal-thickness cone disc.

Table 4 shows the equivalent stiffness diameters obtained by our simplified method and by the precise value, where *D'''* is value by the method used in this paper and *D'* calculated by ANSYS. It can be seen that the errors of the two ways are all less than 0.5%. That proves this simplification method has a higher degree of accuracy.

4. General Calculating Program and Verification Calculation Example

A general calculating program for calculating rotor's torsional vibration features is developed to calculate the characteristics of rotor's torsional vibration with a given data format for different kinds of rotor based on the method mentioned above. To testify the correctness of the method proposed in this paper, the characteristics of the torsional vibration of different kinds of rotors are calculated in this paper, and the result of a 600 MW air-cooled steam turbine rotor is listed here.

4.1. Modeling Method of Integral Rotor

The rotor of a 600 MW air-cooled steam turbine rotor is divided into 173 segments along the axis, shown in **Figure 9** [5].

4.2. Establishing the Disc's Finite Element Model

The disc's finite element model is established by following steps:

1) Establishing a cross section in ANSYS.

2) Generating the corresponding model by rotating the section along the axis [6].

3) Meshing the model by defining the element type as Solid 45. Mapping grid is used so as to get a better quality because it is of better orthogonality.

Figure 10 shows the disc's finite element model.

4.3. Loading Model of the Disc (Torque and Constraint)

For the sake of getting the torsional stiffness of the disc

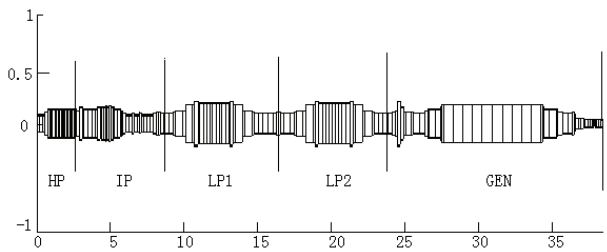

Figure 9. Rotor geometrical model.

Table 4. The equivalent stiffness diameters and errors by simplified method and by precise value.

SN	L/m	b/m	D/m	h/m	α/°	f(α)	D'''/m	D'/m	Error/%
1	0.216	0.123	0.3555	0.598	86.81363	0.205573	0.366427	0.366428	0.00031
2	0.18	0.129	0.36525	0.598	86.43516	0.228928	0.380206	0.380801	0.15621
3	0.498	0.4565	0.39	0.64	67.95205	2.191521	0.458577	0.456555	0.442767
4	0.22	0.17527	0.4725	0.70	82.96241	0.432271	0.494731	0.49715	0.48673

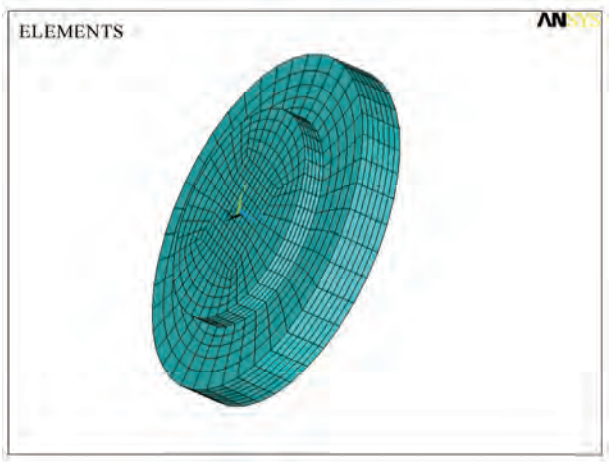

Figure 10. Disc modeling and meshing.

under twisted state, the model established above is loaded in ANSYS by exerting a torque at one end of the disc and fix the other end. The specific steps in loading the torque are described as follows:

1) Establishing a node in the center of the surface, defined as mass 21 unit.

2) Coupling the node with the other nodes to form a rigid region (using 'cerig' command).

3) Loading the torque directly to the master node-the central node.

4.4. Calculating Disc's Equivalent Stiffness Diameter

With the model above-mentioned, twist angle cloud of the disc model under a certain torque T can be obtained (shown in **Figure 11**), when the related material properties are defined in ANSYS. The largest twist angle φ of the disc can be found out in **Figure 11**. Then the torsional stiffness k and the equivalent stiffness diameter D' can be calculated by using (5) and (6).

$$k = T / \varphi \tag{5}$$

$$D' = \sqrt[4]{(2kL)/(\pi G)} \tag{6}$$

where L is the length of the disc and G is the shear modulus.

4.5. Calculating Results

Table 5 and **Figure 12** show the values of the first four orders of torsional vibration frequencies and modes of this rotor obtained from the designed value, the measured value, and the calculated value of this paper (Holzer transfer matrix and Riccati transfer matrix are used). It can be seen that the results of method proposed in this paper are consistent with the measured values and can meet the requirement of accuracy.

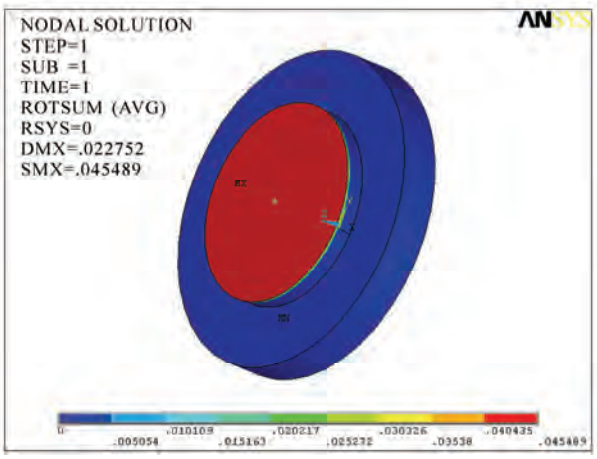

Figure 11. Twist angle cloud of the disc.

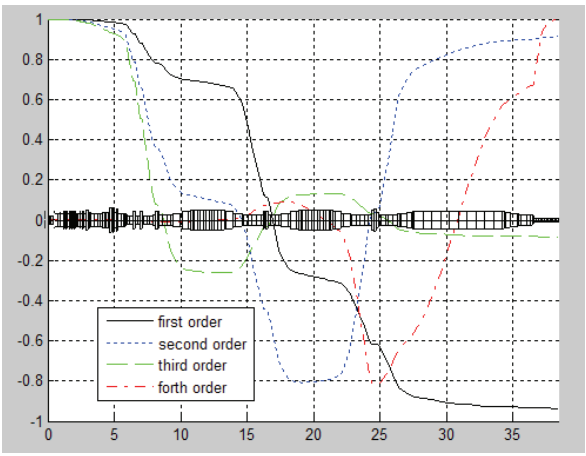

Figure 12. The first four orders of the rotor's torsional vibration modes.

Table 5. The first four orders of the rotor's torsional vibration frequencies* /Hz.

Order		1	2	3	4
designed value		15.03	25.95	30.04	120.3
Measured value		15.3	26.1	30.55	-
Calculated	Holzer	15.2	26.2	31.8	121.6
value	Riccati	15.3	26.3	31.8	124.5

5. Conclusions

To develop a general method to calculate the characteristics of rotor's torsional vibration by using data under given format for different kinds of rotor automatically, the stiffness influence coefficient of single equal thickness disc is resolved at first. Then the torsional stiffness influence coefficient λ of equal thickness disc is fit to a binary curved face and a calculation equation is obtained based on this curved face. In addition, a simplified calculation method for calculating equivalent stiffness diameter of discs with complex structure, such as stepped equal thickness disc and cone disc, is proposed. Following conclusions can be drawn from this paper:

1) The stiffness influence coefficient λ of equal-thickness disc depends on relative thickness B and the relative height H, but not with b and h. And the influence of B on λ is greater than H.

2) Discs with complex structure can be simplified to equal-thickness disc with little error by using the method suggested in this paper, and the error can be control within 1%.

3) The general calculating program developed in this paper is verified to have a universal property and with a reasonable accuracy.

6. Acknowledgements

This work is supported by Dongfang Turbine Co., Ltd. in China.

7. References

[1] W. F. Li, D. M. Xie, *et al.*, "Calculation of Rotor's Torsional Vibration Characteristics Based on Equivalent Diameter of Stiffness," *Asia-Pacific Power and Energy Engineering Conference* (*APPEEC* 2010), Chengdu, 2010.

[2] W. X. Shi, "Turbine Vibration," Water Conservancy and Electric Power Press, Beijing, 1991.

[3] H. T. Sun, "Approach to Torsional Vibration of Shaft System for High-Capacity Turbo-Generations," *Thermal Power Generation*, Vol. 33, No. 1, 2004, pp. 42-44.

[4] D. N. Walker, S. L. Adams and R. J. Placek, "Torsional Vibration and Fatigue of Turbine Generator Shafts," *IEEE Transactions on Power Apparatus and Systems*, Vol. 100, No. 11, 1981, pp. 4373-4380.

[5] Y. L. Li, "Study on Torsional Vibration Characteristics of Turbine Rotor with Cracks Based on ANSYS," Wuhan University, Wuhan, 2008.

[6] L. L. Dang, Z. Y. Weng and G. L. Xu, "Research in Equivalent Rigidity of Rotor Vibration," *Mechanical Engineer*, No. 4, 2009, pp. 89-91.

[7] D. M. Xie, C. Dong and Z. H. Liu, "The Torsional Rigidity of a Shafting Specific Structure and its Effect on the Torsional Vibration Characteristics," *Thermal Power Engineering*, Vol. 22, No. 2, 2007, pp. 146-148.

[8] H. Y. Wu, "Structure and Strength Calculation of Turbine Parts," Machinery Industry Press, Beijing, 1982.

Engineering, 2010, 2, 705-709
doi:10.4236/eng.2010.29091 Published Online September 2010 (http://www.SciRP.org/journal/eng)

Some Aspects of Non-Orthogonal Stagnation-Point Flow towards a Stretching Surface

Motahar Reza[1], Anadi Sankar Gupta[2]
[1]*Department of Mathematics, National Institute of Science & Technology, Berhampur, India*
[2]*Department of Mathematics, Indian Institute of Technology, Kharagpur, India*
E-mail: *reza@nist.edu*
Received May 12, 2010; *revised July* 21, 2010; *accepted August* 3, 2010

Abstract

The problem of steady two-dimensional oblique stagnation-point flow of an incompressible viscous fluid towards a stretching surface is reexamined. Here the surface is stretched with a velocity proportional to the distance from a fixed point. Previous studies on this problem are reviewed and the errors in the boundary conditions at infinity are rectified. It is found that for a very small value of shear in the free stream, the flow has a boundary layer structure when $a/c>1$, where ax and cx are the free stream stagnation-point velocity and the stretching velocity of the sheet, respectively, x being the distance along the surface from the stagnation-point. On the other hand, the flow has an inverted boundary layer structure when $a/c<1$. It is also observed that for given values of a/c and free stream shear, the horizontal velocity at a point decreases with increase in the pressure gradient parameter.

Keywords: Oblique Stagnation-Point Flow, Stretching Surface

1. Introduction

The study of the flow of an incompressible viscous fluid over a stretching surface has important bearing on several technological and industrial processes. Problems such as the extrusion of polymers in melt-spinning, glass blowing, spinning of fibers a several metallurgical as well as metal-working processes involve certain aspects of flow over stretching sheets. Crane [1] obtained a similarity solution in closed analytical form for steady two-dimensional flow of an incompressible viscous fluid caused solely by the stretching of an elastic sheet which moves in its own plane with a velocity varying linearly with distance from a fixed point.

Chiam [2] investigated steady two-dimensional orthogonal and oblique stagnation-point flow of an incompressible viscous fluid towards a stretching surface in the case when the parameter b representing the ratio of the strain rate of the stagnation-point flow to that of the stretching surface is equal to unity. By removing this highly restrictive assumption ($b=1$), Mahapatra and Gupta [3] analyzed the steady two-dimensional orthogonal stagnation-point flow of an incompressible viscous fluid to-wards a stretching surface in the general case $b\neq 1$. They observed that the structure of the boundary layer depends crucially on the value of b. Reza and Gupta [4] generalized the problem of an oblique stagnation-point flow over a stretching surface by Chiam [2] to include surface strain rate different from that of the stagnation flow. But since the displacement thickness arising out of the boundary layer on the surface was ignored in their boundary condition at infinity, the analysis in [4] is of doubt full validity. This was rectified in a paper by Lok, Amin and Pop [5]. However, these authors [5] did not take into account the pressure gradient parameter in the boundary condition at infinity. This is a serious omission since the pressure gradient parameter is linked to the free stream shear in the oblique stagnation-point flow (Drazin and Riley [6]). Hence the results of the paper in [5] are also of doubtful validity.

It is noted that planar oblique stagnation-point flow of an incompressible viscous flow of an incompressible viscous fluid towards affixed rigid surface was first studied by Stuart [7]. This problem was later independently investigated by Tamada [8] and Dorrepaal [9]. The analogue of the planar oblique stagnation-point flow to stagnation flow obliquely impinging on a rigid circular cylinder was discussed by Weidman and Putkaradze [10]. Exact similarity solutions for impingement of two viscous immiscible oblique stagnation flows forming a flat

interface was given by Tilley and Weidman [11]. On the other hand heat transfer in oblique stagnation-point flow of an incompressible viscous fluid towards stretching surface was investigated by Mahapatra, Dholey and Gupta [12]. Further oblique stagnation-point flow of a viscoelastic fluid towards a stretching surface was studied by Mahapatra, Dholey and Gupta [13].

The objective of the present paper is to rectify the errors in [4] and [5] and give a correct solution to the above problem. It is worth pointing out that an oblique stagnation-point flow occurs when a separated viscous flow reattaches to a surface.

2. Flow Analysis

Consider the steady two-dimensional flow near a stagnation point when an incompressible viscous fluid impinges obliquely on an elastic surface coinciding with the plane $y=0$, the flow being confined to $y>0$. Two equal and opposite forces are applied along the *x*-axis so that the surface is stretched keeping the origin fixed, as shown in **Figure 1**. The velocity components in the inviscid free stream along the *x* and *y* directions are

$$U_0 = ax + 2b(y-\delta_1),\ \ V_0 = -a(y-\delta_2), \tag{1}$$

respectively, where a and b are constants. Further δ_2 is the displacement thickness arising out of the boundary layer on the stretching surface and δ_1 is the parameter which controls the horizontal pressure gradient that produces the shear flow. Note that the whole flow field given by (1) may be viewed as being composed of an orthogonal stagnation-point flow combined with a horizontal shear flow. The corresponding stream function for the above velocity distribution is

$$\psi_0 = ax(y-\delta_2) + b(y-\delta_1)^2 \tag{2}$$

There appears a boundary layer on the surface at high Reynolds number. At the stretching surface, the no-slip condition gives

$$u = cx\ , v = 0 \quad \text{at} \quad y = 0, \tag{3}$$

where c is a positive constant and u and v are the velocity components along x and y directions, respectively. In Reza & Gupta [4], stream function in the boundary layer was assumed in the form

$$\frac{\psi}{\nu} = \xi F(\eta) + W(\eta), \tag{4}$$

where ν is the kinematic viscosity and

$$\xi = x\left(\frac{c}{\nu}\right)^{\frac{1}{2}},\ \ \eta = y\left(\frac{c}{\nu}\right)^{\frac{1}{2}}, \tag{5}$$

This gives the dimensionless velocity components from (4) and (5) as

$$U = \xi F'(\eta) + W'(\eta)\ , V = -F(\eta), \tag{6}$$

where $U = u/(c\nu)^{1/2}$ and $V = v/(c\nu)^{1/2}$. Using (6) in the Navier-Stokes equations it was shown in [4] that $F(\eta)$ and $W(\eta)$ satisfy the following equations

$$F'^2 - FF'' - F''' = c_1, \tag{7}$$

$$F'W' - FW'' - W''' = c_2, \tag{8}$$

where c_1 and c_2 are constants. From (6), no-slip conditions (3) become

$$F(0) = 0, F'(0) = 1, \tag{9}$$

$$W(0) = 0, W'(0) = 0. \tag{10}$$

Further from (1) and (6), the boundary condition for $F(\eta)$ and $W(\eta)$ at infinity are

$$F'(\eta) \sim \frac{a}{c}\ \ ;\ \ F(\eta) \sim \frac{a}{c}(\eta - d_2) \quad \text{as} \quad \eta \to \infty, \tag{11}$$

$$W'(\eta) \sim 2\frac{b}{c}(\eta - d_1) \quad \text{as} \quad \eta \to \infty, \tag{12}$$

where $d_2\left(=(c/\nu)^{\frac{1}{2}}\delta_2\right)$ is the dimensionless displacement thickness parameter and $d_1\left(=(c/\nu)^{\frac{1}{2}}\delta_1\right)$ is the dimensionless pressure gradient parameter linked to the free stream shear flow.

Reza and Gupta [4] ignored both the constants δ_1 and δ_2 in (1). While pointing out that δ_2 should be taken into account (as mentioned in the Introduction), Lok, Amin & Pop [5] rectified this error in [4]. However, these authors in [5] lost sight of the constant δ_1 in (1) and consequently arrived at governing equations for the velocity distribution one of which is incorrect. Hence their analysis is of doubtful validity.

Using the boundary conditions (11) and (12) in (7) and (8), we get

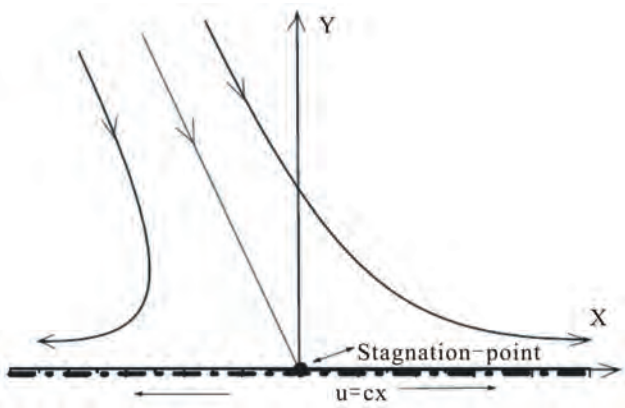

Figure 1. A sketch of the physical problem.

$$c_1 = \frac{a^2}{c^2},\ c_2 = 2\frac{ab}{c^2}(d_2 - d_1)\ . \tag{13}$$

Thus the governing equations for $F(\eta)$ and $W(\eta)$ become

$$F'^2 - FF'' - F''' = \frac{a^2}{c^2}, \tag{14}$$

$$F'W' - FW'' - W''' = 2\frac{ab}{c^2}(d_2 - d_1). \tag{15}$$

Note that Equation (15) derived by Lok *et al.* [5] does not include d_1. Further the boundary condition (12) in [5] is also erroneous due to the absence of d_1. Substitution of (14) and (15) in the x and y momentum equations followed by integration gives the pressure distribution $p(x, y)$ in the flow as

$$\frac{p(x,y)}{c\rho\nu} = -\frac{1}{2}\left(\frac{a^2}{c^2}\xi^2 + F^2\right) - F' - 2\frac{ab}{c^2}(d_2 - d_1)\xi + \text{constant}. \tag{16}$$

which can be found once $F(\eta)$ is known.

Equations (14) and (15) subject to the boundary conditions (9)-(12) are solved numerically by finite difference method using Thomas algorithm (Fletcher [14]).

3. Results and Discussion

Figure 2 shows the variation of $U(\xi,\eta)$ with η at a fixed value of ξ(= 0.5) for several values of a/c when the pressure gradient parameter $d_1 = 0.5$ and $b/c = 1.0$. It can be seen that at a given value of η, U increases with increase in a/c. Further when *b/c* is very small and equal to 0.05, say, the velocity profile at a fixed value of $\xi(= 0.5)$ for several values of a/c with $d_1 = 0.5$ shows a boundary layer structure (see **Figure 3**) and the thickness of the boundary layer decreases with increase in a/c. From a physical point of view, this stems from the fact that increase of straining motion in the free stream (e.g., increase in a/c for a fixed value of c) leads to increase in acceleration of the free stream. This results in thinning of boundary layer.

Figure 3 shows that when the free stream shear is negligible ($b/c = 0.05$ for a given value of *c*), the flow has a boundary layer structure because in this case straining motion dominates over the shear. However, this boundary layer structure is affected to a great extent in the presence of considerable shear in the free stream (see **Figure 2**).

The dimensionless displacement thickness d_2 is computed for different values of a/c from the solution of Equation (14) subject to the boundary conditions (9) and (11) and shown in the above **Table 1**. It may be noticed that for $a/c = 1$, displacement thickness is approximately zero (numerically). This is due to fact that when $a/c = 1$, the stretching velocity of the plate is precisely equal to the irrotational straining velocity. From a physical point of view, the absence of boundary layer in this case arises from the fact that although the flow is not frictionless in a strict sense, the friction is uniformly distributed and does not therefore affect the motion. Stuart [7] and Tamada [8] showed that the value of the dimensional displacement thickness is 0.6479 for oblique stagnation point flow over a rigid plate. This result can be compared with that of our problem by considering $c = 0$ in the boundary condition (3) which gives $F(0) = 0$ and $F'(0) = 0$. We have found that the value of the displacement thickness is $d_2 = 0.64788$. It may be noted that in both the studies of Stuart [7] and Tamada [8], the pressure gradient parameter $\delta_1 \neq 0$.

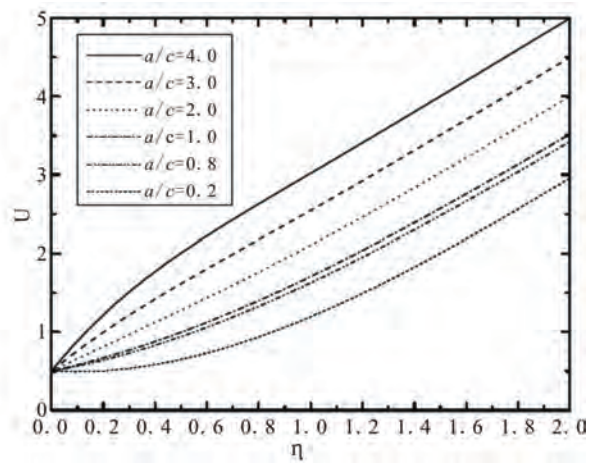

Figure 2. Variation of $U(\xi,\eta)$ with η at $\xi = 0.5$ for several values of a/c when $d_1 = 0.5$ and b/c = 1.0.

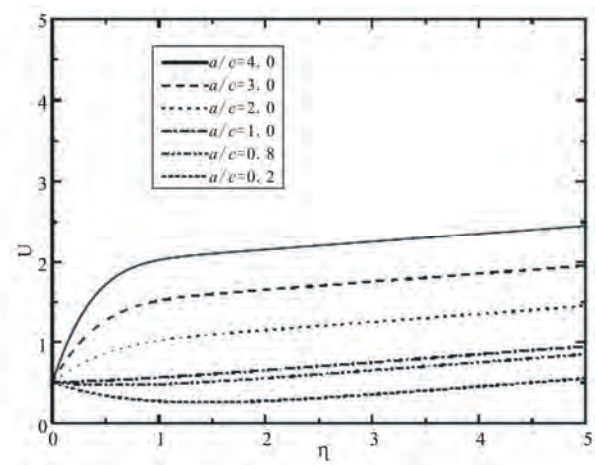

Figure 3. Variation of $U(\xi,\eta)$ with η at $\xi = 0.5$ for several values of a/c when $d_1 = 0.5$ and b/c = 0.05.

Table 1. Values of the displacement thickness d_2 for several values of a/c.

a/c	3	2	1.5	1.0
d_2	0.235278	0.2082290	0.1548889	9.3602152×10^{-7}

Figure 4 displays the variation of $U(\xi, \eta)$ with η at a fixed location ξ(= 0.5) for several values of the pressure gradient parameter d_1 when $a/c=3$ and $b/c=1.0$. It may be seen that at a given value of η, the horizontal velocity *U* decreases with increase in d_1.

The streamline patterns for the oblique stagnation-point flow are shown in **Figures 5(a)** and **5(b)** for very small value of the free stream shear b/c = 0.05 and d_1 = 0.4 in two cases 1) a/c = 0.2, 2) a/c = 5.0. It can be seen that for $a/c<1$, the stream lines are slightly tilted towards the left. but when a/c is large (= 5), the flow almost resembles that of an orthogonal stagnation-point flow as long as the free stream shear is very small (see **Figure 5(b)**). For moderate value of free stream shear ($b/c=1$), the disposition of the streamlines is shown in **Figures 6(a)** and **6(b)** for a/c = 0.2, and a/c = 2.0, respectively. It is observed from **Figures 5(a)** and **6(a)** that for a given value of a/c (= 0.2), with increase in the free stream shear, the streamlines become more tilted towards the left. We also find that with increase in the straining motion in the free stream, the streamlines are less and less tilted to the left. This is plausible on physical grounds because with increase in a/c for a given value of b/c, the flow tends to resemble an orthogonal stagnation-point flow.

4. Summary

An exact solution of the Navier-Stokes equations is given which represents steady two-dimensional oblique stagnation-point flow of an incompressible viscous fluid towards a surface stretched with velocity proportional to the distance from a fixed point. It is shown that when the free stream shear is negligible, the flow has a boundary layer behaviour when the stretching velocity is less than the free stream velocity ($a/c>1$), and it has an inverted boundary layer structure when just the reverse is true ($a/c<1$). It is found that the obliquity of the flow towards the surface increases with increase in b/c. This is consistent with the fact that increase in b/c (for a fixed value of a/c) results in increase in the shearing motion which in turn leads to increased obliquity of the flow towards the surface.

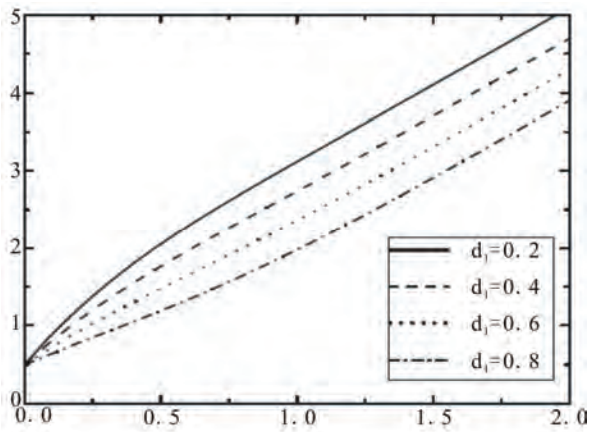

Figure 4. Variation of $U(\xi,\eta)$ with η at $\xi=0.5$ for several values d_1 when $a/c=3.0$ and b/c = 1.0.

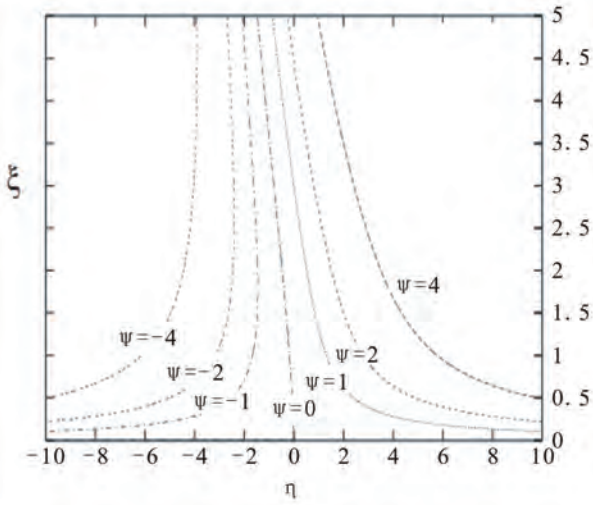

(a) when a/c = 0.2

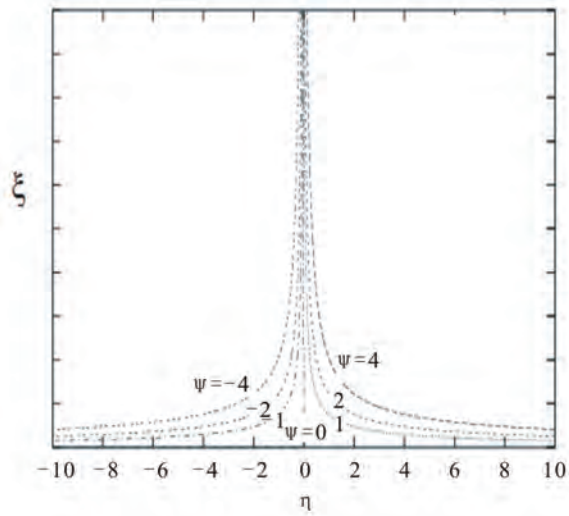

(b) when a/c = 5.0

Figure 5. Streamline patterns for b/c = 0.05 and d_1 = 0.4 (a) when a/c = 0.2 (b) when a/c = 5.0.

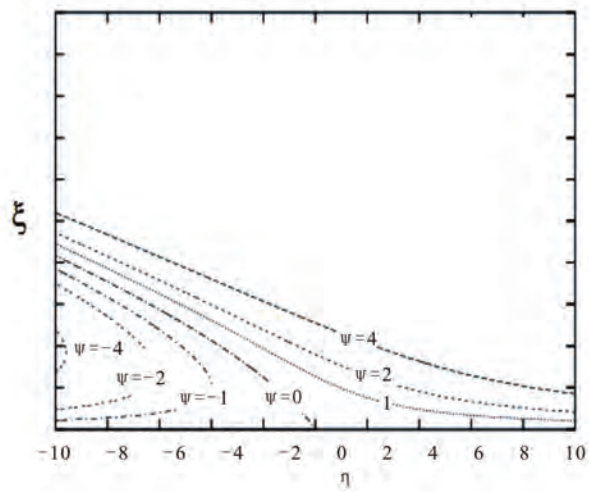

(a) when a/c = 0.2.

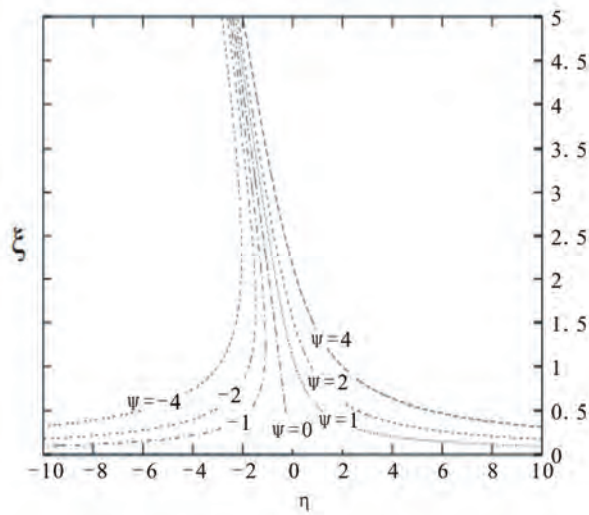

(b) when a/c = 2.0

Figure 6. Streamline patterns for b/c = 1.0 and d_1 = 0.4 (a) when a/c = 0.2; (b) when a/c = 2.0.

5. Acknowledgements

One of the authors (A. S. G) acknowledges the financial assistance of Indian National Science Academy, New Delhi for carrying out this work. Authors would also like to acknowledge the use of the facilities and technical assistance of the Center of Theoretical Studies at Indian Institute of Technology, Kharagpur.

6. References

[1] L. J. Crane, "Flow Past a Stretching Plate," *Zeitschrift für angewandte Mathematik und Physik*, Vol. 21, 1970, pp. 645-657.

[2] T. C. Chiam, "Stagnation-Point Flow towards a Stretching Plate," *Journal of Physical Society of Japan*, Vol. 63, No. 6, 1994, pp. 2443-2444.

[3] T. R. Mahapatra and A. S. Gupta, "Heat Transfer in Stagnation-Point Flow towards a Stretching Sheet," *Heat and Mass Transfer*, Vol. 38, No. 6, 2002, pp. 517-521.

[4] M. Reza and A. S. Gupta, "Steady Two-Dimensional Oblique Stagnation Point Flow towards a Stretching Surface," *Fluid Dynamics Research*, Vol. 37, No. 5, 2005, pp. 334-340.

[5] Y. Y. Lok, N. Amin and I. Pop, "Non-Orthogonal Stagnation Point towards a Stretching Sheet," *International Journal of Non-Linear Mechanics*, Vol. 41, No. 4, 2006, pp. 622-627.

[6] P. G. Drazin and N. Riley, "The Navier-Stokes Equations: A Classification of Flows and Exact Solutions," Cambridge University Press, Cambridge, 2006.

[7] J. T. Stuart, "The Viscous Flow near a Stagnation Point when External Flow has Uniform Vorticity," *Journal of the Aero/Space Sciences*, Vol. 26, 1959, pp. 124-125.

[8] K. Tamada, "Two-Dimensional Stagnation-Point Flow Impinging Obliquely on a Plane Wall," *Journal of Physical Society of Japan*, Vol. 46, No. 1, 1979, pp. 310-311.

[9] J. M. Dorrepaal, "An Exact Solution of the Navier-Stokes Equation which Describes Non-Orthogonal Stagnation-Point Flow in Two Dimensions," *Journal of Fluid Mechanics*, Vol. 163, 1986, pp. 141-147.

[10] D. Weidman and V. Putkaradzeb, "Axisymmetric Stagnation Flow Obliquely Impinging on a Circular Cylinder," *European Journal of Mechanics - B/Fluids*, Vol. 22, No. 2, 2003, pp. 123-131.

[11] B. S. Tilley, P. D. Weidman, "Oblique Two-Fluid Stagnation-Point Flow," *European Journal of Mechanics - B/Fluids*, Vol. 17, No. 2, 1998, pp. 205-217.

[12] T. R. Mahapatra, S. Dholey and A. S. Gupta, "Heat Transfer in Oblique Stagnation-Point Flow of an Incompressible Viscous Fluid towards a Stretching Surface," *Heat and Mass Transfer*, Vol. 43, No. 8, 2007, pp. 767-773.

[13] T. R. Mahapatra, S. Dholey and A. S. Gupta, "Oblique Stagnation-Point flow of an Incompressible Visco-Elastic Fluid towards a Stretching Surface," *International Journal of Non-Linear Mechanics*, Vol. 42, No. 3, 2007, pp. 484-499.

[14] C. A. J. Fletcher, "Computational Techniques for Fluid Dynamics," Vol. 2, Springer-Verlag, Berlin, 1988.

Engineering, 2010, 2, 710-719
doi:10.4236/eng.2010.29092 Published Online September 2010 (http://www.SciRP.org/journal/eng)

Optimization of Biodynamic Seated Human Models Using Genetic Algorithms

Wael Abbas[1*], Ossama B. Abouelatta[2], Magdi El-Azab[3], Mamdouh Elsaidy[4], Adel A. Megahed[5]
[1]*Engineering Physics and Mathematics Department, Faculty of Engineering* (*Mataria*), *Helwan University, Cairo, Egypt*
[2]*Production Engineering and Mechanical Design Department, Faculty of Engineering, Mansoura University, Mansoura, Egypt*
[3,4]*Mathematics and Engineering Physics Department, Faculty of Engineering, Mansoura University, Mansoura, Egypt*
[5]*Mathematics and Engineering Physics Department, Faculty of Engineering, Cairo University, Cairo, Egypt*
E-mail: *wael_abass@hotmail.com*
Received May 16, 2010; *revised July* 21, 2010; *accepted August* 4, 2010

Abstract

Many biodynamic models have been derived using trial and error curve-fitting technique, such that the error between the computed and measured biodynamic response functions is minimum. This study developed a biomechanical model of the human body in a sitting posture without backrest for evaluating the vibration transmissibility and dynamic response to vertical vibration direction. In describing the human body motion, a three biomechanical models are discussed (two models are 4-DOF and one model 7-DOF). Optimization software based on stochastic techniques search methods, Genetic Algorithms (GAs), is employed to determine the human model parameters imposing some limit constraints on the model parameters. In addition, an objective function is formulated comprising the sum of errors between the computed and actual values (experimental data). The studied functions are the driving-point mechanical impedance, apparent mass and seat-to-head transmissibility functions. The optimization process increased the average goodness of fit and the results of studied functions became much closer to the target values (Experimental data). From the optimized model, the resonant frequencies of the driver parts computed on the basis of biodynamic response functions are found to be within close bounds to that expected for the human body.

Keywords: Biodynamic Response, Seated Human models, Simulation, Genetic algorithms

1. Introduction

Recently, many people have focused their attention on the ride quality of vehicle which is directly related to driver fatigue, discomfort, and safety. As traveling increases, the driver is more exposed to vibration mostly originating from the interaction between the road and vehicle. Whole-body vibration occurs in transportation and when near heavy machinery [1]. The vibrations cause the operator's whole body to vibrate, as opposed to just one part of their body, says their hand or foot. Harmful effects of whole-body vibration are experienced when the exposure time is longer than the recommended standard set by ISO 2631-1 [2].

Biodynamic responses of seated human occupant exposed to vibration have been widely characterized to define frequency-weightings for assessment of exposure, to identify human sensitivity and perception of vibration, and to develop seated body models [3]. The biodynamic response of the human body exposed to vibration have been invariably characterized through measurement of force motion relationship at the point of entry of vibration "To-the-body response function", and transmission of vibration to different body segments "Through-the-body response function". Considering that the human body is a complex biological system, the "To-the-body" response function is conveniently characterized through non-invasive measurements at the driving point alone. The vast majority of the reported studies on biodynamic response to whole-body vibration have considered vibration along the vertical axis alone.

The reported studies on biodynamic responses under

vertical vibration are thoroughly reviewed, specifically their response characteristics, experimental conditions, and the measured data. The biodynamic response characteristics reported in terms of either the driving-point mechanical impedance (DPMI) or apparent mass (APMS), and the seat-to-head transmissibility (STHT) are classified under different experimental conditions used in the study.

In early studies, various biodynamic models have been developed to depict human motion from single-DOF to multi-DOF models. These models can be divided as distributed (finite element) models, lumped parameter models and multi-body models. The distributed model treats the spine as a layered structure of rigid elements, representing the vertebral bodies, and deformable elements representing the intervertebral discs by the finite element method. Multi-body human models are made of several rigid bodies interconnected by pin (two-dimensional) or ball and socket (three-dimensional) joints, and can be further separated into kinetic and kinematic models.

The lumped parameter models consider the human body as several rigid bodies and spring-dampers. This type of model is simple to analyze and easy to validate with experiments. However, the disadvantage is the limitation to one-directional analysis. Coermann [4], measured the driving-point impedance of the human body and suggested 1-DOF model. Suggs *et al.* [5] developed a 2-DOF human body. It was modeled as a damped spring-mass system to build a standardized vehicle seat testing procedure. A 3-DOF analytical model for a tractor seat suspension system is presented by Tewari *et al.* [6]. It was observed that the model could be employed as a tool in selection of optimal suspension parameters for any other type of vehicles. Boileau *et al.* [7] used an optimization procedure to establish a 4-DOF human model based on test data. In addition, Zong and Lam [8] validated a 4-DOF nonlinear model originating from Liu *et al.* [9].

Furthermore, Muksian and Nash [10] presented a 6-DOF nonlinear model dedicated to the analysis of vibration imposed on a seated human. This model was modified by Patil *et al.* [11], who suggested a 7-DOF model. This model was further incorporated with a tractor model to evaluate vibration responses of an occupant-tractor system. A complete study on lumped-parameter models for seated human under vertical vibration excitation has been carried out by Liang and Chiang [12], based on analytical study and experimental validation.

On the other hand, GA optimization is used by Baumal *et al.* [13] to determine both active control and passive mechanical parameters of a vehicle suspension system, to minimize the extreme acceleration of the passenger's seat, subjected to constraints representing the required road holding ability and suspension working space. The GA is used to solve the problem and results were compared to those obtained by simulated annealing technique and found to yields similar performance measures.

It is clear that the lumped-parameter model is probably one of the most popular analytical methods in the study of biodynamic responses of seated human subjects, though it is limited to one-directional analysis. However, vertical vibration exposure of the driver is our main concern. Therefore, this paper carries out a thorough survey of literature on the lumped-parameter models for seated human subjects exposed to vertical vibration.

This work aims to develop a biomechanical model of the human body in a sitting posture without backrest for evaluating the vibration transmissibility and dynamic response to vertical vibration direction.

2. Biodynamic Response of the Human Body

The biodynamic response of a seated human body exposed to whole-body vibration can be broadly categorized into two types. The first category "To-the-body" force motion interrelation as a function of frequency at the human-seat interface, expressed as the driving-point mechanical impedance or the apparent mass. The second category "Through-the-body" response function, generally termed as seat-to-head transmissibility for the seated occupant.

The DPMI relates the driving force and resulting velocity response at the driving point (the seat-buttocks interface), and is given by [3]:

$$Z(j\omega) = \frac{F(j\omega)}{V(j\omega)} = \frac{F(j\omega)}{X^{\bullet}(j\omega)} \tag{1}$$

where, $Z(j\omega)$ is the complex DPMI, $F(j\omega)$ and $V(j\omega)$ or $X^{\bullet}(j\omega)$ are the driving force and response velocity at the driving point, respectively. ω is the angular frequency in rad/s , and $j = \sqrt{-1}$ is the complex phasor.

In a similar manner, the apparent mass response relates the driving force to the resulting acceleration response, and is given by [14]:

$$APMS(j\omega) = \frac{F(j\omega)}{a(j\omega)} \tag{2}$$

where, $a(j\omega)$ is the acceleration response at the driving point. The magnitude of *APMS* offers a simple physical interpretation as it is equal to the static mass of the human body supported by the seat at very low frequencies, when the human body resembles that of a rigid

mass. The above two functions are frequently used interchangeably, due to their direct relationship that given by:

$$APMS(j\omega) = \frac{DPMI(j\omega)}{j\omega} \quad (3)$$

The biodynamic response characteristics of seated occupants exposed to whole body vibration can also be expressed in terms of seat-to-head transmissibility, which is termed as "through-the-body" response function. Unlike the force-motion relationship at the driving-point, the STHT function describes the transmission of vibration through the seated body. The STHT response function is expressed as:

$$H(j\omega) = \frac{a_H(j\omega)}{a(j\omega)} \quad (4)$$

where, $H(j\omega)$ is the complex STHT, $a_H(j\omega)$ is the response acceleration measured at the head of seated occupant, and $a(j\omega)$ is the acceleration response at the driving point. The above three functions have been widely used to characterize the biodynamic responses of the seated human subjects exposed to whole body vibration.

3. Experimental Data

Many mathematical models on the study of biodynamic responses of seated human subjects have been published based on individual test data over the years. However, significant variation is known to exist between various data sets. Such variation may be partly attributed to the differences associated with the methodology, experimental conditions or subject population used by different investigators.

3.1. Basic Assumptions on Experimental Data

The biodynamic of seated human subjects exposed to vertical vibration has been widely assessed in terms of STHT, DPMI, and APMS. The first function refers to the transmission of motion through the body, while the other two relate the force and motion at the point of vibration input to the body. A variety of test data used to characterize these response functions has been established using widely varied test conditions. This has resulted in considerable discrepancies among the data. To avoid these discrepancies, a preliminary conclusion was reached that any attempt to define generalized values might not be appropriate unless it could be defined specifically for a particular application or within a limited and well-defined range of situations [12].

Data sets satisfying the following requirements are selected for the synthesis of biodynamic characteristics of the seated human subjects [15-17].

- A human subject is considered to be sitting erect without backrest support, irrespective of the hands' position.
- Body masses will be limited within 49-94 kg.
- Feet are supported and vibrated.
- Analysis is constrained to the vertical direction.
- Vibration excitation amplitudes are below 5 m/s^2, with the nature of excitation specified as being sinusoidal wave.
- Excitation frequency range is limited to 0.5-20 Hz.

3.2. Experimental Results

While vertical DPMI, APAS, and STHT characteristics were not measured as part of this study, applicable target values were defined on the basis of a synthesis of published data Boileau [14], Liang *et al.* [12,17] and Wu [18]. **Figure 1** shows upper, lower, and target values of DPMI, APMS, and STHT magnitude established as target values within 0.5-20 Hz frequency range, respectively.

4. Biomechanical Modeling

The human body in a sitting posture can be modeled as a mechanical system that is composed of several rigid bodies interconnected by springs and dampers. In this study, three types of biomechanical models are discussed to describe the vertical response: 4-DOF Wan and Schimmels model, 4-DOF Boileau and Rakheja model, and 7-DOF Patil and Palanichamy model as shown in **Figure 2**.

4.1. Wan and Schimmels 4-DOF Model

In this model, the seated human body was constructed with four separate mass segments interconnected by five sets of springs and dampers, with a total human mass of 60.67 kg [19]. The four masses represent the following body segments: head and neck (m_1), upper torso (m_2), lower torso (m_3), and thighs and pelvis (m_4). The arms and legs are combined with the upper torso and thigh, respectively. The stiffness and damping properties of thighs and pelvis are (k_5) and (c_5), the lower torso are (k_4) and (c_4), upper torso are (k_2, k_3) and (c_2, c_3), and head are (k_1) and (c_1). The schematic of the model is shown in **Figure 2(a)**, and biomechanical parameters of the model are listed in **Table 1**.

The equations of motion of the human-body can be obtained as follows:

$$
\begin{cases}
m_1 \ddot{x}_1 = -c_1(\dot{x}_1 - \dot{x}_2) - k_1(x_1 - x_2) \\
m_2 \ddot{x}_2 = c_1(\dot{x}_1 - \dot{x}_2) + k_1(x_1 - x_2) - c_2(\dot{x}_2 - \dot{x}_3) \\
-k_2(x_2 - x_3) - c_3(\dot{x}_2 - \dot{x}_4) - k_3(x_2 - x_4) \\
m_3 \ddot{x}_3 = c_2(\dot{x}_2 - \dot{x}_3) + k_2(x_2 - x_3) \\
-c_4(\dot{x}_3 - \dot{x}_4) - k_4(x_3 - x_4) \\
m_4 \ddot{x}_4 = c_4(\dot{x}_3 - \dot{x}_4) + k_4(x_3 - x_4) + c_3(\dot{x}_2 - \dot{x}_4) \\
+k_3(x_2 - x_4) - c_5(\dot{x}_4 - \dot{x}_{se}) - k_5(x_4 - x_{se})
\end{cases}
\tag{5}
$$

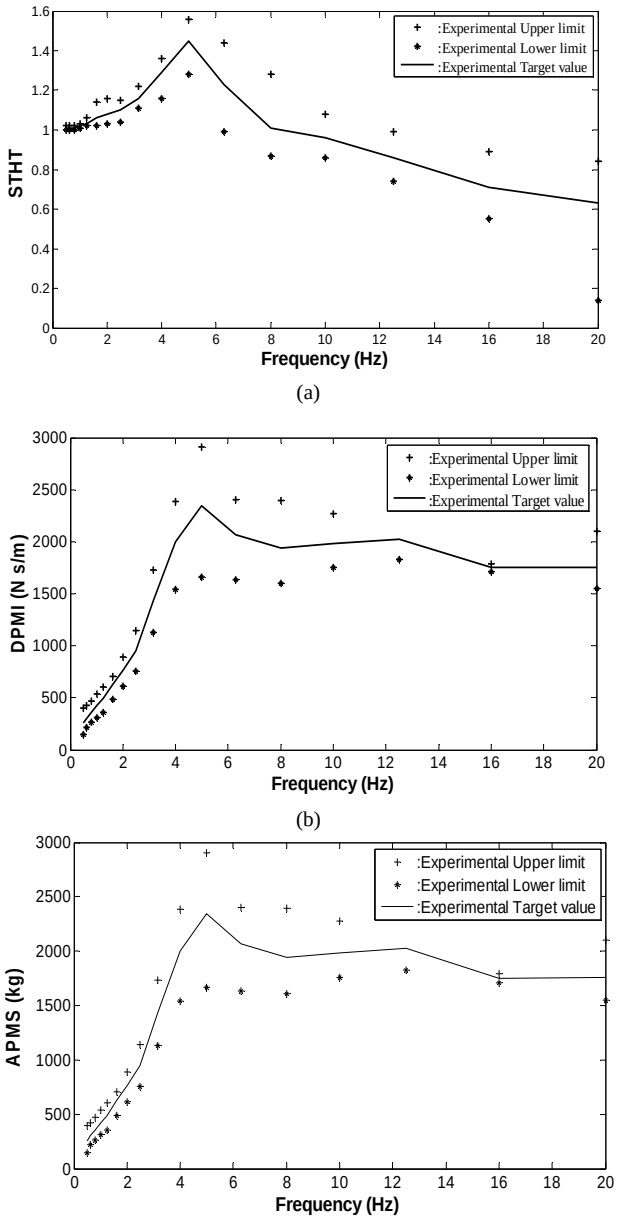

Figure 1. Experimental data of (a) STHT; (b) DPMI; and (c) APMS.

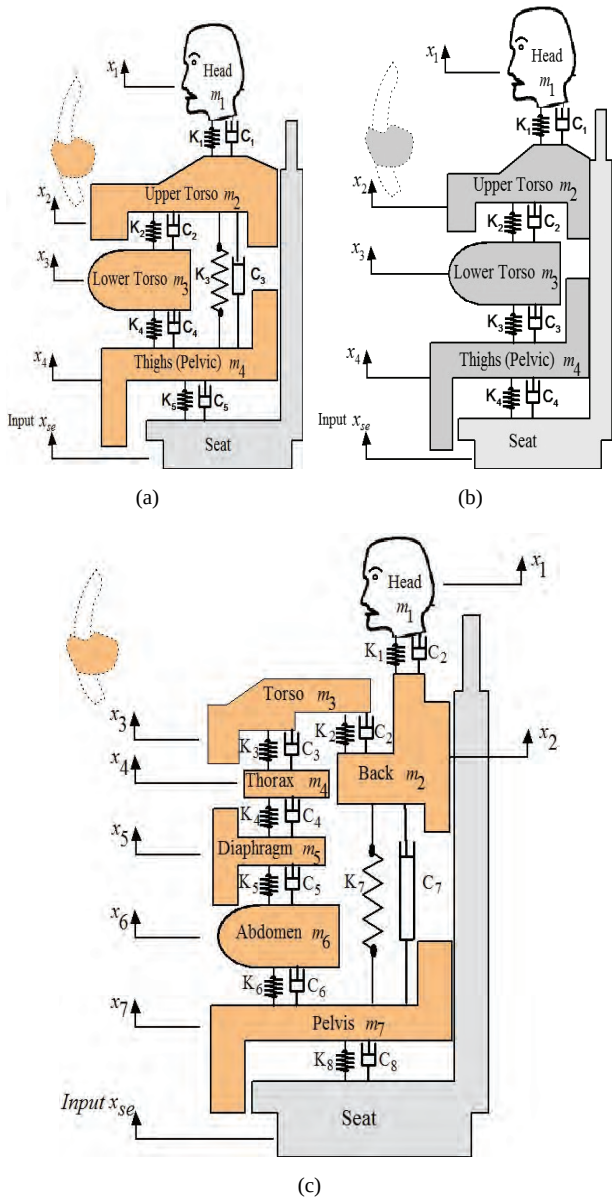

Figure 2. Biomechanical models. (a) Wan and Schimmels 4-DOF model; (b) Boileau and Rakheja 4-DOF model; and (c) Patil and Palanichamy 7-DOF model.

4.2. Boileau and Rakheja 4-DOF Model

The human-body consists of four mass segments interconnected by four sets of springs and dampers with a total mass of 55.2 kg [7], as shown in **Figure 2(b)**. The four masses represent the following four body segments: the head and neck (m_1), the chest and upper torso (m_2), the lower torso (m_3), and the thighs and pelvis in contact with the seat (m_4). The mass due to lower legs and the feet is not included in this representation, assuming their negligible contributions to the biodynamic response of the seated body. The stiffness and damping properties of

thighs and pelvis are (k_4) and (c_4), the lower torso are (k_3) and (c_3), upper torsos are (k_2) and (c_2), and head are (k_1) and (c_1). The biomechanical parameters of the model are listed in **Table 2**. The equation of motion of the human body can be obtained as follows:

$$\begin{cases} m_1 x_1^{\bullet\bullet} = -c_1(x_1^{\bullet} - x_2^{\bullet}) - k_1(x_1 - x_2) \\ m_2 x_2^{\bullet\bullet} = c_1(x_1^{\bullet} - x_2^{\bullet}) + k_1(x_1 - x_2) - c_2(x_2^{\bullet} - x_3^{\bullet}) \\ -k_2(x_2 - x_3) \\ m_3 x_3^{\bullet\bullet} = c_2(x_2^{\bullet} - x_3^{\bullet}) + k_2(x_2 - x_3) - c_3(x_3^{\bullet} - x_4^{\bullet}) \\ -k_3(x_3 - x_4) \\ m_4 x_4^{\bullet\bullet} = c_3(x_2^{\bullet} - x_4^{\bullet}) + k_3(x_2 - x_4) - c_4(x_4^{\bullet} - x_{se}^{\bullet}) \\ -k_4(x_4 - x_{se}) \end{cases} \tag{6}$$

4.3. Patil and Palanichamy 7-DOF Model

Based on Muksian's 6-DOF model, a 7-DOF nonlinear model was developed by Patil and Palanichamy [11]. In this model, the human body consists of seven mass segments interconnected by eight sets of springs and dampers, with total mass of 80 kg. The seven masses represent the following body segments: head and neck (m_1), back (m_2), upper torso (m_3), thorax (m_4), diaphragm (m_5), abdomen (m_6) and thighs and pelvis (m_7). The arms and legs are combined with the upper torso and thigh, respectively. The stiffness and damping properties of thighs and pelvis are (k_8) and (c_8), abdomen are (k_6) and (c_6), the diaphragm are (k_5) and (c_5), the thorax are (k_4) and (c_4), the torso are (k_2, k_3) and (c_2, c_3), back are (k_7) and (c_7), and head are (k_1) and (c_1). The schematic of the model is shown in **Figure 2(c)**, and biomechanical parameters of the model are listed in **Table 3**.

The equation of motion of the human-body can be obtained as follows:

$$\begin{cases} m_1 x_1^{\bullet\bullet} = -c_1(x_1^{\bullet} - x_2^{\bullet}) - k_1(x_1 - x_2) \\ m_2 x_2^{\bullet\bullet} = c_1(x_1^{\bullet} - x_2^{\bullet}) + k_1(x_1 - x_2) - c_7(x_2^{\bullet} - x_7^{\bullet}) \\ -k_7(x_2 - x_7) - c_2(x_2^{\bullet} - x_3^{\bullet}) - k_2(x_2 - x_3) \\ m_3 x_3^{\bullet\bullet} = c_2(x_2^{\bullet} - x_3^{\bullet}) + k_2(x_2 - x_3) - c_3(x_3^{\bullet} - x_4^{\bullet}) \\ -k_3(x_3 - x_4) \\ m_4 x_4^{\bullet\bullet} = c_3(x_3^{\bullet} - x_4^{\bullet}) + k_3(x_3 - x_4) - c_4(x_4^{\bullet} - x_5^{\bullet}) \\ -k_4(x_4 - x_5) \\ m_5 x_5^{\bullet\bullet} = c_4(x_4^{\bullet} - x_5^{\bullet}) + k_4(x_4 - x_5) - c_5(x_5^{\bullet} - x_6^{\bullet}) \\ -k_5(x_5 - x_6) \\ m_6 x_6^{\bullet\bullet} = c_5(x_5^{\bullet} - x_6^{\bullet}) + k_5(x_5 - x_6) - c_6(x_6^{\bullet} - x_7^{\bullet}) \\ -k_6(x_6 - x_7) \\ m_7 x_7^{\bullet\bullet} = c_6(x_6^{\bullet} - x_7^{\bullet}) + k_6(x_6 - x_7) + c_7(x_2^{\bullet} - x_7^{\bullet}) \\ +k_7(x_2 - x_7) - c_8(x_7^{\bullet} - x_{se}^{\bullet}) - k_8(x_7 - x_{se}) \end{cases} \tag{7}$$

5. Estimation of Biodynamic Response Characteristics

There are two methods to solve system equations of motion; time domain and frequency domain. Frequency domain solutions are often of more interest than the time history and can usually be performed more conveniently than in the time domain. However, for the solutions to be applicable, the equations must either be linear, or linearized. Frequency domain analysis employs the Fourier transformation.

The system equations of motion, Equations (5-7), for the model can be expressed in matrix form as follows:

$$[M]\{x^{\bullet\bullet}\} + [C]\{x^{\bullet}\} + [K]\{x\} = \{f\} \tag{8}$$

where, $[M], [C]$ and $[K]$ are $n \times n$ mass, damping, and stiffness matrices, respectively; $\{f\}$ is the force vector due to external excitation.

By taking the Fourier transformation of equation (8), the following matrix form of equation can be obtained**:**

$$\{X(j\omega)\} = \left[[K] - \omega^2[M] + j\omega[C]\right]^{-1}\{F(j\omega)\} \tag{9}$$

where, $\{X(j\omega)\}$ and $\{F(j\omega)\}$ are the complex Fourier transformation vectors of $\{x\}$ and $\{f\}$ respectively. ω is the excitation frequency. Vector $\{X(j\omega)\}$ contains complex displacement responses of n mass segments as a function of ω

$$(\{x_1(j\omega), x_2(j\omega), x_3(j\omega), ...x_n(j\omega)\}).$$

$\{F(j\omega)\}$, consists of complex excitation forces on the mass segments as a function of ω as well.

The driving-point mechanical impedance is defined as the ratio of driving force (summation of spring and damping forces between pelvis and seat) to the driving-point velocity (input velocity of the seat). Accordingly, DPMI can be represented as follows (e.g. Boileau and Rakheja, model):

$$DPMI(j\omega) = \left|(c_4 + \frac{k_4}{j\omega})\frac{x_4(j\omega)}{x_0(\omega)} - (c_4 + \frac{k_4}{j\omega})\right| \tag{10}$$

Seat-to-head transmissibility is defined as the ratio of output responses (head) to input excitation.

$$STHT(j\omega) = \frac{x_1(j\omega)}{x_0(j\omega)} \tag{11}$$

Apparent mass, can be expressed in terms of DPMI, Equation (3), as follows (e.g. Boileau and Rakheja model):

$$\begin{aligned} APMS(j\omega) &= \left|\frac{DPMI(j\omega)}{j\omega}\right| \\ &= \left|(\frac{c_4}{j\omega} + \frac{k_4}{-\omega^2})\frac{x_4(j\omega)}{x_0(j\omega)} - (\frac{c_4}{j\omega} + \frac{k_4}{-\omega^2})\right| \end{aligned} \tag{12}$$

Table 1. The biomechanical parameters of the Wan and Schimmels model (Before and after optimization).

Mass (kg)	Damping coefficient (N.s/m)		Spring constant (N/m)	
	Before	After	Before	After
m_1 = 4.17	c_1 = 250	c_1 =310	k_1 = 134400	k_1 = 166990
m_2 = 15	c_2 = 200	c_2 =200	k_2 = 10000	k_2 = 10000
m_3 = 5.5	c_3 = 909.1	c_3 = 909.1	k_3 = 192000	k_3 = 144000
m_4 = 36	c_4 = 330	c_4 =330	k_4 = 20000	k_4 = 20000
-	c_5 = 2475	c_5 =2475	k_5 = 49340	k_5 =49340

6. Development of Models

Many biodynamic models have been derived using trial and error curve-fitting technique, such that the error between the computed and measured biodynamic response functions is minimum. Such curve-fitting methods may lead to a proper fit over a specific frequency range, but rarely provide good results when extended over a broad frequency range. Alternatively, nonlinear programming based optimization techniques may be effectively employed to determine the model parameters, involving the use of a constrained optimization algorithm in conjunction with well defined biodynamic response function [14]. A constrained objective function may be defined to minimize the error between the computed and the target values of specific biodynamic response function over a specific frequency range.

Optimization software based on stochastic techniques search methods, Genetic algorithms (GAs), is employed to determine the human model parameters imposing some limit constraints on the model parameters. An objective function is formulated comprising the sum of errors between the computed and of the driving-point mechanical impedance, apparent mass and seat-to-head transmissibility functions. The model thus derived can provide reasonable correlation with the impedance, apparent mass and transmissibility characteristics.

Starting with an assumed set of model parameters, the differential equations of motion are solved for unit displacement excitation to drive the driving-point mechanical impedance using Equation (1), apparent mass using Equation (3), and seat-to-head transmissibility using Equation (4). At each iteration of search, the sum of square errors defined by an objective function over the entire frequency range is examined, and the procedure is re-initiated with modified parameter values when the error exceeds that from the previous search. The search is terminated when the computed error approaches the minimum value.

6.1. Objective Function

The objective function is selected to comprise the squared sum errors associated with driving-point mechanical impedance (U_1) apparent mass (U_2) and seat-to-head transmissibility functions (U_3) to minimize the error between the computed and the target values. This study used the classical weighted sum approaches to solve a multi-objective optimization problem as follows:

$$OBJ = W_1.(U_1) + W_2.(U_2) + W_3.(U_3) \tag{13}$$

where,

$$U_1 = \sum_{i=1}^{n}\left[\left|DPMI(j\omega_i)\right| - \left|DPMI_t(j\omega_i)\right|\right]^2,$$

$$U_2 = \sum_{i=1}^{n}\left[\left|APMS(j\omega_i)\right| - \left|APMS_t(j\omega_i)\right|\right]^2,$$

$$U_3 = \sum_{i=1}^{n}\left[\left|STHT(j\omega_i)\right| - \left|STHT_t(j\omega_i)\right|\right]^2$$

In the above equations $\left|DPMI_t(j\omega_i)\right|$, $\left|APMS_t(j\omega_i)\right|$ and $\left|STHT_t(j\omega_i)\right|$ are the target values of driving-point mechanical impedance, apparent mass, and seat-to-head transmissibility, respectively. The target values of DPMI, APMS, and STHT are illustrated in **Figure 1**. W_1, W_2 and W_3 are weighting factors to emphasize the relative importance of the terms.

The limit constraints are calculated as ±25% variations about the biomechanical parameters of the three models.

6.2. Evaluation of Biodynamic Seated Human Models

To evaluate the prediction accuracy of each human model in comparison with experimental results from literature, the ratio of the root-mean-square error to the mean value is calculated with the following equation:

$$\text{Goodness of fit } (\varepsilon) = \frac{\sqrt{\sum(\tau_e - \tau_c)^2/(N-2)}}{\sum \tau_e / N} \tag{14}$$

where τ_e is the test datum, τ_c is the calculated result from each model, and N is the number of test data points used in the comparison. The fit of predicted results to test data is perfect when ε is equal to 1. The predictions on seat-to-head transmissibility, the driving-point mechanical impedance, and apparent mass for each lumped-parameter model will be compared using Equation (14) to obtain prediction accuracy.

7. Results and Discussion

1) Wan and Schimmels modified model

The solution of the constrained optimization problem,

Equation (5), resulted in an optimized model parameters are listed in **Table 1**. **Figure 3** presents a comparison of the driving-point mechanical impedance, apparent mass, and seat-to-head transmissibility with the target data, respectively. It is obvious that the developed model better fits target values compared with Wan and Schimmels model. The calculated goodness of fit for seat-to-head transmissibility is 92% compared to 90.9% for Wan and Schimmels model.

On the other hand, the developed model matches the target values better with a goodness of fit of 82.1% for driving-point mechanical impedance and 87.1% apparent mass compared to 80.1% and 86.8%, for Wan and Schimmels model, respectively.

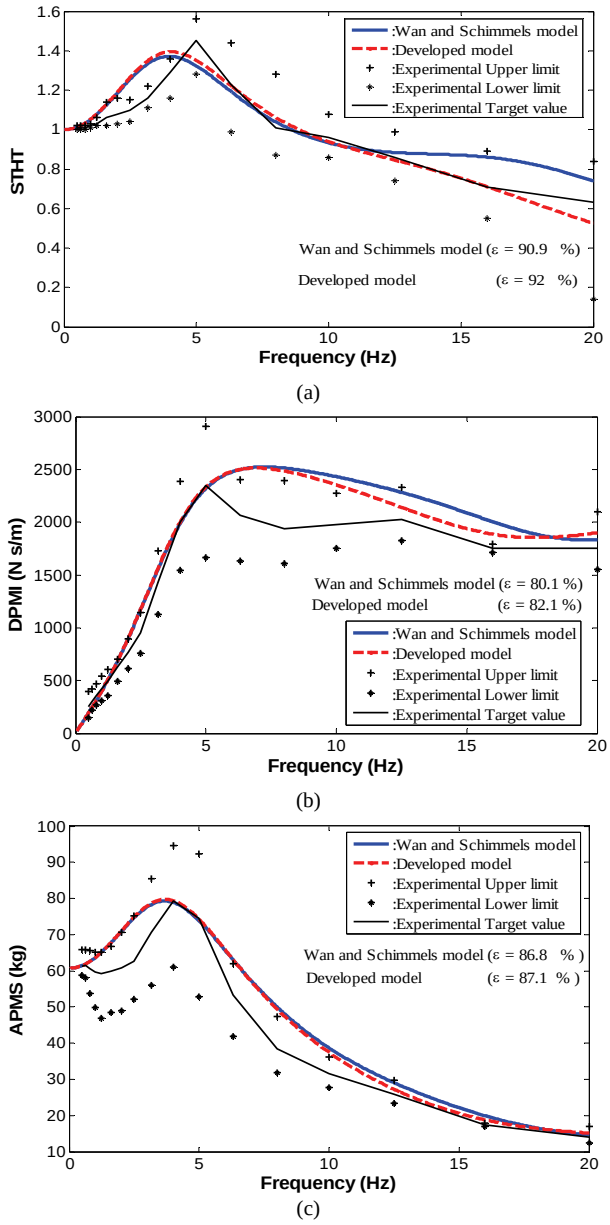

Figure 3. Comparison of biodynamic response characteristics for Wan model, and optimized model with the target data.

In addition, the peak values of the Wan and Schimmels model occur at 4 Hz for seat-to-head transmissibility, 3.7 Hz for apparent mass, and 7.2 Hz for driving-point mechanical impedance, whereas for the optimized model, they occur at 4.05, 3.8 and 6.9 Hz, respectively.

2) Boileau and Rakheja modified model

The solution of the constrained optimization problem, Equation (6), resulted in optimized model parameters which are listed in **Table 2**.

Simulation results are illustrated in **Figure 4**. This figure presents a comparison of the driving-point mechanical impedance, apparent mass and seat-to-head transmissibility with the target data, respectively. It is obvious that the optimized model better fits target values than the Boileau and Rakheja model; with a goodness of fit for seat-to-head transmissibility is 80.6%, compared to 76.8% for the Boileau and Rakheja model.

In addition, the developed model matches the target values better with a goodness of fit of 84% for driving-point mechanical impedance compared to 80.1% for Boileau and Rakheja model. Optimized model matches the target values better with a goodness of fit of 87% for apparent mass compared to 86.7% for the Boileau and Rakheja model.

On the other hand, the peak values of the Boileau and Rakheja model occur at 4.7 Hz for seat-to-head transmissibility, 4.6 Hz for apparent mass, and 5.5 Hz for driving-point mechanical impedance, whereas for the optimized model, they occur at 4.95, 4.55 and 5.9 Hz, respectively.

3) Patil and Palanichamy modified model

In a similar way, the solution of the constrained optimization problem, Equation (7), resulted in an optimized of the following model parameters are listed in **Table 3**. **Figure 5** presents a comparison of the driving-point mechanical impedance, apparent mass, and seat-to-head transmissibility with the target data, respectively. It was observed that the developed model better fits target values compared the Patil and Palanichamy model, with a goodness of fit for seat-to-head transmissibility is 35% compared to 22% for Patil and Palanichamy model. On the other hand, the developed model matches the target values better with a goodness of fit of 13% for driving-point mechanical impedance compared to 1% for Patil and Palanichamy model. The developed model matches the target values with a goodness of fit of 34% for apparent mass compared to 0% for Patil and Palanichamy model.

Table 2. The biomechanical parameters of the Boileau and Rakheja model (Before and after optimization).

Mass (kg)	Damping coefficient (N.s/m)		Spring constant (N/m)	
	Before	After	Before	After
m_1 = 5.31	c_1 = 400	c_1 =460	k_1 = 310000	k_1 = 356370
m_2 = 28.49	c_2 = 4750	c_2 =5400	k_2 = 183000	k_2 = 208570
m_3 = 8.62	c_3 = 4585	c_3 =5190	k_3 = 162800	k_3 = 187110
m_4 = 12.78	c_4 = 2064	c_4 =2370	k_4 = 90000	k_4 = 103480

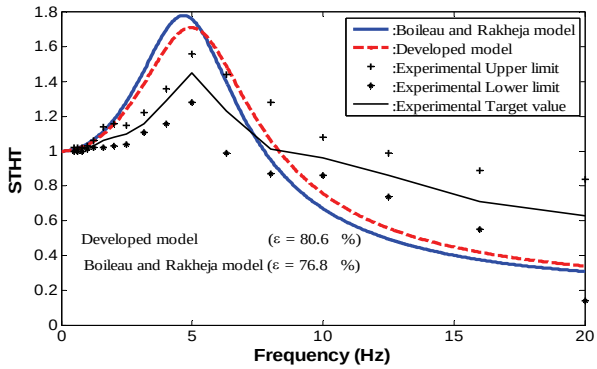

(a)

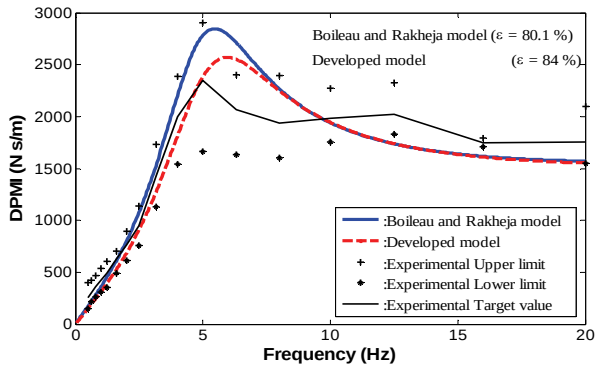

(b)

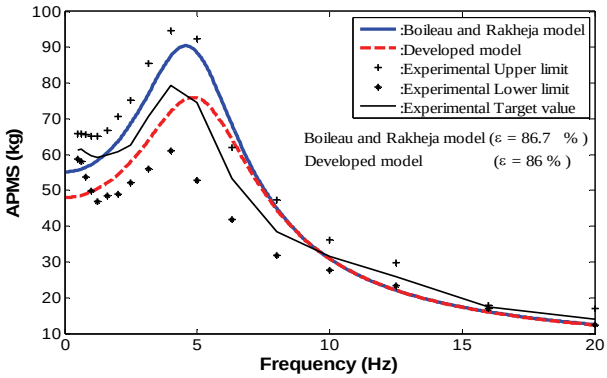

(c)

Figure 4. Comparison of biodynamic response characteristics for Boileau model, and optimized model with the target data.

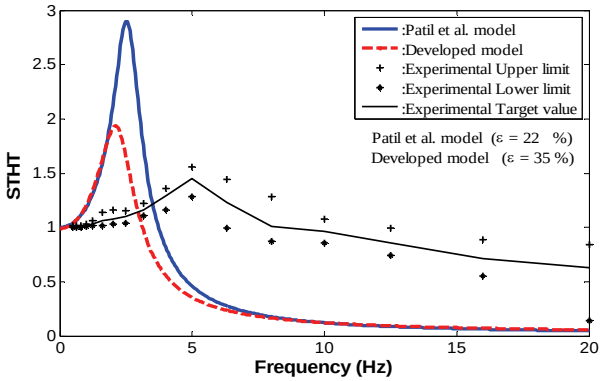

(a)

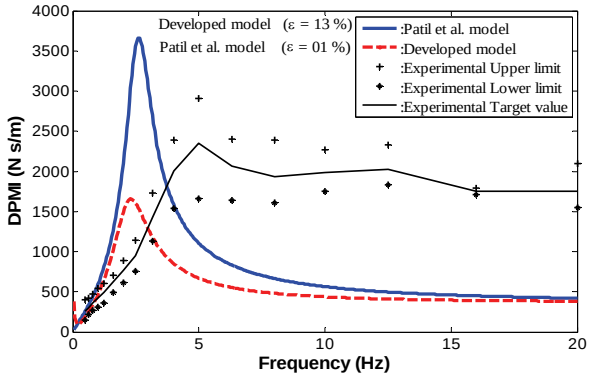

(b)

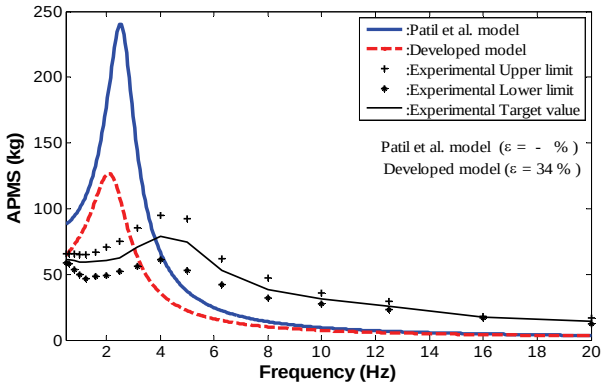

(c)

Figure 5. Comparison of biodynamic response characteristics for Patil model, and optimized model with the target data.

In addition, the peak values of Patil and Palanichamy model occur at 2.5 Hz for seat-to-head transmissibility, 2.5 Hz for apparent mass, and 2.6 Hz for driving-point mechanical impedance, whereas for the developed model, they occur at 2.1, 2.1 and 2.3 Hz, respectively.

The simulations of the three lumped-parameter models listed in this study for seated human subjects exposed to vertical vibration exposure are listed in **Table 4**. It is observed that the 4-DOF optimization of Wan and Schimmels can give the best estimation on seat-to-head transmissibility with goodness of fit values of 92%. The

Table 3. The biomechanical parameters of the Patil and Palanichamy model (Before and after optimization).

Mass (kg)	Damping coefficient (N.s/m)		Spring constant (N/m)	
	Before	After	Before	After
m_1 = 5.55	c_1 =3651	c_1 =3542	k_1 = 53640	k_1 = 41978
m_2 = 6.94	c_2 =3651	c_2 =2685	k_2 = 53640	k_2 = 40943
m_3 = 33.33	c_3 =298	c_3 =351	k_3 =8941	k_3 =1001
m_4 = 1.389	c_4 =298	c_4 =237	k_4 =8941	k_4 =845
m_5 = 0.4629	c_5 =298	c_5 =354	k_5 =8941	k_5 =1052
m_6 = 6.02	c_6 =298	c_6 =225	k_6 =8941	k_6 =1035
m_7 = 27.7	c_7 =3651	c_7 =2929	k_7 = 53640	k_7 = 39575
	c_8 =378	c_8 =463	k_8 = 25500	k_8 = 19325

goodness of fit is 82.1% for driving-point mechanical impedance. On the other hand, the development model matches the target values better with a goodness of fit of 87.1% for apparent mass compared to all models.

8. Conclusions and Recommendations

A study on the biodynamic models of seated human subjects exposed to vertical vibration is carried out. A three lumped-parameter models from literature have also been analyzed and optimized using genetic algorithms to match an experimental data in terms of STH transmissibility, DPM impedance, and AP mass. It is shown that the optimized 4-DOF Wan and Schimmels model can give the best estimation on STH transmissibility, DPM impedance, AP mass with goodness of fit values of 91.2%, 82.1%, and 87.1%, respectively. In addition, it has the highest average of goodness of fit (87%). So, this model is recommended for the study of biodynamic responses of seated human subjects exposed to vertical whole body vibration. The biomechanical parameters of the Wan and Schimmels model that match the experimental data was changed for the head as c_1 = 310 N.s/m and k_1 = 166990 N/m, respectively; and for upper torso stiffness as k_3 = 144000 N/m. From the model, the main body resonant frequencies computed on the basis of both biodynamic response functions are found to be within close bounds to that expected for the human body.

Table 4. Result of STHT, DPMI, and APMS for different models.

DOF	Model Name	STHT		DPMI		APMS		Goodness of fit average (%)
		Peak frequency (Hz)	Goodness of fit (%)	Peak frequency (Hz)	Goodness of fit (%)	Peak frequency (Hz)	Goodness of fit (%)	
	Target values	**5.1**		**4.8**		**4.4**		
4	**Wan model**	**4**	**90.9**	**7.2**	**80.1**	**3.7**	**86.8**	**85.8**
	Optimized Wan model	**4.05**	**92**	**6.9**	**82.1**	**3.8**	**87.1**	**87**
4	**Boileau model**	**4.7**	**76.8**	**5.5**	**80.1**	**4.6**	**86.7**	**81.2**
	Optimized Boileau	**4.95**	**80.6**	**5.9**	**84**	**4.55**	**87**	**83.86**
7	**Patil model**	**2.5**	**22**	**2.6**	**1**	**2.5**	**0**	**7.67**
	Optimized Patil model	**2.1**	**35**	**2.3**	**13**	**2.1**	**34**	**27.7**

This research provides a comprehensive understanding of the aforementioned biodynamic responses. Future research may be extended to the following:

1) Therefore, further research can be conducted on the other lumped-parameter models from literature. This work will be done after applying an optimization processes to determine the much closer one that match experimental data to STH transmissibility, DPM impedance, and AP mass values.

2) Quarter, semi, and full car suspension system including seat-human car suspension system should be analyzed and validated to find the actual frequency responses of driver parts.

9. References

[1] G. Salvendy, "Handbook of Human Factors and Ergonomics," 2nd Edition, John Wiley & Sons, Inc., New York, 2005.

[2] ISO 2631-1, "Mechanical Variation and Shock - Evaluation of Human Exposure to Wholebody Vibration. Part I: General Requirements," *Technology Report*, International Organization for Standardization, 1997.

[3] X. Wu, S. Rakheja and P.-E. Boileau, "Analyses of Relationships between Biodynamic Response Functions," *Journal of Sound and Vibration*, Vol. 226, No. 3, 1999, pp. 595-606.

[4] R. R. Coermann, "The Mechanical Impedance of the Human Body in Sitting and Standing Position at Low Frequencies," *Human Factors*, October 1962, pp. 227-253.

[5] C. W. Suggs, C. F. Abrams and L. F. Stikeleather, "Application of a Damped Spring-Mass Human Vibration Simulator in Vibration Testing of Vehicle Seats," *Ergonomics*, Vol. 12, No. 1, 1969, pp. 79-90.

[6] V. K. Tewari and N. Prasad, "Three-DOF Modelling of

Tractor Seat-Operator System," *Journal of Terramechanics*, Vol. 36, No. 4, 1999, pp. 207-219.

[7] P. E. Boileau and S. Rakheja, "Whole-Body Vertical Biodynamic Response Characteristics of the Seated Vehicle Driver: Measurement and Model Development," *International Journal of Industrial Ergonomics*, Vol. 22, No. 6, 1998, pp. 449-472.

[8] Z. Zong and K. Y. Lam, "Biodynamic Response of Shipboard Sitting Subject to Ship Shock Motion," *Journal of Biomechanics*, Vol. 35, No. 1, 2002, pp. 35-43.

[9] X. X. Liu, J. Shi and G. H. Li, "Biodynamic Response and Injury Estimation of Ship Personnel to Ship Shock Motion Induced by Underwater Explosion," *Proceeding of* 69*th Shock and Vibration Symposium*, Vol. 18, St. Paul, 1998, pp. 1-18.

[10] R. Muksian and C. D. Nash, "A Model for the Response of Seated Humans to Sinusoidal Displacements of the Seat," *Journal of Biomechanics*, Vol. 7, No. 3, 1974, pp. 209-215.

[11] M. K. Patil, M. S. Palanichamy and N. G. Dhanjoo, "Minimization of the Verticale Vibrations Sustained by a Tractor Operator, By Provision of a Standard-Type Tractor Seat Suspension," *ANNALS of Biomedical Engineering*, Vol. 6, 1978, pp. 138-153.

[12] C. C. Liang and C. F. Chiang, "A Study on Biodynamic Models of Seated Human Subjects Exposed to Vertical Vibration," *International Journal of Industrial Ergonomics*, Vol. 36, No. 10, 2006, pp. 869-890.

[13] A. E. Baumal, J. J. McPhee and P. H. Calamai, "Application of Genetic Algorithms to the Design Optimization of an Active Vehicle Suspension System," *Computer Methods in Applied Mechanics and Engineering*, Vol. 163, No. 1, 1998, pp. 87-94.

[14] P.-E. Boileau, "A Study of Secondary Suspensions and Human Drivers Response to Whole-Body Vehicular Vibration and Shock," Ph.D. Thesis, Concordia University, Montreal, Quebec, 1995.

[15] W. Wang, "A Study of Force-Motion and Vibration Transmission Properties of Seated Body under Vertical Vibration and Effects of Sitting Posture," Ph.D. Thesis Concordia University, Montreal, Quebec, 2006.

[16] Y. Huang, "Mechanism of Nonlinear Biodynamic Response of the Human Body Exposed to Whole-Body Vibration," Ph.D. Thesis, University of Southampton, 2008.

[17] C. C. Liang and C. F. Chiang, "Modeling of a Seated Human Body Exposed to Vertical Vibrations in Various Automotive Postures," *Industrial Health*, Vol. 46, No. 2, 2008, pp. 125-137.

[18] X. Wu, "A Study of Driver-Seat Interaction and Enhancement of Vehicular Ride Vibration Environment," PhD. Thesis Concordia University, Montreal, Quebec, 1998.

[19] Y. Wan and J. M. Schimmels, "A Simple Model that Captures the Essential Dynamics of a Seated Human Exposed to Whole Body Vibration," *Advances in Bioengineering, ASME*, Vol. 31, 1995, pp. 333-334.

Engineering, 2010, 2, 720-726
doi:10.4236/eng.2010.29093 Published Online September 2010 (http://www.SciRP.org/journal/eng)

Finite Element Analysis of Contact Pressures between Seat Cushion and Human Buttock-Thigh Tissue

Chak Yin Tang, Wai Chan, Chi Pont Tsui
[1]*Department of Industrial and Systems Engineering, Hong Kong Polytechnic University, Hong Kong, China*
E-mail: *mfgary@inet.polyu.edu.hk*
Received May 19, 2010; *revised July* 21, 2010; *accepted August* 6, 2010

Abstract

Unrelieved pressure on load-bearing muscle tissues of humans can produce pressure ulcers. In a seated upright posture, the highest pressures occur inferior to the ischial tuberosities (ITs). Moreover, the vibration can initiate the development of pressure ulcer. Therefore, the seat cushion is not only used to lower the maximum seating pressure on buttocks but also minimize the transmission of vibration to human body. The purpose of this study was to investigate the effects of varying vertical vibration frequencies on seat-interface contact pressure during sitting on three different seat cushions by using a finite element modeling approach. A simplified two-dimensional human buttock-thigh model was developed to simulate the mechanical response of the muscle of buttocks and thigh under vertical vibration. Static and vibrational loads with five different frequencies of 0.1, 1, 10, 30 and 50 Hz and the same amplitude of 3 mm were applied to different seat cushions. The result showed that the "SAF 6060" seat cushion with both hyperelastic and viscoelastic behaviors could be effective in reducing the amplitude of varying maximum contact pressure, especially for the frequency of 10-20 Hz. This method could help in design of seat cushions with appropriate material properties and shape so as to reduce vibrations transmitted to human body at a certain frequency range.

Keywords: Finite Element Analysis, Seat Cushion, Vibration, Buttock-Thigh

1. Introduction

Static seating comfort is important for drivers and wheelchair users. Seat-interface pressure distribution has been used as an objective measure for discomfort prediction [1]. Experimental methods could find the interface pressure between human body and seat. However, it could not provide the information about subcutaneous stress and deformations of soft tissues. For drivers and wheelchair users who have sat for a long time, they could be associated with an increased risk of pressure ulcers [2]. Moreover, severe pressure ulcer initiates in muscle tissue overlying a bony prominence (ischial tuberosity) and progresses outwards through fat and skin, giving rise to the subcutaneous stress [3,4]. Many researchers conducted two-dimensional (2D) and three-dimensional (3D) finite element analyses to investigate the subcutaneous stress [1,5-12]. Ragan *et al.* determined the effects of the thickness of polymer foam wheelchair cushions on subcutaneous pressures during seating by using a finite element approach [8]. It was found that seat-interface pressures were a good indicator for reducing the subcutaneous stress.

Shocks normal to the seat cushions and shear stresses could initiate the development of pressure ulcer [13,14]. Following the directive 2002/44/EC of the European Parliament, manufacturers of seat cushions were required to limit vibration exposure to users. Wu *et al*., [15] found that the maximum ischium pressure and the effective contact area on a soft seat occur near resonant frequency of the coupled human-seated system (2.5-3.0 Hz), and generally increased considerably with increase in the magnitude of vibration excitation. DiGiovine *et al*., [16] discussed that the application of the appropriate seating system may reduce the amount of whole-body vibration experienced by an individual during manual wheelchair propulsion, They also suggested the manufacturers should concentrate on designing seat cushions that shift the resonant frequency away from the range of frequencies most sensitive to humans during whole-body vibration (4-12.5 Hz) as defined in ISO 2631-1:1997 [17].

Owing to these reasons, many researchers developed a

biomechanical model of human body for investigating the dynamic response to vertical vibrations. Verver *et al.*, [18] developed a finite element model for the human body using MADYMO while Siefert *et al.* [9] used CASIMIR for model creation. However, for their models, only hyperelastic behavior was used to describe the seat cushion and human soft tissue but their viscoelastic properties were not considered. Kitazaki and Griffin [19] used beam, spring and mass elements to model a 2D human model including the spine, viscera, head, pelvis and buttocks tissue. This model was good for estimating the transmission capability from vertical seat motion to vertical spinal motion. Other methods such as lumped parameter model [20,21] and finite segment model [22] were also used to evaluate the whole-body vibration . However, these two methods could not present realistic human geometry. Other researchers experimentally determined if seat cushions of a selected wheelchair could minimize the transmission of vibrations to users [16,23, 24].

The main goal of our study was to investigate the effects of vertical vibration on subcutaneous stress of buttocks sitting on three different seat cushions by using a finite element modeling approach. The simplified buttock-thigh model was developed for the analysis. The hyperelastic and viscoelastic properties were used to describe the mechanical behaviors of the human soft tissue and seat cushion.

2. Methodology

2.1. Buttock-Thigh Model

Figure 1 shows the buttock-thigh model consisting of a femur and ischial tuberosity (IT) for representing humans in a sitting posture. It was assumed that a human sit uprightly on the cushion and there was no support on the feet. The total length of the buttock-thigh model was 60 cm for the male at the fifty-percentile [25]. A circle with a radius of 1cm represents the cross section of the IT where supports the body's weight in a sitting position. The distance between the bottom of the IT and the skin was 4 cm [8]. The thickness of the cushion was set to 8 cm because Chow and Odell [26] found that the cushion thickness beyond 8cm was ineffective in further reducing subcutaneous stress. The distance between the buttock-thigh model and the cushion was set to 1 cm at the beginning step because the buttocks were assumed not to sit on the cushion initially. With the finite element tool – ABAQUS, the buttock-thigh model and seat cushion were meshed using 2D plane strain elements as shown in **Figure 2**.

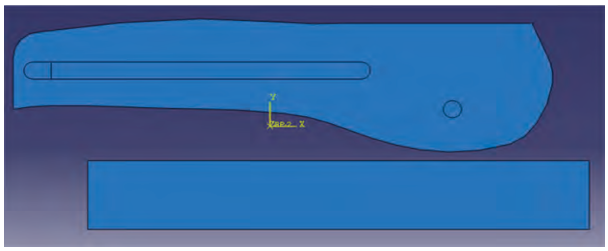

Figure 1. The buttock-thigh model and the cushion.

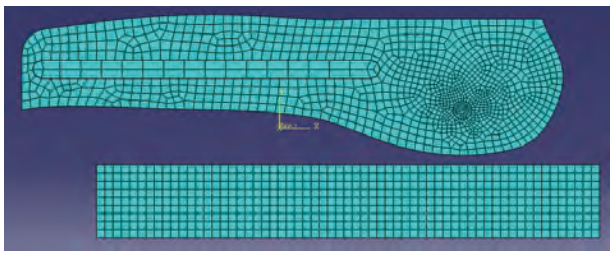

Figure 2. Finite element model of the buttock-thigh model and the cushion.

2.2. Material Models

The muscle and seat cushions were assigned different material properties. All bones in the model were defined as rigid bodies, because their stiffness is very high as compared to the muscle and cushion.

2.2.1. Seat Cushions

Three different material properties of seat cushions were considered in this study. One of the seat cushions was assumed to be made of SAF 6060 polymer foam with rate-independent hyperelastic and viscoelastic behaviors, which was produced by Foam Partner Fritz Nauer AG. Another two seat cushions were similar to the above-mentioned SAF6060 cushion but with a linear elastic response instead of the hyperelastic behavior. The Young moduli of these two cushions were separately set to 15 kPa (Elastic 15000) and 20 kPa (Elastic 20000), while their Poisson's ratio was 0.3 [27].

The hyperealstic behavior of the seat cushion SAF6060 was represented using a non-linear isotropic compressible hyperelastic soft foam material model or a so-called hyperfoam. The hyperelastic behavior of the foam material is described by the strain energy potential, U in the following form:

$$U = \sum_{i=1}^{N} \frac{2\mu_i}{\alpha_i^2}\left[\hat{\lambda}_1^{\alpha_i} + \hat{\lambda}_2^{\alpha_i} + \hat{\lambda}_3^{\alpha_i} - 3 + \frac{1}{\beta_i}\left(\left(J^{el}\right)^{-\alpha_i\beta_i} - 1\right)\right] \quad (1)$$

where N is the order of the strain energy potential, μ_i, α_i and β_i are the temperature-dependent material parameters; $\hat{\lambda}_i = (J^{th})^{-\frac{1}{3}}\lambda_i$, $\hat{\lambda}_1\hat{\lambda}_2\hat{\lambda}_3 = J^{el}$ and λ_i are the principal stretches. J^{el} is the ratio of elastic-deformation to

volume-change and J^{th} is the ratio of the thermal-strain to volume-change. The coefficients μ_i are related to the initial shear modulus while the coefficient β_i determines the degree of compressibility and is related to the Poisson's ratio [28]. In the present work, polyurethane soft foam parameters determined by Schrodt *et al.* [29] from uniaxial compression tests were used to define the above-mentioned material parameters for SAF 6060 cushion as listed in **Table 1**. Moreover, its density was set to 60 kg/m^3 and a second order (N = 2) of the strain energy potential was used.

The viscoelastic behavior of the SAF 6060 cushion was defined by using a time-based Prony-series model for the shear modulus only because the time-dependency of bulk modulus is generally not significant [5]. Time-dependent shear relaxation modulus *G(t)* is given by

$$G(t) = G_0 - \sum_{i=1}^{N} G_i \left(1 - e^{-t/\tau_i^G}\right) \quad (2)$$

where τ_i^G is the relaxation time and N is the order of the Prony series. G_0 and G_i are the instantaneous shear modulus and relative shear modulus, respectively. With reference to the findings by the work of Grujicic *et al.* [5], the viscoelastic material parameters for the SAF 6060 cushion were defined such that N = 2, G_1 = 0.3003 and τ_1 = 0.010014 s, and G_2 = 0.1997 and τ_2 = 0.1002 s.

2.2.2. Muscle

The muscular portion of the buttock-thigh model was modeled using a non-linear visco-hyperelastic isotropic material model to describe the human soft tissue. The density of soft tissue is 1000 kg/m^3 [30] and hyperelastic portion of the soft tissue is expressed in the form of the polynomial strain energy potential, W:

$$W = \sum_{i+j=1}^{N} C_{ij} \left(\bar{I}_1 - 3\right)^i \left(\bar{I}_2 - 3\right)^j + \sum_{i=1}^{N} \frac{1}{D_i} (J^{el} - 1)^{2i} \quad (3)$$

where C_{ij} and D_i are the material parameters. A higher N value may provide a better fit to the exact solution. However, it may cause numerical difficulty in fitting the material constants and require enough data to cover the entire range of interest of deformation. Therefore a very higher N value is not usually recommended. In the present study, N = 2 was chosen and the hyperelastic parameters for the muscle model obtained from a URL, http://lyle.smu.edu/~hyao/academics.html#Research are listed in **Table 2**. Referring to the work of Tang and Tsui [31], the viscoelastic parameters for the muscle model were set as G_1 = 0.5, K_1 = 0.5 and τ_1 = 0.8 s.

2.3. Simulation Set-Up

In the present study, ABAQUS explicit dynamics analysis has been performed to deal with the dynamic problem. As this type of analysis uses a consistent large-deformation theory, the cushion and the muscle model could undergo large rotations and deformation. The analysis procedure was implemented by using an explicit integration rule and diagonal element mass matrices. The equations of motion for the body were integrated using the following explicit central-difference integration rule:

$$\dot{u}^N_{(i+\frac{1}{2})} = \dot{u}^N_{(i-\frac{1}{2})} + \frac{\Delta t_{(i+1)} + \Delta t_i}{2} \ddot{u}^N_{(i)}$$

and

$$u^N_{(i+\frac{1}{2})} = u^N_{(i)} + \Delta t_{(i+1)} \dot{u}^N_{(i+\frac{1}{2})}$$

where u^N is a degree of freedom (a displacement or rotation component) and the subscript i refers to the increment number in an explicit dynamics step. The central-difference integration operator is explicit such that the kinematic state is advanced using known values of $\dot{u}^N_{(i+1/2)}$ and $\ddot{u}^N_{(i)}$ from the previous increment [28].

2.4. Interaction between the Buttock-Thigh Model and Cushion

In this work, it was assumed that the human sit on the cushion and then the vertical vibration was applied onto the bottom of the cushion. The loading was applied to the model due to the weight of the human, such that a gravity-based body force was used to prescribe the loading. The interaction between the buttock-thigh model and the cushion was analyzed in ABAQUS/Explicit using a penalty contact method with finite-sliding. Surface-to-surface contact with a coefficient of friction of 0.5 [5] was used to define the contact pair between the buttock-thigh model and cushion. The outer surface of the buttock-thigh model was defined as the "master surface" which has a larger surface and higher stiffness, while the surface of the cushion was defined as the "slave surface" which is softer and has smaller surface than that of the buttock-thigh model. The surfaces between the bone and muscle were tied together so that there was no relative motion between them.

Table 1. Hyperelastic material parameters for the SAF6060 cushion.

μ_1 [MPa]	α_1	β_1	μ_2 [MPa]	α_2	β_2
0.481 × 10^{-2}	0.198 × 10^2	0.145 × 10^{-1}	0.36 × 10^{-2}	0.198 × 10^2	0.65 × 10^{-2}

Table 2. Hyperelastic material parameters for the muscle model (All values in MPa).

C_{10}	C_{01}	C_{20}	C_{11}	C_{02}	D_1	D_2
0.08556	−0.05841	0.039	−0.02319	0.00851	3.65273	0

2.5. Loading and Boundary Conditions

According to fifty-percentile male body segment masses [25], the total weight is 80.4 kg, including 54.5 kg of the upper body and 25.9 kg of the lower body. The current model represented only one side of the body so that the mass assigned to the model should be halved. Thus, the weight of the upper body on the iscahial tuberosity was set as 27.3 kg while the weight of lower leg on the femur was set as 4.5 kg. **Figure 3** shows the positions of the assigned masses. It was assumed that the cushion was placed on a rigid surface so that the bottom surface of the cushion was restricted to move in all directions. Moreover, the upper surface of the buttock-thigh model was limited to move in *X*-direction only.

The analyses were performed in two steps. In the first step, the buttock-thigh model moved to sit on the seat cushion due to the gravity load (9.81 ms^{-2}). After 15 seconds, there followed a second step in which a vertical vibration in the form of harmonic motion was applied onto the bottom of the cushion. The periodic definition method was used to define the amplitude. The frequencies of the vibration were chosen to be 0.1, 1, 10, 20 and 50 Hz which are the frequencies generated mostly in our life according to **Table 3** [32]. A vibration amplitude of 3 mm was applied to the bottom of the cushion. Each vibration case was conducted for 50 cycles (see **Table 4**).

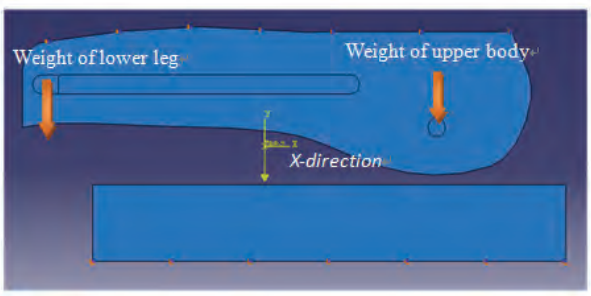

Figure 3. Loading and boundary conditions on the buttock-thigh model and cushion.

Table 3. Sensitivity of human systems to vibration.

Frequency Level	Frequency range	Sensitivity	Vibration Generator
Low	0 to 1-2 Hz	Vestibular system	Ships, cranes, aircrafts
Middle	2 to 20-30 Hz	Biomechanics: body resonances	Vehicles, aircrafts
High	> 20 Hz	Somesthetic receptors in muscles, tendons, skins	Tools, machinery

Table 4. Different loading conditions for the simulation.

	Loading					
	Gravity	Vertical vibration of 0.1 Hz	Vertical vibration of 1 Hz	Vertical vibration of 10 Hz	Vertical vibration of 20 Hz	Vertical vibration of 50 Hz
Duration (Second)	15	500	50	5	2.5	1

3. Results and Discussions

As the distribution of the contact pressure at the seated human/cushion contact interface is important for determining the seating comfort [5], the maximum contact pressure at three different locations of the three cushions at the frequency of 20 Hz have been identified as shown in **Figure 4**. Among them, the SAF 6060 cushion shows the lowest contact pressure at the locations of A and B. As the location B is under the ichial tuberosities (IT), minimizing the contact pressure at this location means minimizing the stress under IT. It can also be observed from **Figure 5** that the maximum von Mises stress near IT using the SAF 6060 cushion is lower than the other two cushions by about 30~37% at the same frequency of 20 Hz. Moreover, the SAF 6060 cushion shows lower stress within the buttock especially at the region near the cushion as shown in **Figure 6**. Therefore, the SAF 6060 cushion is effective in reducing the stress below IT, and also has better pressure distributions at three distinct locations than the other two.

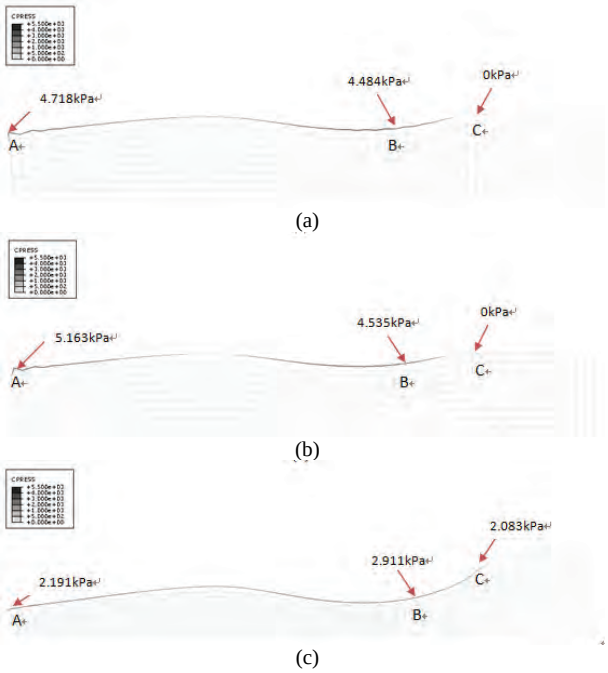

Figure 4. Maximum contact pressure at the three different locations of the three cushions at the frequency of 20 Hz. (a) Elastic 15000; (b) Elastic 20000 and (c) SAF 6060.

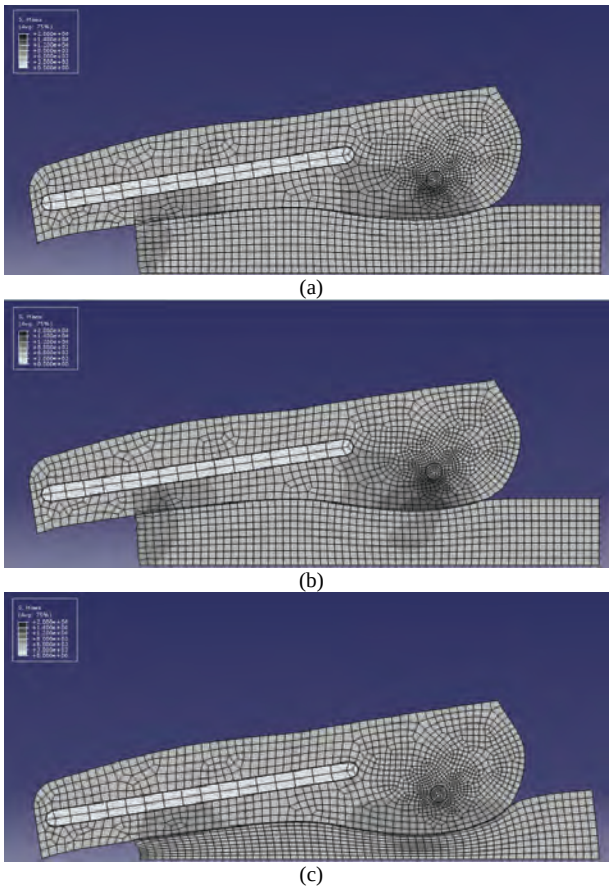

(a)

(b)

(c)

Figure 5. von Mises stresses distribution within the human body and cushion at the frequency of 20 Hz. (a) Elastic 15000; (b) Elastic 20000 and (c) SAF 6060.

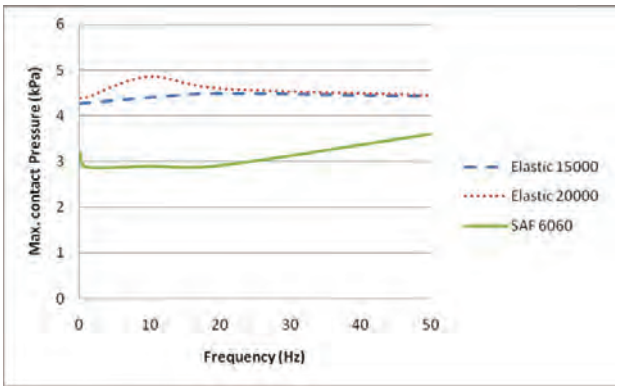

Figure 6. Maximum contact pressure versus frequency.

For a range of frequencies under study, the magnitude of maximum contact pressure in the SAF 6060 cushion is much lower than that of the other two cushions as shown in **Figure 6**. **Figure 7** shows the variation of maximum contact pressure with time for the three different cushions in response to five different frequencies. In **Figure 7**, the contact pressure generally increases rapidly to reach a maximum for all frequencies and cushions during the first step, because the buttock-thigh model fell quickly onto the cushion due to the gravity.

During the second step, all the three cushions were subjected to a vertical vibration of different frequencies. At the frequency of 0.1 Hz, the responses of all three cushions are slow and do not vary sinusoidally after 15 seconds as shown in **Figure 7(a)**. It can be observed from **Figure 7(a)** that the maximum contact pressure at the location B for the Elastic 15000 and Elastic 20000 cushions keep increasing with time while that for the SAF 6060 cushion increases with time up to 500 seconds. When the frequency is increased to 1 Hz, there is only a slight change in the maximum contact pressure around 0.02 to 0.04 kPa as shown in **Figure 7(b)**. When the frequency is increased to 10Hz or above, the responses of all the cushions become significant after 15 seconds. It is apparent from **Figures 7(c)** and **7(d)** that the amplitude of varying maximum contact pressure for the SAF 6060 cushion at the frequency of 10 Hz and 20 Hz is only around 0.15 kPa, which is much lower than those of the other two cushions by 63~85%. At the frequency of 50 Hz, the amplitude for the SAF 6060 cushion has sharply increased to 1.2 kPa, which is much higher than those of the other two cushions as shown in **Figure 7(e)**. Therefore, the SAF 6060 cushion is effective in reducing the amplitude of varying maximum contact pressure, especially for the frequency of 10-20 Hz, which belong to the frequency range of vibration generated mostly by vehicles and aircrafts.

For simplification and reducing the amount of CPU time for running the simulation, the 2D model of the buttock-thigh was firstly developed to study mechanical responses in bony prominence of IT and the vibration

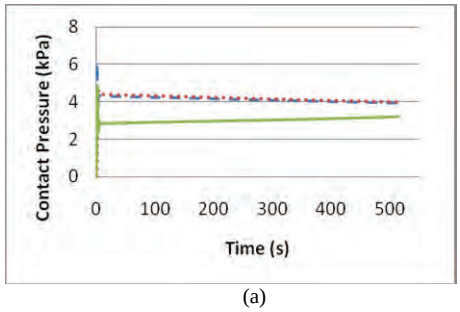

(a)

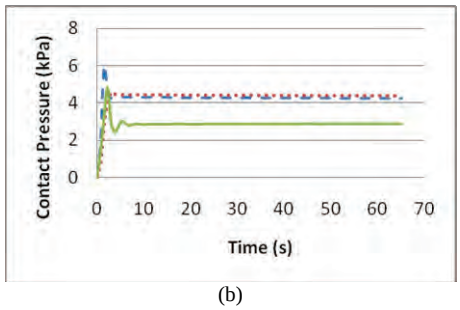

(b)

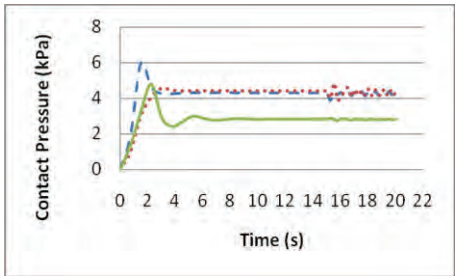

(c)

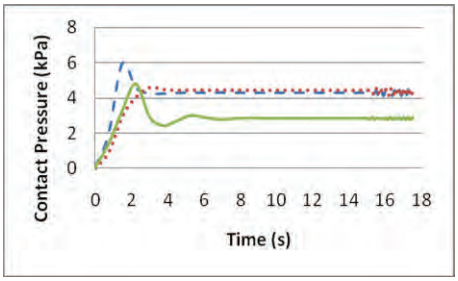

(d)

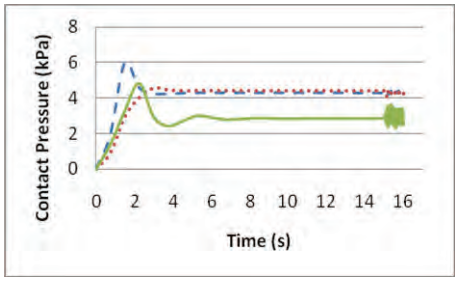

(e)

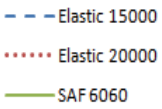

Figure 7. Variation of maximum contact pressure at location B with time at various frequencies. (a) 0.1 Hz; (b) 1 Hz; (c) 10 Hz; (d) 20 Hz and (e) 50 Hz.

transmissibility of different cushions under vertical vibration at different frequencies. As 3D finite element model has the advantages of an accurate anatomical geometry and accuracy in performance, a 3D model representing more complicated geometry may be developed in future work.

4. Conclusions

This simplified simulation was designed to mimic the response of the human under the vertical vibration. Finite element analysis could evaluate the transmission of vibrations onto different seat cushions subjected to varying frequencies. From this analysis, the SAF 6060 seat cushion was found to be effective in reducing the amplitude of varying maximum contact pressure, especially for the frequency of 10-20 Hz, belonging to the frequency range of vibration generated mostly by vehicles and aircraft. Thus, this method is useful for designing the material properties and the shape of the seat cushion for reducing the transmission of vibrations to users at a certain frequency range.

5. Acknowledgements

The authors would like to thank the Research Grants Council of the Hong Kong Special Administrative Region for its support of the project (PolyU 5273/07E).

6. References

[1] M. M. Verver, J. van Hoof, C. W. J. Oomens, J. S. H. M. Wismans and F. P. T. Baaijens, "A Finite Element Model of the Human Buttocks for Prediction of Seat Pressure Distributions," *Computer Methods in Biomechanics and Biomedical Engineering*, Vol. 7, No. 4, 2004, pp. 193-203.

[2] D. M. Brienza, P. E. Karg, M. J. Geyer, S. Kelsey and E. Trefler, "The Relationship between Pressure Ulcer Incidence and Buttock-Seat Cushion Interface Pressure in At-Risk Elderly Wheelchair Users," *Archives of Physical Medicine and Rehabilitation*, Vol. 82, No. 4, 2002, pp. 529-533.

[3] J. M. Black, "Moving toward Consensus on Deep Tissue Injury and Pressure Ulcer Staging," *Advances in Skin & Wound Care*: *The Journal for Prevention and Healing*," Vol. 18, No. 8, 2005, pp. 415-421.

[4] M. R. Bliss, "Acute Pressure Area Care: Sir James Paget's Legacy," *Lancet*, Vol. 339, No. 8792, 1992, pp. 221-223.

[5] M. Grujicic, B. Pandurangan, G. Arakere, W. C. Bell, T. He and X. Xie, "Seat-Cushion and Soft-Tissue Material Modeling and a Finite Element Investigation of the Seating Comfort for Passenger-Vehicle Occupants," *Materials & Design*, Vol. 30, No. 10, 2009, pp. 4273-4285.

[6] E. Linder-Ganz, N. Shabshin, Y. Itzchak, Z. Yizhar, I. Siev-Ner and A. Gefen, "Strains and Stresses in Sub-Dermal Tissues of the Buttocks are Greater in Paraplegics than in Healthy During Sitting," *Journal of Biomechanics*, Vol. 41, No. 3, 2008, pp. 567-580.

[7] M. Makhsous, D. Lim, R. Hendrix, J. Bankard, W. Z. Rymer and L. Fang, "Finite Element Analysis for Evaluation of Pressure Ulcer on the Buttock: Development and Vvalidation," *IEEE Transactions on Neural Systems and Rehabilitation Engineering*, Vol. 15, No. 4, 2007, pp. 517-525.

[8] R. Ragan, T. W. Kernozek, M. Bidar and J. W. Matheson, "Seat-Interface Pressures on Various Thicknesses of Foam Wheelchair Cushions: A Finite Modeling Approach," *Archives of Physical Medicine and Rehabilitation*, Vol. 83, No. 6, 2002, pp. 872-875.

[9] A. Siefert, S. Pankoke and H. P. Wölfel, "Virtual Optimisation of Car Passenger Seats: Simulation of Static and

Dynamic Effects on Drivers' Seating Comfort," *International Journal of Industrial Ergonomics*, Vol. 38, No. 5-6, 2008, pp. 410-424.

[10] Q. Sun, F. Lin, L. Ruberte, E. Nam, R. Hendrix and M. Makhsous, "FE Modeling and Analysis of Compressed Human Buttock-Thigh Tissue," *Proceeding of ASB* 29*th Annual Meeting*, Georgia, 2005.

[11] B. A. Todd and J. G. Thacker, "Three-Dimensional Computer Model of the Human Buttocks, In Vivo," *Journal of Rehabilitation Research*, Vol. 31, No. 2, 1984, pp. 111-118.

[12] E. Wagnac, C. Aubin and J. Dansereau, "A New Method to Generate a Patient-Specific Finite Element Model of the Human Buttocks," *IEEE transactions on Biomedical Engineering*, Vol. 55, No. 2, 2008, pp. 774-782.

[13] R. A. Cooper, "Wheelchair Selection and Configuration," *Demos Medical*, New York, 1998.

[14] J. L. Minkel, "Seating and Mobility Considerations for People with Spinal Cord Injury," *Physical Therapy*, Vol. 80, No. 7, 2000, pp. 701-709.

[15] X. Wu, S. Rakheja and P. É. Boileau, "Distribution of Human-Seat Interface Pressure on a Soft Automotive Seat under Vertical Vibration," *International Journal of Industrial Ergonomics*, Vol. 24, No. 5, 1999, pp. 545-557.

[16] C. P. DiGiovine, R. A. Cooper, S. G. Fitzgerald, M. L. Boninger, E. J. Wolf and S. Guo, "Whole-Body Vibration During Manual Wheelchair Propulsion with Selected Seat Cushions and Back Supports," *IEEE Transactions* on *Neural Systems and Rehabilitation Engineering*, Vol. 11, No. 3, 2003, pp. 311-322.

[17] International Organization for Standardization, "ISO 2631-1: 1997, Mechanical Vibration and Shock - Evaluation of Human Exposure to Whole-Body Vibration," Switzerland, 1997.

[18] M. M. Verver, J. van Hoof, C. W. J. Oomens, N. van de Wouw and J. S. H. M. Wismans, "Estimation of Spinal Loading in Vertical Vibrations by Numerical Simulation," *Clinical Biomechanics*, Vol. 18, No. 9, 2003, pp. 800-811.

[19] S. Kitazaki and M. J. Griffin, "A Modal Analysis of Whole-Body Vertical Vibration Using a Finite Element Model of the Human Body," *Journal of Sound and Vibration*, Vol. 200, No. 1, 1997, pp. 83-103.

[20] T.-H. Kim, Y.-T. Kim and Y.-S. Yoon, "Development of a Biomechanical Model of the Human Body in a Sitting Posture with Vibration Transmissibility in the Vertical Direction," *International Journal of Industrial Ergonomics*, Vol. 35, No. 9, 2005, pp. 817-829.

[21] J. Rosen and M. Arcan, "Modeling the Human Body/Seat System in a Vibration Environment," *Journal of Biomechanical Engineering*, Vol. 125, No. 2, 2003, pp. 223-231.

[22] F. M. L. Amirouche, "Modeling of Human Reactions to Whole-body Vibration," *Journal of Biomechanical Engineering*, Vol. 109, No. 3, 1987, pp. 210-217.

[23] D. R. Huston, C. C. Johnson, M. A. Wood and X. Zhao, "Vibration Attenuating Characteristics of Air Filled Seat Cushions," *Journal of Sound and Vibration*, Vol. 222, No. 2, 1999, pp. 333-340.

[24] E. J. Wolf, M. S. R. A. Cooper, C. P. DiGiovine, M. L. Boninger and S. Guo, "Using the Absorbed Power Method to Evaluate Effectiveness of Vibration Absorption of Selected Seat Cushions During Manual Wheelchair Propulsion," *Medical Engineering & Physics*, Vol. 26, No. 9, 2004, pp. 799-806.

[25] R. L. Huston, "Principles of Biomechanics," CRC Press, Boca Raton, 2009.

[26] W. Chow and E. Odell, "Deformations and Stresses in Soft Body Tissues of a Sitting Person," *Journal of Biomechanical Engineering*, Vol. 100, No. 2, 1978, pp. 79-87.

[27] A. Lowe and R. S. Lakes, "Negative Poisson's Ratio Foam as Seat Cushion Material," *Cellular Polymers*, Vol. 19, No. 3, 2000, pp. 157-167.

[28] ABAQUS Version 6.9-1, "User Documentation," Dassault Systems, 2009.

[29] M. Schrodt, G. Benderoth and A. Kuhhorn, "Hyperelastic Description of Polymer Soft Foams at Finite Deformations," *Technische Mechanik*, Vol. 25, No. 3-4, 2005, pp. 162-173.

[30] E. Pennestrì, P. P. Valentini and L. Vita, "Comfort Analysis of Car Occupants: Comparison between Multibody and Finite Element Models," *International Journal of Vehicle Systems Modelling and Testing*, Vol. 1, No. 1-3, 2005, pp. 68-78.

[31] C. Y. Tang and C. P. Tsui, "Method of Modeling Muscular Tissue with Active Finite Elements," U. S. Patent, The Hong Kong Polytechnic University, Kowloon (HK), 2006.

[32] D. B. Chaffin, G. B. J. Andersson and B. J. Martin, "Occupational Biomechanics," Wiley-Interscience, Hoboken, 2006.

Engineering, 2010, 2, 727-732
doi:10.4236/eng.2010.29094 Published Online September 2010 (http://www.SciRP.org/journal/eng)

Rolling Deformations and Residual Stresses of Large Circular Saw Body

Bolesław Porankiewicz[1], Jari Parantainen[2], Karolina Ostrowska[3]
[1]*University of Zielona Góra, Zielona Góra, Poland*
[2]*Stresstech OY, Vaajakoski, Finland*
[3]*Poznań University of Technology, Poznań, Poland*
E-mail: *poranek@amu.edu.pl, jari.parantainen@stresstech.fi, karolina.ostra@gmail.com*
Received May 21, 2010; *revised July* 19, 2010; *accepted September* 5, 2010

Abstract

Rolling path squeezes and rolling residual stresses of large diameter circular saw body for wood, generated by rolling pressure from 10 up to 120 bar were examined. X-ray diffraction, Barkhausen noise (*BN*) and Full Width of the peak at a Half Maximum (*FWHM*) (^{o}) methods for evaluation of residual stresses were used. Dependencies of a tangential rolling residual stresses inside rolling paths upon rolling pressure *p* (bar) and rolling area *A* (mm^2) were evaluated. The rolling pressure, as large as 60 bar, resulting in the rolling squeeze as high as 0.04 mm^2, and, tangential residual compression stresses inside a rolling path, as large as σ_{TI} = −822 MPa, was considered to be the largest for the practical application.

Keywords: Circular Saw, Rolling Squeeze Area, Rolling Squeeze Width, Rolling Squeeze Depth, Rolling Pressure, Tangential Rolling Residual Stresses, Radial Rolling Residual Stresses, X-Ray Diffraction, Barkhausen Noise, FWHM.

1. Introduction

Circular saws rolling use to be widely applied method of initial tensioning, aiming at increase the dynamic stiffness of saws for wood and secondary wood products machining. This method is not devoid of negative aspects. It has to be mentioned that the rolling may cause necessity to correct flatness when stresses distribution inside a circular saw body is not correct. There are several ways of evaluation of rolling effects, like: - a depth *d* (mm), - an area *A* (mm^2) of a rolling path, - a light gap between deformed blade and a straight edge rule [1], - a static stiffness [2], - a compression stresses inside a rolling path. However, as a final measure of effect of a saw blade rolling was recognized as a shift of natural frequencies and critical rotational speeds of several initial vibration modes [3,4]. From available literature important facts concerning with amount of tensioning necessary to insert in a saw blades of different dimension and for different applications in order to get stable work are known [5-7]. However, from practical point of view there are lack of informations in published works, about rolling pressures used, plastic squeeze of circular saw body material and rolling path shape [2]. The goals of actual work were: to exam the amount of squeeze in a circular saw body using different rolling pressures *p* (bar) and measure presence of residual stresses using three different techniques.

2. Experimental

The circular saw body, before cemented carbide tips soldering, by thickness of t_S = 3 mm and by diameter of *D* = 620 mm, made of 75Cr1 low alloy steel, was rolled in industrial conditions, with use of rolling machine Arga T08 on 12 different paths. The pressure *p* (bar) in hydraulic cylinder, was from 10 bar (145.04 psi) up to 120 bar (1740.456 psi) with of 10 bar (145.04 psi) increment. The depth *d* (mm) and width *w* (mm) of a rolling paths were measured with use of profilografometer type ME10. X-ray residual stress measurements contained totally 25 points from the blade using modified d(sin$^2\psi$) [8] method. X-ray measurements were performed using XSTRESS3000 diffractometer manufactured by Stresstech OY, by following conditions:

Device: G2R (#7147)
Radiation source: CrKa
Diffraction line angular position,

according to Bragg's law 2q: 156.4° (211)
Spot size: 1 mm and 2 mm
Exposure time: 20 s and 8 s
Tilt angles: 4/4 tilts, ψ <−40°/40°>; ψ oscillation ±5°
Young's modulus: 211 000 MPa
Poisson ratio: 0.3
Calculation: Cross correlation, constant background [8].
Measurement method: Modified $d(\sin^2\psi)$ [8]

The measurement directions can be seen in **Figure 1**. The angle of φ = 0° corresponds to tangential direction and of φ = 90° to radial direction.

The *FWHM* (°) values were calculated from the x-ray diffraction peaks in order to get indirect information for the presence of the residual stresses through micro hardness and plastic deformation (dislocation density) layer. The *FWHM* (°) values are average ones from ψ (°) angles examined.

The *BN* measurements were performed in the same radial path, like during the X-ray diffraction ones, using following conditions:

Device: Rollscan 300
Sensor: S1-138
Magnetizing voltage: 4.0 Vpp
Magnetizing frequency: 100 Hz
Analyzing frequency: 70-200 kHz

Higher hardness and/or compressive stresses decrease the *BN* and vice versa [9]. It has to be mentioned that using the *BN* itself was not possible to evaluate absolute values of residual stresses.

Outside rolling paths Rockwell hardness was measured (according to PN-EN ISO 6508 standard) with preliminary load of 98 N and total load of 1471 N, in places shown in **Figure 2**, by 5 repetitions. For every place outside rolling paths an average value and standard deviation were calculated.

3. Results and Discussion

The rolling squeeze cross section shape for the largest rolling pressure, shown in **Figure 3**, was approximated with use of a second order polynomial function $d = f(a_1 + a_2 \cdot w_i + a_3 \cdot w_i^2)$. It was evaluated by a Formula (1) with correlation coefficient R and standard deviation S_D(mm), as large as 0.91 and 0.0067 mm respectively.

$$d = 0.010209 - 0.037531 \cdot w_i + 0.00709 \cdot w_i^2 \text{ (mm)} \quad (1)$$

In the rolling squeeze cross section shape, several up-casts can be seen, what indicated possible wear of rolls and/or bearings in the rolling machine. The depth and width of the largest up-cast were as large as 11.4 μm and 590 μm respectively. Results of measurements of rolling squeeze depth d (mm) and width w (mm) were collected in **Table 1** and illustrated in **Figure 4** and **Figure 5**, re-spectively.

From **Figure 4** it can be seen that rolling squeeze depth d (mm) increased with growth of the rolling pressure p (bar) with rather large dispersion. The width w (mm) of the rolling squeezes, shown in **Figure 5** increased with a growth of the rolling pressure p (bar) until 50 bar. For larger pressure opposite tendency can be noticed with large dispersion. The area of the rolling squeeze A (mm^2), shown in **Figure 6** was evaluated by integrating the surface limited from the bottom by the squeeze shape and from the top by d = 0. Large dispersion in the dependency $A = f(p)$ can also be seen especially for rolling pressure larger than p = 60 bar, namely p = 70 bar, 100 bar and 110 bar. The reason of large dispersion of rolling depth d (mm), rolling width w (mm) and rolling squeeze A (mm^2) was probably the wear of rolls or bearings in the rolling machine used. According to the work [6], the rolling squeeze area of 0.04 mm^2, applied for a circular saw diameter D = 400 mm, saw blade thickness t_S = 2 mm and collar diameter of d_C = 100 mm, resulted in 2.4, 29.4 and 14.5 times increased

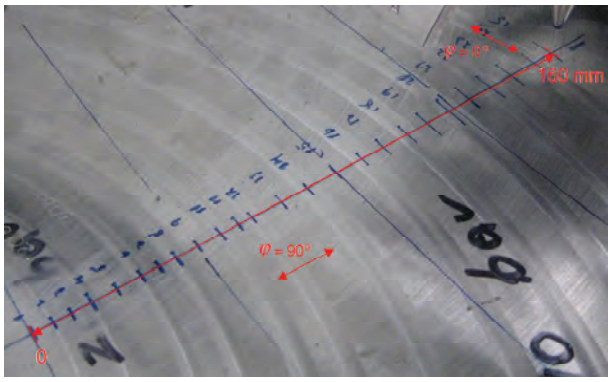

Figure 1. Direction of X-ray diffraction measurements.

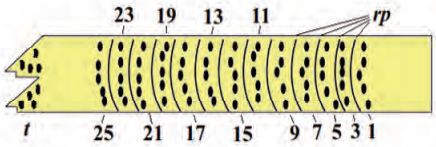

Figure 2. Places for Rockwell hardness measurements: - outside rolling paths nos. 1-25, *t* - tooth area, *rp* - rolling paths.

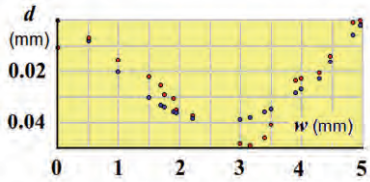

Figure 3. The observed (red) and predicted (blue) shape of cross section of the rolling path for maximum rolling pressure *p* = 120 bar.

Table 1. Rolling pressure *p* (bar), rolling depth *d* (mm), rolling width *w*(mm), rolling area *A* (mm^2).

p	*d*	*w*	*A*
(MPa)	(mm)	(mm)	(mm^2)
10	2.02	3.24	0.0027
20	1	3.95	0.0015
30	3.4	3.9	0.0075
40	5.6	5.48	0.0176
50	9.3	6.33	0.029
60	15.3	6.11	0.0443
70	9.1	5.03	0.0318
80	23.2	4.21	0.0463
90	21.6	5.59	0.0642
100	18.8	4.99	0.0312
110	17.7	4.69	0.0312
120	49	4.95	0.123

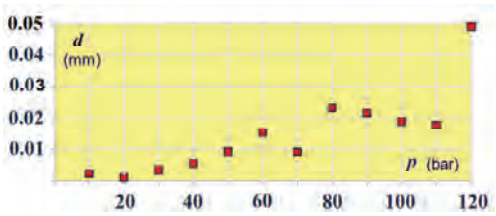

Figure 4. The average rolling path depth *d* (mm) in dependence from rolling pressure *p* (bar).

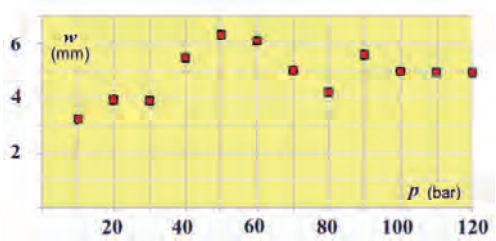

Figure 5. The average rolling path width *w* (mm) in dependence from rolling pressure *p* (bar).

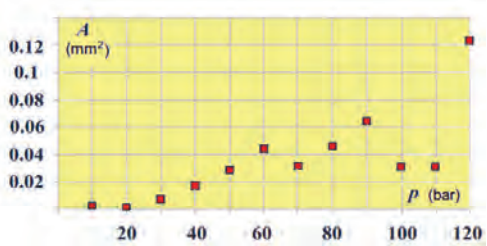

Figure 6. The average rolling path area *A* (mm^2) in dependence from rolling pressure *p* (bar).

natural frequencies of (0,4), (0,3) and (0,2) vibration modes respectively, while the vibration modes (0,1) and (0,0) natural frequencies were dropped down as much as 18% and 23% respectively by rotating speed of 3600 min^{-1} (the first digit in the brackets '0' is the number of nodal circles, the second digit '4', '3' and '2' is the number of nodal diameters). However, in the work quoted above, no information on used rolling pressure and rolling squeeze cross section profile were given.

The residual stresses evaluated with use of the X-ray XSTRESS3000 diffractometer, inside and outside rolling paths, in both tangential σ_{TI} (MPa) and radial directions σ_{RI} (MPa) were shown in **Figure 7**. From **Figure 7** it can be seen that tangential residual stresses inside rolling path σ_{TI} (MPa) did not change their values smoothly according to an enlargement of the rolling pressure *p* (bar), what was clearly seen for points nos.: 4, 8, 16 and 22. The dispersion can also be seen for tangential residual stresses outside rolling path σ_{TI} (MPa) (points nos. 5, 11, 12, 17 and 21). The reason of that might be a rather large dispersion of the residual stresses in the saw blade before rolling and/or large dispersion of rolling squeeze profile. A saw in which body are present such a large, and highly differentiated residual stresses generated during manufacturing process, has small chance for a smooth and effective work in future even if using hammering will be exactly flattened.

From **Figure 7** it can be seen decreasing tendency of the tangential residual stresses outside rolling paths σ_{TO} (MPa), with an increase of the rolling pressure *p* (bar). Starting from point no. 11 up to point no. 25, the tangential residual stresses outside rolling paths σ_{TO} (MPa) did change from compression to tensile. This was due to the total influence of rolling effect on tangential residual stresses $\Delta\sigma_T$ (MPa) along saw body radius. It was also assumed that in the saw blade examined before rolling, there were average tangential residual stresses distribution σ_{TO} (MPa) with randomly distributed dispersion. The average total rolling effect, as a function of distance $\Delta\sigma_T = f(L)$ was approximated with statistical Formula (2) by correlation coefficient *R* and standard deviation S_D (MPa) as large as 0.85 and 43.6 MPa, respectively.

$$\Delta\sigma_T = -79.861196 + 3.278002 \cdot L - 0.0141832 \cdot L^2 \text{ (MPa)} \quad (2)$$

The tangential compression stresses inside rolling paths after correction σ_{TIK} (MPa) were calculated as difference between the tangential compression stresses inside rolling paths σ_{TI} (MPa) and the average rolling effect on the tangential residual stresses outside rolling paths $\Delta\sigma_T$ (MPa), described by Formula (2), and approximated by statistical Formula (3) in dependence upon rolling pressure *p* (bar), by $R = 0.96$, $S_D = 40.8$ MPa and upon rolling squeeze area *A* (mm^2) by statistical Formula (4), by $R = 0.89$ and $SD = 68.7$ MPa.

$$\sigma_{TIK} = 161639.174 - 161769.431 \cdot p^{0.001152} \text{ (MPa)} \quad (3)$$

$$\sigma_{TIK} = 54277.706 - 55542.535 \cdot A^{0.00184} \text{ (MPa)} \quad (4)$$

It has to be mentioned that the dispersion of the residual tangential residual stresses in the examined saw blade

before rolling (outside rolling paths σ_{TO} (MPa)) overshadowed examined relation.

Looking at **Figure 8** it can be concluded that an increase of rolling pressure above $p > 70$ bar stops the increase in tangential compression stresses inside rolling path. One can conclude that in analyzed case, the maximum rolling squeeze, giving increase tangential compression stresses inside rolling path was $A = 0.04$ mm^2. In the published papers [1,2,5-7], there was no information about dispersion of residual stresses inside saw blades before rolling.

In examined case, after correction, the tensile stress inside saw blade before rolling, at point no. 5 was evidenced, as large as +1.9 MPa (**Figure 8**). The compression stress in point no. 21 was also very low, as small as −5.7 MPa.

The radial residual stresses inside rolling paths σ_{RI} (MPa) were smaller (**Figure 7**). They oscillated on level of about <−332, −484> MPa. From **Figure 7** it can also be seen the presence of a residual radial tensile stresses σ_{RO} (MPa) for all points outside rolling paths. No significant correlation between residual radial tensile stresses outside rolling paths σ_{RO} (MPa) and distance L (mm) along saw body radius, according to increasing rolling pressure p(bar) was recognized. The residual radial stresses outside rolling paths σ_{RO} (MPa) did oscillate in the range of <+4, +266> MPa with an error of < 35, 46 > MPa.

It can be seen from **Figure 9** that the *BN* measurements followed general shape of stresses distribution showed in **Figure 7**, excluding total rolling effect $\Delta\sigma_T$ (MPa). The *BN* measurements allow recognizing places with large and small values of compression stresses. Places outside rolling paths shown in **Figure 9** on positions $L = 108$ mm, $L = 114$ mm, $L = 134$ mm, and $L = 144$ mm were having the largest of all the *BN* values, what effect was not seen in **Figure 7** and **Figure 8**. The reason of that was lower Rockwell hardness of the saw body material closer to the rim, what show **Figure 10**, for points nos. 17, 19, 21 and 25. According to **Figure 9**, the hardness in point no. 23 was too large, however, not the same measuring path for the *BN* and the Rockwell hardness as well as large dispersion of the saw body hardness resulted in such a difference. For places outside rolling paths on positions $L = 0$-4 mm and $L = 12$-18 mm, shown in **Figure 9**, low *BN* values can be associated with large saw body hardness. For places inside rolling paths, on positions $L = 6$ mm and $L = 22$ mm, shown in **Figure 9**, slightly higher the *BN* values, can be associated with small rolling residual compression stresses. The *BN* measurements results for places outside rolling paths shown in **Figure 9** were characterized with large dispersion. The *BN* measurements technique would be useful in manufacturing conditions, to control residual stresses distribution in saw blades after different operations. This conclusion can also be supported by the fact of many times lower price of the Rollscan 300 device in comparison to the X-ray XSTRESS3000 diffractometer. Still the priority benefit is in the time consumed in performing the measurements. The whole X-ray measurement procedure can easily last hour or two, but the *BN* measurement is usually done in few seconds.

Results of measurements of the *FWHM* (^{o}) outside and inside rolling, were collected in **Table 2** and illustrated in **Figure 11**. From the plot shown in **Figure 11** it can be

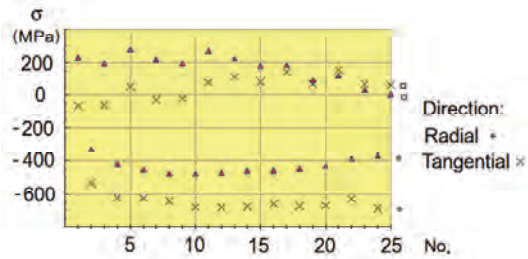

Figure 7. The plot of residual stresses σ (MPa) along saw blade radius, in tangential and radial directions, * - inside and ¤ - outside rolling paths.

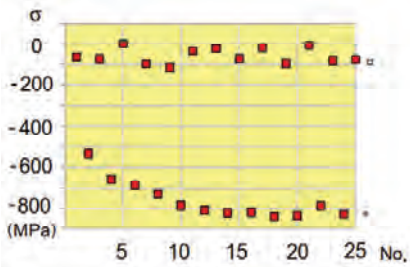

Figure 8. The plot of residual stresses in tangential direction after correction, along the saw blade radius, * - inside σ_{TI} (MPa), and ¤ - outside σ_{TO} (MPa) rolling paths.

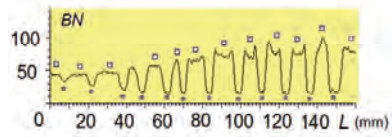

Figure 9. The plot of the Barkhausen noise along saw blade radius, * inside and ¤ outside rolling paths.

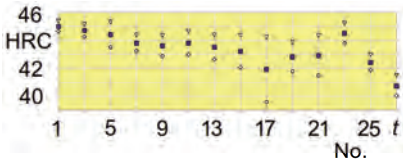

Figure 10. The plot of the Rockwell hardness of the saw-body, along saw blade radius, in points number No., outside rolling paths, *t* - tooth area.

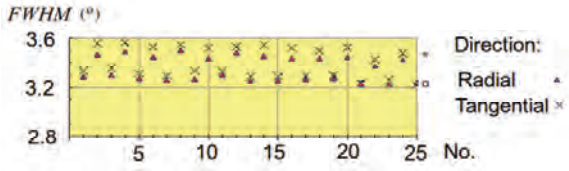

Figure 11. The plot of *FWHM* (°) along saw blade radius in tangential and radial directions, * - inside and ¤ - outside rolling paths.

seen that the *FWHM* (°) values were larger for places inside rolling paths than for places outside rolling paths, what was opposite in comparison to the *BN* measurements results shown in **Figure 9**. The difference between small and large residual compression stresses inside rolling paths can not be recognized using **Figure 11**, what indicates that the shape of the plots from **Figure 7** and **Figure 11** was not followed each other. The *FWHM* (°) measurements allow recognizing places with large and small residual stresses, but with much lower precision if compare to the *BN* measurements. The increase of the *FWMH* (°) values inside rolling paths might also be occurred by work hardening effect of the rolling process.

4. Conclusions

The experiment and measurements of rolling effects and analysis of results obtained allow concluding that:

1) It is recommended to apply the rolling pressure up to 60MPa by use rolling machine Arga T08, giving rolling squeeze as large as A = 0.04 mm^2 and tangential residual compression stresses inside rolling paths as large as σ_{TI} = −822 MPa.

2) For rolling pressure p (bar) from 70 to 120 bar, no increase of the tangential compression residual stresses increase inside the rolling paths was observed.

3) For rolling pressure p (bar) from 70 to 120 bar large variation of rolling squeeze depth d (mm) and width w(mm) was seen. By the largest rolling pressure (d = 0.049 mm, w = 4.95 mm, A = 0.123 mm^2) significant upcast of 11.4 µm in depth and 590 µm in the width was evidenced, indicating possible wear of rolls and/or bearings in the rolling machine.

4) Large dispersion of tangential σ_{TO} (MPa) and radial σ_{RO} (MPa) residual stresses outside rolling paths, added to the saw blade before rolling, with maximum value of 155 MPa and 274 MPa respectively was evidenced.

5) The *BN* measurements allow recognizing the presence of small and large compression stresses inside and outside rolling paths, but this information is mixed with effect of hardness change distribution.

6) In one measuring point, outside rolling path after correction positive, residual tensile tangential stress of + 1.9 MPa was recognized.

Table 2. Stress and *FWHM* (°) values, evaluated with use of X-ray diffractometer.

Position No	Stress Tangential $\varphi = 0°$		Stress Radial $\varphi = 90°$		*FWHM* $\varphi = 0°$	*FWHM* $\varphi = 90°$
	(MPa)	(MPa)	(MPa)	(MP)	(°)	(°)
1	−64	10	225	46	3.33	3.28
2	−533	8	−332	13	3.56	3.46
3	−60	11	190	41	3.35	3.30
4	−625	7	−424	8	3.56	3.49
5	51	13	274	39	3.31	3.27
6	−626	8	−458	18	3.53	3.45
7	−26	11	215	42	3.29	3.25
8	−645	7	−484	15	3.55	3.50
9	−19	12	189	46	3.33	3.26
10	−681	10	−483	11	3.52	3.43
11	77	17	266	40	3.33	3.29
12	−683	10	−477	18	3.53	3.48
13	113	12	217	40	3.28	3.25
14	−678	6	−464	15	3.54	3.45
15	81	18	175	41	3.28	3.25
16	−660	17	−462	19	3.52	3.43
17	144	20	181	40	3.29	3.26
18	−674	9	−453	20	3.50	3.43
19	69	15	86	36	3.29	3.27
20	−671	9	−435	21	3.52	3.44
21	155	21	115	35	3.23	3.22
22	−631	11	−392	25	3.43	3.37
23	67	22	30	36	3.26	3.22
24	−687	11	−377	34	3.48	3.42
25	59	26	4	28	3.22	3.24

7) No significant rolling effect on radial residual stresses inside σ_{RI} (MPa) and outside σ_{RI} (MPa) rolling paths was seen.

5. Acknowledgements

The authors were grateful for the support of the Stresstech OY Company in performing X-ray diffraction and *BN* measurements. The authors were also grateful for the support of the Poznań Networking & Supercomputing Center (PCSS) calculation grant.

6. References

[1] P. F. Lister and G. S. Schajer, "The Effectiveness of the Light-Gap and Frequency Measurement Methods for Evaluating Saw Tensioning," *Proceedings of* 10*th Wood Machining Seminar*, University of California, Forest Products Laboratory, Richmond, 21-23 October 1991, pp. 68-84.

[2] R. Szymani and C. D. Mote, "Circular Saw Stiffness as a

Measure of Tension," *Forest Products Journal*, Vol. 27, No. 3, 1977, pp. 28-32.

[3] J. Rhemrev and L. Trinchera, "Improving the Stability of Thin Circular Saws though Applied Research," 32*nd Annual Meeting the Forest Products Research Society*, Atlanta, 1978.

[4] G. S. Schajer and C. D. Mote, "Analysis of Roll Tensioning and its Influence on Circular Saw Stability," *Wood Science & Technology*, Vol. 17, 1983, pp. 287-302.

[5] U. V. Münz, "Means of Testing and Designing Circular Saw Blades," *Proceedings of the* 13*th International Wood Machining Seminar*, Vancouver, 17-20 June 1997, pp. 105-116.

[6] G. S. Schajer and C. D. Mote, "Analysis of Optimal Roll Tensioning for Circular Saw Stability," *Proceedings of* 7*th Wood Machining Seminar*, University of California Forest Products Laboratory, Richmond, 18-20 October 1982, pp. 264-283.

[7] G. S. Schajer and C. D. Mote, "Analysis of Optimal Roll Tensioning for Circular Saw Stability," *Wood & Fiber Science*, Vol. 16, No. 3, 1984, pp. 323-338.

[8] P. S. Prevey, "X-Ray Diffraction Residual Stress Techniques, Metals Handbook," 10 *Metals Park*: *American Society for Metals*, 1986, pp. 380-392.

[9] R. L. Pasley, "Barkhausen Effect - An Indication of Stress," Southwest Research Institute, San Antonio, Texas, 1969.

Engineering, 2010, 2, 733-739
doi:10.4236/eng.2010.29095 Published Online September 2010 (http://www.SciRP.org/journal/eng)

A Non-Dimensional Consideration in Combustor Axial Stress Computations

Ebene Ufot[1,2], Barinaadaa Thaddeus Lebele-Alawa[1*], Ibiba Emmanuel Douglas[1], Kelvin D. H. Bob-Manuel[1]
[1]*Faculty of Engineering, Rivers State University of Science and Technology, Port Harcourt, Nigeria*
[2]*Department of Mechanical Engineering, University of Uyo, Uyo, Nigeria*
E-mail: *lebele-alawa.thaddeus@ust.edu.ng*
Received June 23, 2010; *revised August* 5, 2010; *accepted August* 5, 2010

Abstract

Thermal stresses in the combustor of gas-turbines are computed using non-dimensional parameters. Buckingham pi theorem was used to arrange the listed relevant parameters into non-dimensional groups. In testing the validity of the functional relation of the non-dimensional independent parameters, use is made of the prevailing temperatures of the combustor in operation. A computer program was used to enhance computations. The results showed an interesting way of influencing the axial stresses. To reduce stresses in gas-turbine combustors, a method of varying the independent parameter that is of radius ratio oriented and thickness dependent was adopted. This showed a reduction of the axial stresses to minimal levels using the parameters. Plots were made and a point of inflection that manifested itself in the presentation of the axial stress function was further investigated upon. It turned out to be a point of abnormal stress level and out-of-trend temperature profile. The use of non-dimensional consideration proved adequate in the computation of axial stresses. The results showed a 2 percent difference from existing values of stresses got from a transient thermal loading of a combustor.

Keywords: Thermal, Stresses, Combustor, Gas-Turbine

1. Introduction

Thermally induced axial stresses or shocks occur in materials when they are heated or cooled. It affects the operations of gas-turbines due to the large components subjected to stresses. Many structural elements of hollow cylinders subjected to rapid internal heating crack or deform due to thermally induced axial stresses produced in them. Tret'yachenko, *et al.* [1] carried out investigations on thermal stresses of hollow cylinders drum of unilateral internal heating. The main aim of their investigations was to obtain graphs that could be used to estimate the stress level in cylindrical structural elements. Kumar and Rajgopalan, [2] performed non-dimensional stress analysis on cylindrical objects. They obtained plots of non-dimensional tangential stress against non-dimensional length of cylinder. Their presentations showed the differences in the values of functions from various radial positions.

The analytical solution for computing the radial and circumferential stresses in a functionally graded material (FGM) thick cylindrical vessel under influence of internal pressure and temperature was presented by Abrinia *et al.* [3]. FGMs are fabricated by continuously changing the volume fraction of two basic materials (usually ceramics and metals) in one or more directions.

Nomenclature

Ax.Str.Funct	Axial stress function-σ_{zth}/E
C	Non-dimensional axial stress parameter for average temperature
C_1	Non-dimensional axial stress parameter as ratio of radius dependent
C_2	Non-dimensional axial stress parameter as ratio of temperature to average temperature
E	Young's modulus of elasticity
T	Temperature in Kelvin
T_i	Temperature of the bulk airstream of combustion products
T_m	Average temperature in combustor
T_{ma}	Maximum average temperature in combustor

T_{wa}	Combustor outer wall temperature
T_{wi}	Combustor internal wall temperature
T_{surr}	Temperature of the surroundings
r	Radial distance from centre of cylinder
r_a	Radius to outer wall
r_i	Radius to inner wall
Greek letters	
α	Coefficient of thermal expansion
σ	Axial stress
ν	Poisson's ratio
Suffixes	
r	radial stress
φ	tangential stress
zth	Thermal stress in axial (z) direction

In the analysis, the effect of non-homogeneity in FGM thick cylinder could be implemented by choosing a dimensionless parameter, β, which could be assigned an arbitrary value affecting the stresses in the cylinder. Various values of β were used to demonstrate the effect of in-homogeneity on the stress distribution. They concluded that by changing the values of β, the properties of FGM could be so modified that the lowest stress levels were reached.

Kubo *et al.* [4] investigated a multidisciplinary problem of heat conduction, elastic deformation, heat transfer, liquid flow. They used inverse method for determining the optimum thermal load history which reduced transient thermal stress. Temperature history functions were introduced to ensure the continuity of the temperature increasing rate. The multidisciplinary complex problem was decomposed into heat transfer and thermal stress problems. Ootoa *et al.* [5] determined the temperature and thermal stress distribution in the cross-section of a non-homogenous hollow circular cylinder due to a moving heat source in the axial direction, and found that; the maximum temperature occurs at the region through which the moving heat source passed. All of the above used non-dimensional functions of stress and found that it very conveniently influenced the stresses so computed. Principal axes that could be considered in thermal stresses in hollow cylinders are axial, radial and the tangential. In this work only axial stresses will be considered. A non-dimensional approach of expression of the pertinent parameters has been adopted. This makes the expressions more compact and allows a wider understanding of the properties in further considerations. Dimensional analysis using the Buckingham π theorem has been applied in analyzing the stress problems. This therefore presents the axial stresses in few independent non-dimensional parameters. Thus it has enhanced the establishment of influencing factors to reduce stresses in materials. The involvement of a computer code has enabled fast computation of the axial stresses.

2. Materials and Methods

From the equation of thermally induced axial stress [6] one can re-work it to the required expression

$$\text{Axial Stress, } \sigma_{zth} = \nu(\sigma_{rth} + \sigma_{\varphi th}) - E\alpha_{th}T(r) \quad (1)$$

where σ_{rth} and $\sigma_{\varphi th}$ are given as:

Radial Stress,

$$\sigma_{rth} = \frac{E\alpha_{th}}{1-\nu}\left[\frac{r^2 - r_i^2}{r_a^2 - r_i^2}\frac{r_a^2}{r^2}T_m(ra) - T_m(r)\right] \quad (2)$$

Tangential Stress,

$$\sigma_{\phi th} = \frac{E\alpha_{th}}{1-\nu}\left[\left[\frac{r^2 + r^{i2}}{r_a^2 - r^{i2}}\right]\frac{r_a^2}{r^2}T_m(ra) + T_m(r) - T(r)\right] \quad (3)$$

Turning Axial Stress Equation to a Non-Dimensional Equation:

From Equation (1) above,

$$\sigma_{zth} = \nu(\sigma_r + \sigma_\phi) - E\alpha_{th}\ T(r)$$

$$\sigma_{zth} = \upsilon * \frac{E\alpha_{th}}{1-\upsilon}\left[\frac{r^2 - r_1^2}{r_a^2 - r_1^2} * \left[\frac{r_a}{r}\right]^2 * T_{ma} - T_m(r) + \frac{r^2 + r_i^2}{r_a^2 - r_i^2} + \left[\frac{ra}{r}\right]^2 * T_{ma} + T_{m(r)} - T_{(r)}\right] - Ea_{th}\ T_m$$

$$= \frac{\upsilon E\alpha_{th}}{1-\upsilon}\left[\frac{r2 - r_i^2}{r_a^2 - r_i^2} * \left[\frac{r_a}{\tau}\right]^2 * T_{ma} + \frac{r + r_i^2}{r_a^2 - r_i^2} * \left[\frac{ra}{r}\right] * T_{ma} - T_{(r)}\right] - E\alpha_{th}\ T_{(r)}$$

$$= \frac{\upsilon E\alpha_{th}}{1-\upsilon}\left[\frac{1}{r_a^2 - r_i^2} * \frac{r_a^2}{r^2} + T_{ma} * 2r^2 - T_{(r)}\right] - E\alpha_{th}\ T_{(r)}$$

$$= \frac{\upsilon E\alpha_{th}}{1-\upsilon}\left[\frac{1}{r_a^2 - r_i^2} * \left[\frac{ra}{r}\right]^2 * T_{ma}\ x\,(r^2 - r_i^2 + r^2 + r_i^2) - T_{(r)}\right] - E\alpha_{th}\ T_{(r)}$$

$$= \frac{2\upsilon E\alpha_{th}}{1-\upsilon}\frac{T_{ma}}{\left[1-\left(\frac{ri}{ra}\right)^2\right]} - \frac{E\alpha_{th}}{1-\upsilon}\ T_{(r)}$$

$$\sigma_{zth} = \frac{E\alpha_{th}}{1-\upsilon} * T_{ma}\left(\frac{2\upsilon}{1-\left(\frac{ri}{ra}\right)^2} - \frac{T_{(r)}}{T_{ma}}\right) \quad (4)$$

Hence, from Equation (2) above, some functional relation must exist in the form of

$$\sigma_{Zth} = \sigma_{Zth}\left(E,\ \alpha_{th},\ r_a,\ r_i,\ T_{ma},\ T_{(r)}\right) \quad (5)$$

Dimensionless Consideration on Axial Stress.

Sorting out the inherent parameters:

Forming a table of parameters: **Table 1**.

The Buckingham π theorem proves that in a physical problem including **n** quantities in which there are **m** dimensions, the quantities can be arranged into **n – m** independent dimensionless parameters.

Hence some functional relation must exist in the form as expressed in Equation (5)

$$\sigma_{zth} = \sigma_{zth}\left(E,\ \alpha_{th}\ r_a,\ r_i,\ T_{ma},\ T_{(r)}\right)$$

Applying the Buckingham π theorem, there are three π groups to be found, so Axial Stress, $\sigma_{Z\text{-}th}$ can be more compactly stated as a function of these three non-dimensional parameters [7]. Thus from Equation (5)

1. $\frac{\sigma_Z}{E}$ – *as a non – dimensional parameter* (**Axial Stress Function**)
2. $\frac{T_{(r)}}{T_{ma}}$ – *as* C_2
3. $\frac{2\upsilon}{1-\left(\frac{r_i}{r_a}\right)^2}$ *as* C_1
4. $T_{ma} * \alpha_{th}/(1-\upsilon)$ *as* C_0

Actually, the main three independent dimensionless parameters can be seen as:

$$\sigma_Z/E,\ C_0 * C_1 \ \ and \ \ C_0 * C_2$$

But Equation (3) can be written as:

$$\frac{\sigma_{Zth}}{E} = C_0\left[C_1\ (r) - C_2\ (r)\right] \quad (6)$$

3. Results and Discussions

The results of the non-dimensional axial stress computations are shown as program results below, and the corresponding wall thickness values are given in **Table 2**. The non-dimensional consideration gave a wider view of the axial stress. In **Figure 1** and **Figure 2**, the values were plotted against a non-dimensional temperature parameter,

EU402-AXIAL STRESS FUNCTION_PROGRAM RESULTS

VarNr,	ra,	Twa,	Twi
1	38	2549.6	2584.1

T(0),	T(1),	T(2),	T(3),	T(4)
2549.6	2558.2	2566.9	2575.5	2584.1

Tm(0),	Tm(1),	Tm(2),	Tm(3),	Tm(4)
194.8	176.5	130.2	80.7	27.8

VarNr	C1	C2	C0	AxialStress	AxialStressFunct:Ax-Str/E
1	3.96	13.09	0	.00	.000000
1	3.96	13.09	0.00345	−6618.35	−.031516
1	3.96	13.14	0	.00	.000000
1	3.96	13.14	0.00345	−6650.44	−.031669
1	3.96	13.18	0	.00	.000000
1	3.96	13.18	0.00345	−6682.52	−.031822
1	3.96	13.22	0	.00	.000000
1	3.96	13.22	0.00345	−6714.61	−.031974
1	3.96	13.27	0	.00	.000000
1	3.96	13.27	0.00345	−6746.69	−.032127

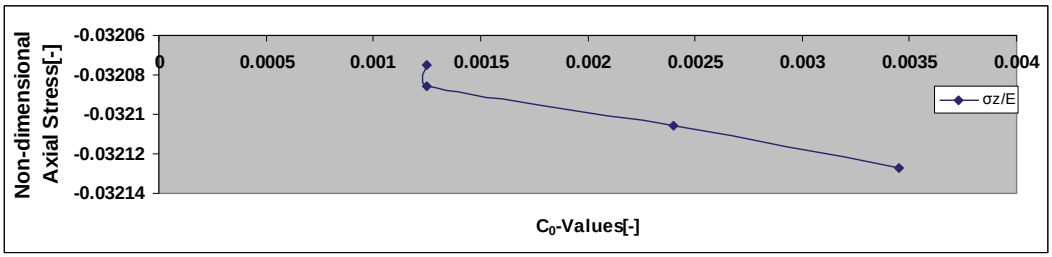

Figure 1. Non-dimensional axial stress versus C0-values.

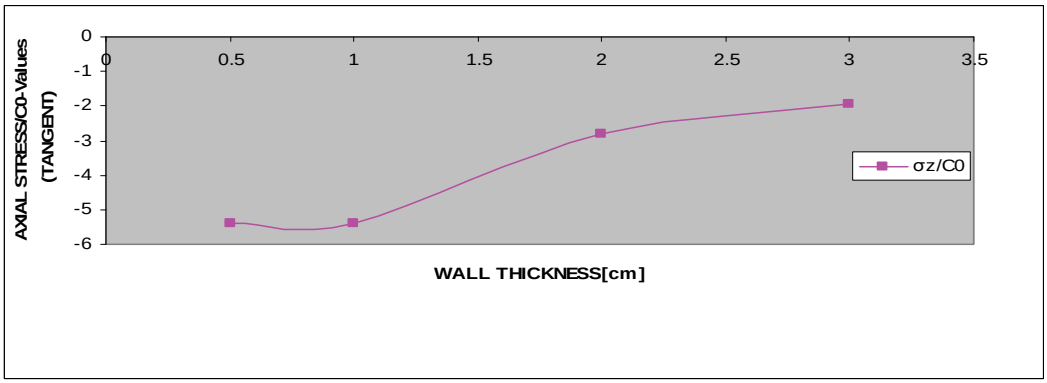

Figure 2. Axial stress/C0 (Tangent) versus wall thickness showing a point of inflection at a thickness of 1.44 cm.

Table 1. Dimensions of independent parameters for axial stress.

S/N	Input parameters		Dimensions			
1	Axial stress, σ_{th}	$\left(N/m^2 = 1kg\, m/s^2 * 1/m^2 \right)$	M	L^{-1}	T^{-2}	
2	E,	$\left(N/m^2 = 1kg/s^2 * m \right)$	M	L^{-1}	T^{-2}	
3	α_{th}	$\left(1/K \right)$				K^{-1}
4	T_{ma}	$[K]$				K
5	$T_{(r)}$	$[K]$				K
6	r_a	$[m]$		L		
7	r_i	$[m]$		L		
	$n - m = 3$					

Table 2. Axial stress function versus wall thickness.

Var.Nr	r_a	r_i	Wall Thickness	T_{surr}	T_i	T_{wa}	T_{wi}	Ax.Str.Fct. σ_{zth}(max)
1	38	35	3	620	2620	2549.6	2584.1	−0.032127
5	37	35	2	620	2620	2561.9	2584.7	−0.032106
7	36	35	1	620	2620	2574.0	2585.4	−0.032086
10	35.5	35	0.5	620	2620	2580.0	2585.7	−0.032075
18	35.25	35	0.25	620	2620	2586.0	2586.5	−0.032073
16 (AFAM)	75	74.5	0.25	605	2578	2535.5	2536.0	−0.031447

C_O and against the wall thickness, respectively. In **Figure 3** the axial stress function is plotted against the radial nodal positions. All the presentations show an increasing tendency with increased wall thickness.

The **Figure 4** above shows a method of influencing the stress levels in materials:

By increasing the independent parameter, C_1, the stress levels can be reduced

where
$$C_1 = . \frac{2\upsilon}{1-\left(\frac{r_i}{r_a}\right)^2}$$

In other words, the radial ratio, r_i/r_a should be increased.

In Equation (4),

$$\sigma_z / E = C_0 \left(C_1(r) - C_2(r)\right)$$

$$C_2. = \frac{T_{(r)}}{T_{ma}}$$

where:
$$C_1 = \frac{2\upsilon}{1-\left(\frac{r_i}{r_a}\right)^2}$$

And,

$$C_0 = . T_{ma} * \alpha_{th} / (1 - \upsilon)$$

If C_1 is to be high,

Then the ratio r_i/r_a must be high

i.e., $r_a \approx r_i$

i.e., r_a should be reduced to the lowest value applicable.

A table of values can be formed for r_i = 35 cm:

See **Table 3**, above. The results for internal wall temperatures are presented in **Table 4**.

Table 3. A non-dimensional parameter, *C*1 by various external wall radius of model.

r_a [cm]	r_i/r_a	$1-\left(\frac{r_i}{r_a}\right)^2$	$2\nu / \left\{1-\left(\frac{r_i}{r_a}\right)^2\right\}$
38	0.92	0.1536	3.96
37	0.946	0.1052	5.70
36	0.97	0.055	10.95
35.5	0.986	0.028	21.42
35.25	0.993	0.014	42.86

Table 4. Axial stress function versus internal wall temperatures.

Time [secs]	T_{wi} [K]	Axial S_{tress} σ_{zth} [MPa] (Ufot, 2010)	Axial Stress Function (σ_{zth}/E) [-]	Axial Stress Function (Present model)
70	2027.8	−5820.0	−0.027714	−0.027113
140	2298.2	−6351.0	−0.030243	−0.029990
210	2392.4	−6531.0	−0.031100	−0.031005
350	2429.9	−6601.0	−0.031433	−0.031413
490	2433.0	−6607.0	−0.031462	−0.031447
630	2433.3	−6608.0	−0.031467	−0.031450
922.1	2584.1	−6746.7	−0.032127	−0.032127

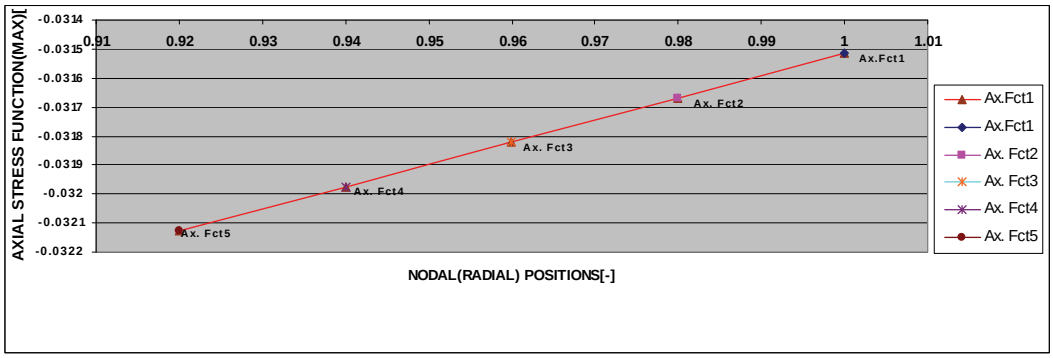

Figure 3. Axial stress function (Max) versus radial nodal positions radial nodal positions $r = r_i/r_a$.

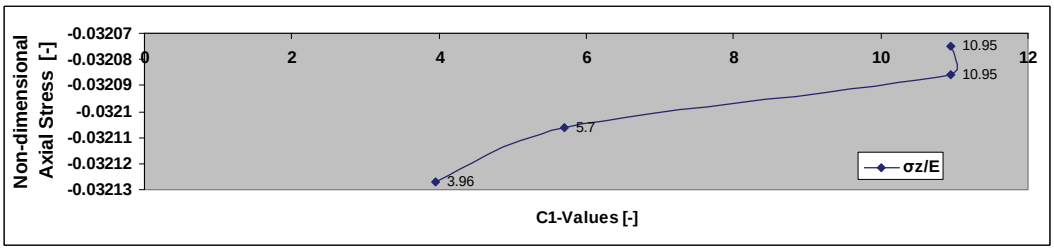

Figure 4. Non-dimensional axial stress versus *C*1.

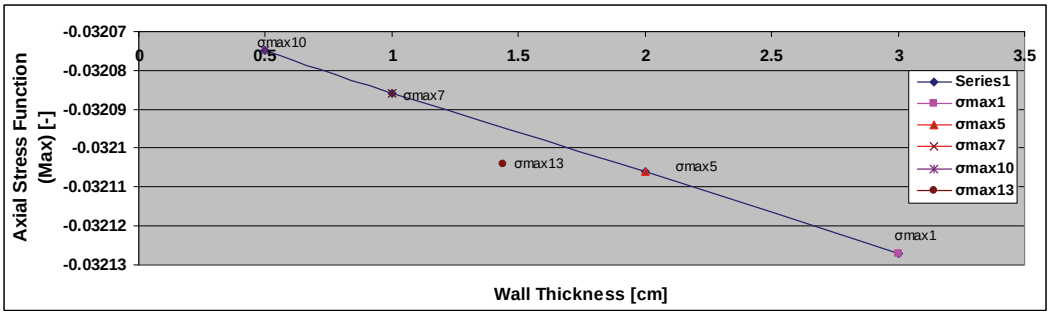

Figure 5. Axial stress function versus wall thickness - showing value position of point of inflection: σmax13.

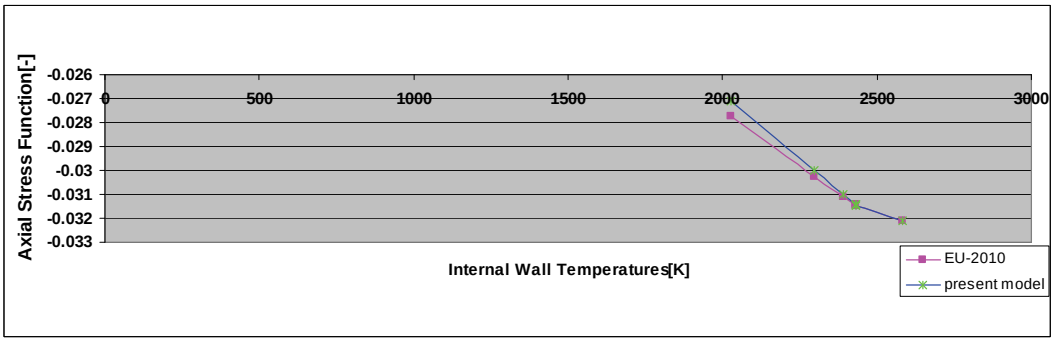

Figure 6. Axial stress function versus internal wall temperatures.

Figure 1 is a presentation of a non-dimensional axial stress against C_0-values. The non-dimensional temperature parameter, C_0, is the maximum average temperature dependent parameter. The stress shows a tendency of increasing with the C_0. That means to reduce the stress in the material, the maximum average temperature in the material must be reduced. And this maximum temperature is noted to be increasing with wall thickness. Therefore, in the final analysis, the wall thickness for minimal thermal stresses should be as small as applicable.

Figure 2 shows a point of Inflection in the presentation of axial stress/C_0 with wall thickness. Further consideration of this point of Inflection occurring at a wall thickness of 1.44 cm, shows an abnormal trends of temperatures and stresses in the material. In a cross-sectional view of the non-dimensional stress profile in the material shows linear relationship with the non-dimensional radial positions. In **Figure 4**, a non-dimensional axial stress is shown varying against C_1-values. The indicated C_1-value on the trend is showing that with very high values of C_1 the stress tends minimal. It is a definite method of influencing the stress levels in materials. It can be shown with **Figure 5** that to obtain very minimal axial stresses in material, the wall thickness should be reduced. As is shown in the figure, the stress values are reducing as the wall thickness is reduced. **Figure 6** shows that the Axial Stress Function increases with increased internal wall temperatures.

4. Conclusions

The work is very adequate in computing the thermal axial stress in combustors and cylindrical pipes at the instance of known wall surface temperatures. With the Non-dimensional consideration in the combustor axial Stress computation it is possible to indicate ways of minimizing the thermal axial stress in the material.

5. References

[1] G. N. Tret'yachenko, S. Karpinos and L. E. Kiyashko, "Thermal Stress State of Hollow Cylinders during Unilateral Internal Heating," UDC 539.319.624.074.4, 1976.

[2] I. J. Kumar and D. Rajgopalan, "Thermal Stresses in a Hollow Cylinder Due to a Sinusoidal Surface Heating Source," V. R. Thiruvenkatachar, F.N.I. Defence Science Laboratory, Delhi 6 I, 1969.

[3] K. Abrinia, H. Naee, F. Sadeghi and F. Djavanroodi, "New Analysis for the FGM Thick Cylinders under Combined Pressure and Temperature Loading," © 2008 Science Publications Tehran, Amirabad Shomali St., Tehran, Iran 852, 2008.

[4] S. Kubo, K. Uchida, T. Ishizaka and S. Ioka, "Determination of the Optimum Temperature History of Inlet Water for Minimizing Thermal Stresses in a Pipe by Multiphysics Inverse Analysis," *Journal of Physics*: *Conference Series*, Vol. 135, 2008, p. 012058.

[5] Y. Ootao, T. Akai and Y. Tanigawa, "Three-Dimensional

Transient Thermal Stress Analysis of a Non-Homogeneous Hollow Circular Cylinder Due to a Moving Heat Source in the Axial Direction," *Journal of Thermal Stresses*, Vol. 18, No. 5, 1995, pp. 497-512.

[6] S. Fronius and G. Trankner, "Taschenbuch Maschinenbau, Band 1/π Grundlagen," 3rd Edition, VEB Verlag Technik, Berlin, 1975.

[7] E. Ufot, "Modeling Thermal Stresses in the Combustor of Gas Turbine," Ph.D. Dissertation, Rivers State University of Science and Technology, Port Harcourt, 2010.

Engineering, 2010, 2, 740-749
doi:10.4236/eng.2010.29096 Published Online September 2010 (http://www.SciRP.org/journal/eng)

Profile Modification for Increasing the Tooth Strength in Spur Gear Using CAD

Shanmugasundaram Sankar[1], Maasanamuthu Sundar Raj[2], Muthusamy Nataraj[2]
[1]*Research Scholar, Anna University, Coimbatore, India*
[2]*Department of Mechanical Engineering, Government College of Technology, Coimbatore, India*
E-mail: {*shanmugasundaramsankar, m_natanuragct*}*@yahoo.com*
Received July 13, 2010; *revised August* 5, 2010; *accepted August* 18, 2010

Abstract

This paper examines the tooth failure in spur gears. Corrective measures are taken to avoid tooth damage by introducing profile modification in root fillet. In general, spur gear with less than 17 numbers of teeth had the problem of undercutting during gear manufacturing process which minimizes the strength of gear at root. In this study, a novel design method, namely circular root fillet instead of the standard trochoidal root fillet is introduced in spur gear and analyzed using ANSYS version 11.0 software. The strength of these modified teeth is studied in comparison with the standard design. The analysis demonstrates that the novel design exhibit higher bending strength over the standard trochoidal root fillet gear. The result reveals that the circular root fillet design is particularly suitable for lesser number of teeth in pinion and where as the trochoidal root fillet gear is more opt for higher number of teeth.

Keywords: Bending Stress, Circular Root Fillet, Deflection, Profile Modification, Spur Gear, Trochoidal Root Fillet

1. Introduction

The objective of the gear drive is to transmit power with comparatively smaller dimensions, runs reasonably free of noise and vibration with least manufacturing and maintenance cost. There is a growing need for higher load carrying capacity and increased fatigue life in the field of gear transmissions. Spitas and Costopoulos [1] have introduced one–sided involute asymmetric spur gear teeth to increase load carrying capacity and combine the meshing properties. Tesfahunegn and Rosa [2] investigated the influence of the shape of profile modifications on transmission error, root stress and contact pressure through non linear finite element approach. Spitas and Costopoulos [3] expressed that the circular fillet design is particularly suitable in gears with small number of teeth (pinion). Fredette and Brown [4] discussed the possibility of reducing gear tooth root stresses by adding internal stress relief features. Ciavarella and Demeliio [5] concluded that the fatigue life is lower on gears with a lesser number of teeth. Hebbal and Math [6] have reduced the root fillet stress in spur gear using internal stress relieving feature of different shapes. Senthilvelan and gnanamoorthy [7] studied the effect of gear tooth fillet radius on the performance of injection moulded nylon 6/6 gears. Tae Hyong Chong and Jae Hyong Myong [8] conducted a study to calculate simultaneously the optimum amounts of tooth profile modification for minimization of vibration and noise.

Beghini *et al*. [9] proposed a simple method to reduce the transmission error for a given spur gear at the nominal torque by means of the profile modification parameters. Researchers focused either on the development of advanced materials or new heat treatment methods or designing the gears with stronger tooth profiles. Gears having standard involute with smaller number of teeth (*i.e.*, less than 17 teeth) had the problem of undercutting. In gear manufacturing process the tooth root fillet is generated as the tip of the cutter removes material from the involute profile resulting teeth that have less thickness at root. This reduces the tooth strength and leads to the crack initiation and propagation at root fillet area. To improve the gear tooth strength many works have been done but all mostly employed positive profile shifting [10-13]. These contributions exhibit lower pitting and scoring resistance with lesser contact ratio resulting in more noise and vibration during the power transmission [14].

2. Gear Geometry

The involute spur gear with circular root fillet is illustrated in **Figure 1**. The point ´O´ is the center of the gear, 'Oy' is the axis of symmetry of the tooth and 'B' is the point where the involute profile starts from the form circle r_s.

'A' is the point of tangency of the circular fillet with the root circle r_f. 'D' laying on (ε_2) = 'OA' represents the center of the circular fillet. Line (ε_3) is tangent to the root circle at A and intersects with line (ε_1) at C. The fillet is tangent to the line (ε_1) at point E. Since it is always $r_s > r_f$, the proposed circular fillet can be implemented without exceptions on all spur gears irrelevant of number of teeth or other manufacturing parameters. A comparison of the geometrical shape of a tooth of circular fillet with that of standard fillet is presented in **Figure 2**.

The geometry of the circular fillet coordinates (points A and B) in **Figure 1** is obtained using the following formulas;

$X_A = r_f \sin(\zeta + \Omega_s)$, $Y_A = r_f \cos(\zeta + \Omega_s)$

$X_B = r_f \sin\Omega_s$, $Y_B = r_f \cos\Omega_s$

$X_D = (r_f + AD) \sin(\zeta + \Omega_s)$, $Y_D = (r_f + AD \cos(\zeta + \Omega_s)$

$X_E = (OC + CE) \sin\Omega_s$, $Y_E = (OC + CE) \cos\Omega_s$

2.1. Part Modeling

In actual practice, trochoidal root fillet is present in spur gear having large number of teeth (more than 17) and exhibits less bending stress for higher number of teeth.

The circular root fillet is preferable for gears with smaller number of teeth (less than 17) depending on the tip radius of the hob. The proposed teeth are composed of a standard involute working profile from the outer to the form circle of the gear and of a circular fillet profile from the form circle to the root circle of the gear replacing the conventional trochoidal fillet profile.

Table 1 gives the parametric specification of 15 teeth and 16 teeth spur gear. These design specifications have been arrived from KISS soft an application software for the given centre distance. The virtual model of the spur gear with 15 teeth and 16 teeth having Circular and Trochoidal root fillet are modeled in Pro-E wildfire version 3.0 software and are presented in the following **Figure 3** and **Figure 4.**

3. Force Analysis

The load transmitting capability of gear tooth is analyzed and checked for designing a gear system. The effective circumferential force on the tooth at the pitch circle of the gear while in meshing is estimated. Two kinds of stresses are induced in gear pair during the power transmission from one shaft to another shaft. They are: 1) Bending stress – Induced on gear teeth due to tangential force developed by the power and 2) Surface contact stress or Compressive stress. The load is assumed to be uniformly distributed along the face width of the tooth.

3.1. Components of Forces

When the mating gears are engaged the line of contact starts from bottom of the tooth to tip of the tooth along

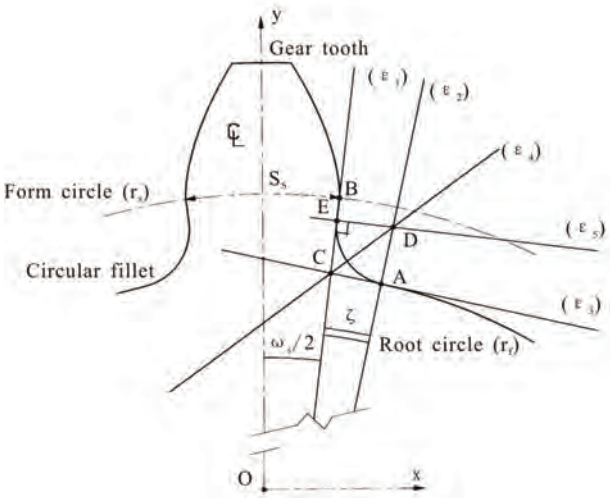

Figure 1. Geometry of the circular fillet.

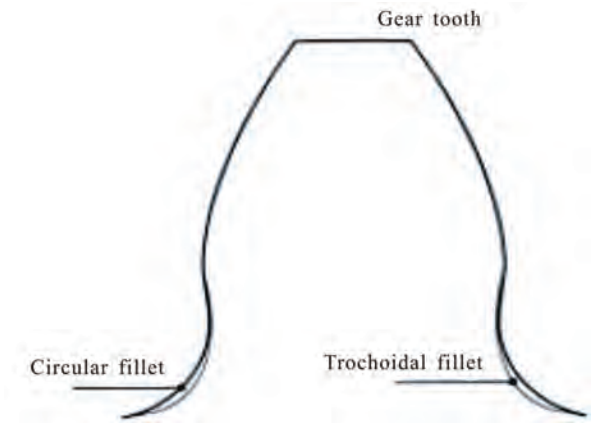

Figure 2. Superposition of circular fillet on a standard tooth.

Table 1. Specification of gear.

Gear tooth type	:	Standard involute full depth
Number of teeth (Z)	:	15 and 16
Normal module (mn)	:	4 mm
Pressure angle (α)	:	20°
Helix angle (β)	:	0°
Tooth root fillet	:	Trochoidal and Circular (proposed)

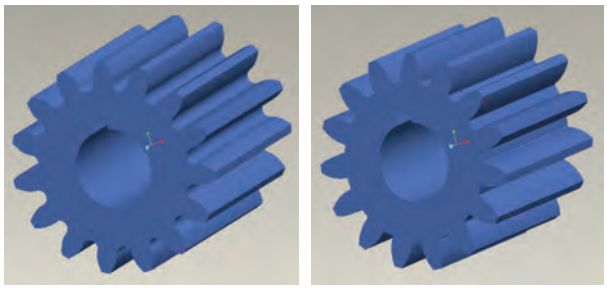

Circular fillet Trochoidal fillet

Figure 3. Gear with 15 teeth.

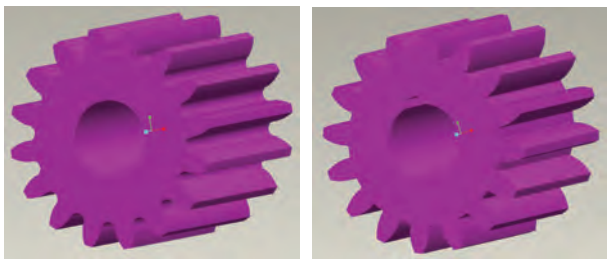

Circular fillet Trochoidal fillet

Figure 4. Gear with 16 teeth.

tooth-profile for the pinion and tip to bottom for the gear. While the force is acting at the tip of tooth, the long distance of action from root cause maximum bending stress at the bottom of tooth. Hence the force at this position (*i.e.*, at tip) is considered for analysis.

The normal force (F_n) to the tip of the gear is depicted in **Figure 5**. This force (F_n) is at an angle with the common tangent to pitch circle (*i.e.*, pressure angle) is resolved into two components:

1) Tangential Force (F_t)

2) RadialForce (F_r).

The tangential force 'F_t' or transmitting load can be derived from the following standard equation;

$F_t = [2000T]/d$

where, $T = 9550\ P/n$

Irrespective of the value of the contact ratio, the gear forces are effective on a single pair of teeth in mesh. Referring to **Figure 5**, the normal force (F_n) acts along the pressure line. The normal force produces an equal and opposite reaction at the gear tooth. Since the gear is mounted on the shaft, the radial force F_r acts at the centre of the shaft and is equal in magnitude but opposite in direction to the normal force F_n.

As far as the transmission power is concerned, the component of forces 'F_n' and 'F_r' plays no role and the driving component is tangential force 'F_t'. The tangential force 'F_t' constitutes a couple which produces the torque on the pinion which in turn drives the mating gears. The tangential force bends the tooth and the radial force compresses it. The magnitudes of the components of the normal force' F_n' are given by:

$F_t = F_n.\cos\alpha$

$F_r = F_n.\sin\alpha$

Forces are calculated based on power transmission (power is equal to 20 kW), the speed of the gear are 1000 rpm,1500 rpm and 2000 rpm respectively for which the components of forces are calculated for 15 teeth and 16 teeth and are given in **Table 2** and **Table 3**.

4. Finite Element Analysis

A finite element model with a single tooth is considered for analysis. Gear material strength is a major consideration for the operational loading and environment. Generally, cast iron is used in normal loading and higher wear resisting conditions. In modern practice, the heat treated alloy steels are used to overcome the wear resistance. ANSYS version 11.0 software is used for analysis. In this work, heat treated alloy is taken for analysis. The gear tooth is meshed in 3-dimensional (3-D) solid 20 nodes 92 elements with fine mesh. SOLID92 has a quadratic displacement behavior and is well suited to model irregular meshes. The material properties chosen for analysis are presented in **Table 4**.

Figure 6 illustrates a single tooth of 2-dimensional (2-D) Circular fillet roots and **Figure 7** shows a single tooth of 2-dimensional Trochoidal fillet roots. **Figure 8** shows the FEM meshed model of single tooth of Circular fillet roots. Similarly, **Figure 9** shows the FEM meshed model of single tooth Trochoidal fillet roots.

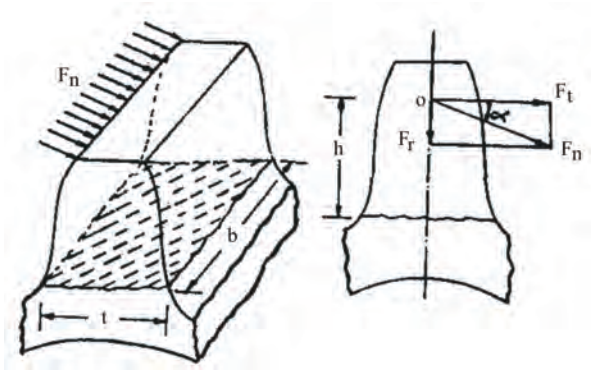

Figure 5. Tooth forces in spur gear.

Table 2. Force components for 15 teeth.

Speed (rpm)	Torque (N-mm)	Force Components (Newton)		
		F_t	F_n	F_r
1000	191000	6366.67	6775.27	2317.28
1500	127330	4244.44	4516.84	1544.85
2000	95500	3638.10	3871.58	1324.16

Table 3. Force components for 16 teeth.

Speed (rpm)	Torque (N-mm)	Force Components (Newton)		
		F_t	F_n	F_r
1000	191000	5968.75	6351.81	2172.45
1500	127330	3979.17	4234.54	1448.30
2000	95500	3410.71	3629.61	1241.40

Table 4. Material properties.

Gear material	:	Alloy structural steel
Density	:	7870 kg/m^3
Young's modulus	:	206 GPa
Poisons ratio	:	0.3
Yield strength	:	637 MPa

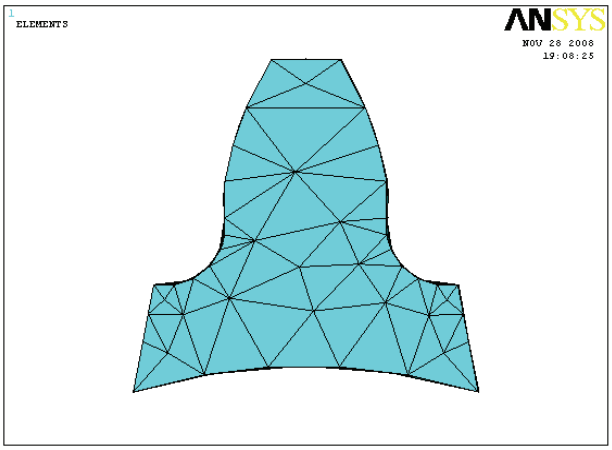

Figure 6. 2-D Circular root fillet tooth.

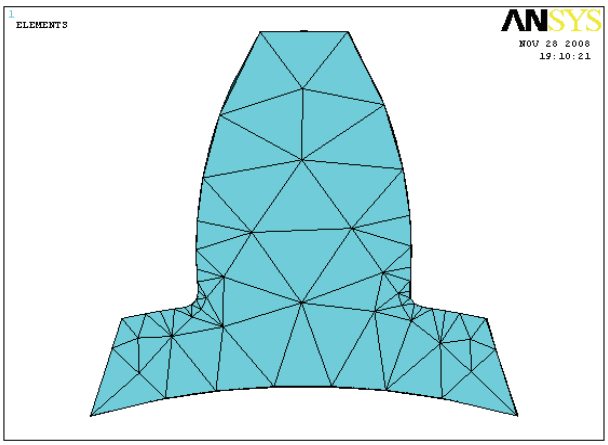

Figure 7. 2-D Trochidal root fillet tooth.

4.1. Displacement and Loading

In order to facilitate the finite element analysis, the gear tooth was considered as a cantilever beam. All the degrees of freedom were constrained at the root circle but for analysis purpose the constrained degrees of freedoms are transferred to gear hub surface. The revolutions of the gears are limited to 2000 rpm. In nonlinear contact analysis the tooth forces are applied on tip of the tooth profile.

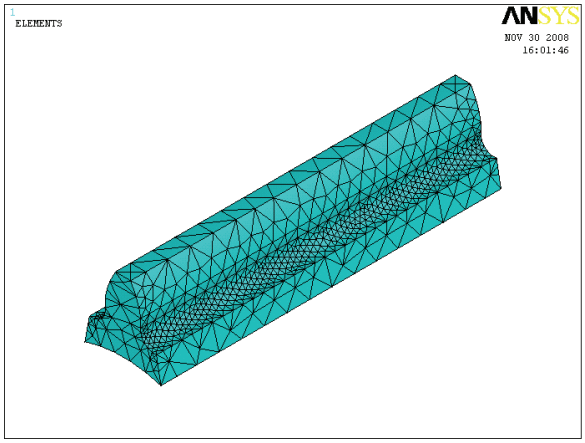

Figure 8. Meshed model of circular root fillet tooth.

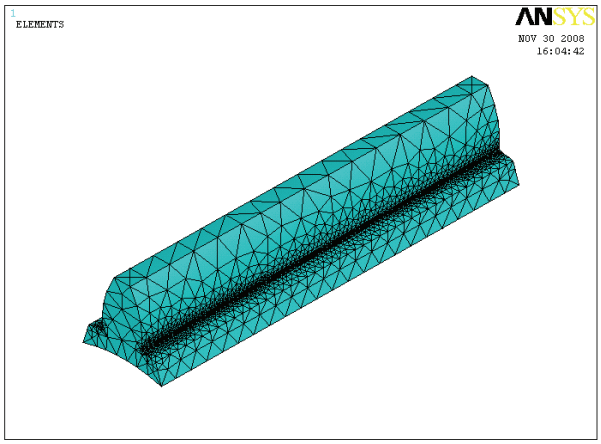

Figure 9. Meshed model of trochidal root fillet tooth.

5. Results and Discussion

The deflection and bending stress analysis were carried out for the spur gear with 15 teeth and 16 teeth. The induced bending stress and obtained deflection values are presented in **Table 5**.

The investigation reveals that the deflection value of both circular and trochoidal root fillet gears are identical. But, looking in to bending stress the 15T gear generated with circular root fillet have lesser stress (609.654 N/mm^2) at 1000 rpm when compared with trochoidal fillet gear (626.699 N/mm^2).

Correspondingly, the induced bending stress for 16 T circular root fillet gear at 2000 rpm was 348.374 N/mm^2

where as it was noticed as 358.114 N/mm^2 for 16 T trochoidal root fillet gear. The bending stress and deflection values taken from FEA results for 15 teeth gear with circular and trochoidal root fillet are depicted in **Figure 10**.

Similarly, the bending stress and deflection values taken from FEA results for 16 teeth gear with circular and trochoidal root fillet are depicted in **Figure 11**. It is observed from ANSYS study that the 16T gear generated with circular root fillet have lesser stress (328.381 N/mm^2) at 1000 rpm when compared with trochoidal fillet gear (558.287 N/mm^2). Also, the bending stress

Table 5. Deflection and bending stress result.

Speed	Deflection(mm)				Bending Stress (N/mm^2)			
	15 Teeth		16 Teeth		15 Teeth		16 Teeth	
	Trochoidal	Circular	Trochoidal	Circular	Trochoidal	Circular	Trochoidal	Circular
1000	0.013343	0.013747	0.013909	0.012407	626.699	609.654	558.287	328.381
1500	0.008895	0.009164	0.009272	0.008271	417.798	406.435	372.192	218.921
2000	0.007624	0.007855	0.007948	0.007090	358.114	348.374	319.021	187.646

15 Teeth - Deflection

Trochoidal Fillet | Circular Fillet

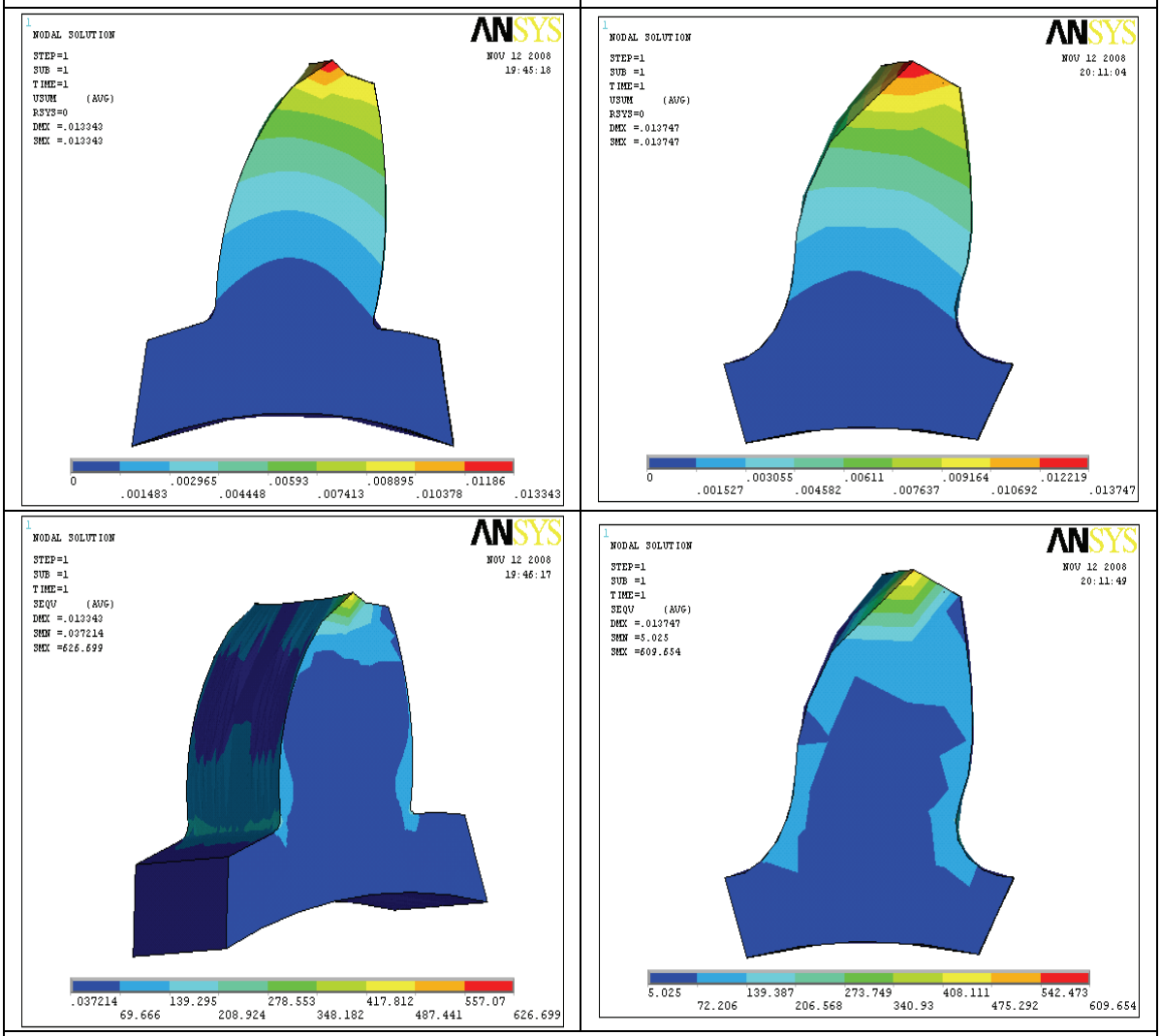

at 1000 rpm

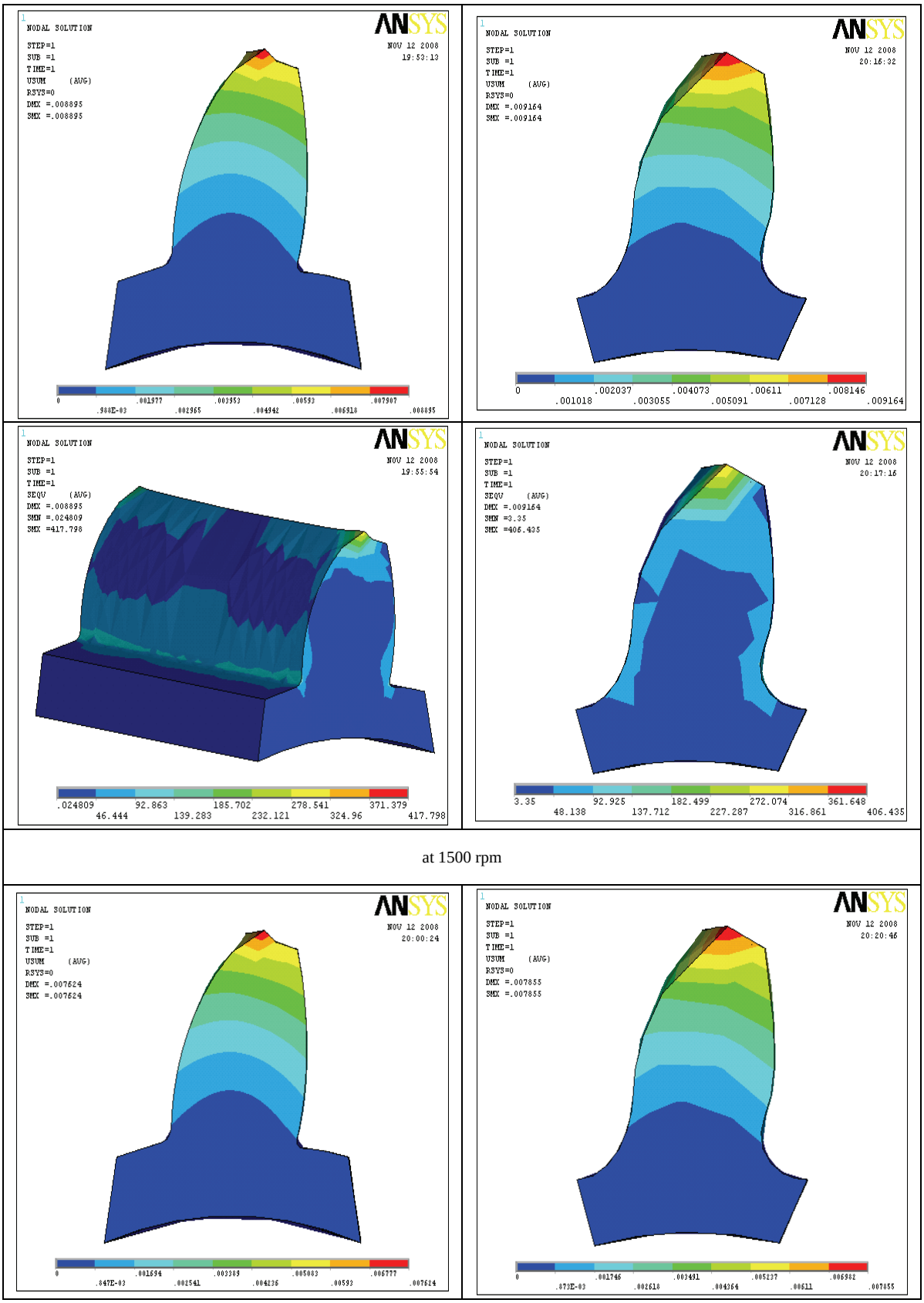
NODAL SOLUTION
STEP=1
SUB =1
TIME=1
USUM (AVG)
RSYS=0
DMX =.008895
SMX =.008895
ANSYS
NOV 12 2008
19:53:13
0
.001977
.002965
.003953
.004942
.00593
.006918
.007907
.008895
NODAL SOLUTION
STEP=1
SUB =1
TIME=1
USUM (AVG)
RSYS=0
DMX =.009164
SMX =.009164
ANSYS
NOV 12 2008
20:16:32
0
.001018
.002037
.003055
.004073
.005091
.00611
.007128
.008146
.009164
NODAL SOLUTION
STEP=1
SUB =1
TIME=1
SEQV (AVG)
DMX =.008895
SMN =.024809
SMX =417.798
ANSYS
NOV 12 2008
19:55:54
.024809
46.444
92.863
139.283
185.702
232.121
278.541
324.96
371.379
417.798
NODAL SOLUTION
STEP=1
SUB =1
TIME=1
SEQV (AVG)
DMX =.009164
SMN =3.35
SMX =406.435
ANSYS
NOV 12 2008
20:17:16
3.35
48.138
92.925
137.712
182.499
227.287
272.074
316.861
361.648
406.435
at 1500 rpm
NODAL SOLUTION
STEP=1
SUB =1
TIME=1
USUM (AVG)
RSYS=0
DMX =.007624
SMX =.007624
ANSYS
NOV 12 2008
20:00:24
0
.847E-03
.001694
.002541
.003389
.004236
.005083
.00593
.006777
.007624
NODAL SOLUTION
STEP=1
SUB =1
TIME=1
USUM (AVG)
RSYS=0
DMX =.007855
SMX =.007855
ANSYS
NOV 12 2008
20:20:46
0
.873E-03
.001746
.002618
.003491
.004364
.005237
.00611
.006982
.007855

at 1500 rpm

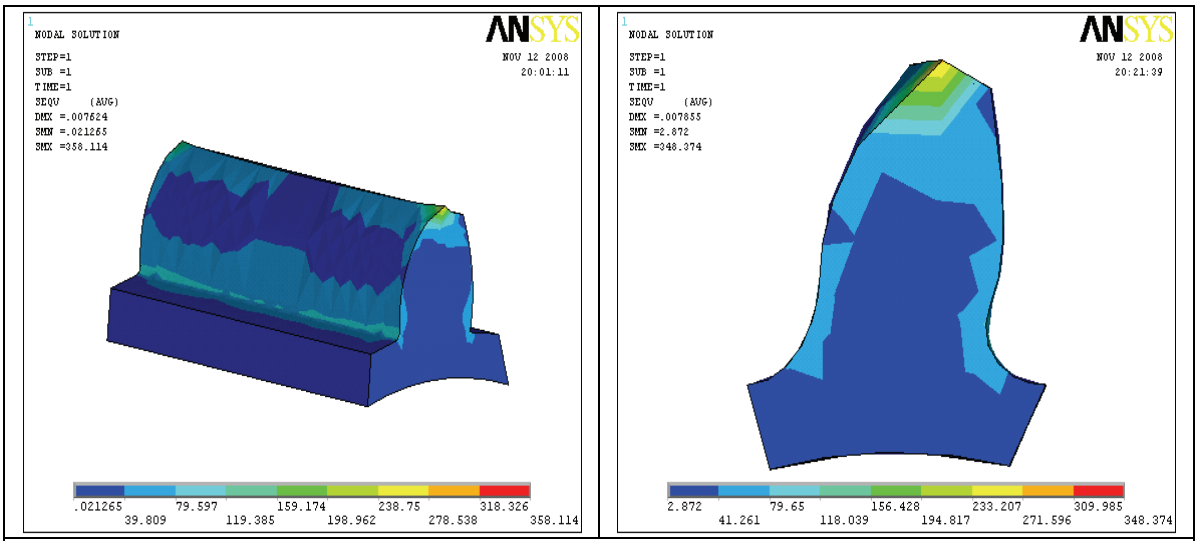

at 2000 rpm

Figure 10. FEA results for 15 teeth gear.

16 Teeth - Deflection

Trochoidal root fillet	**Circular root fillet**
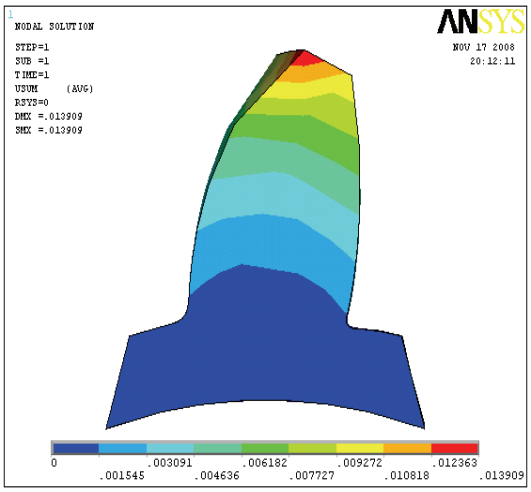	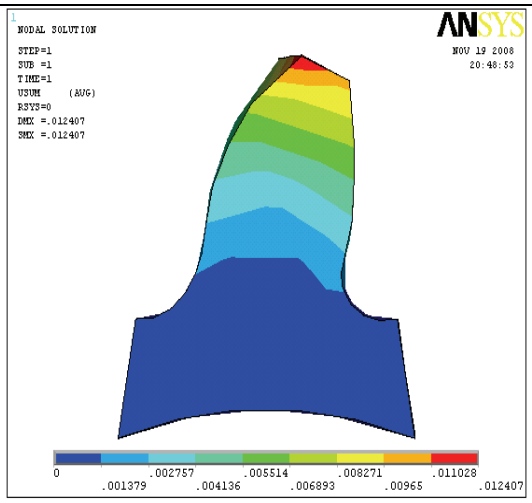
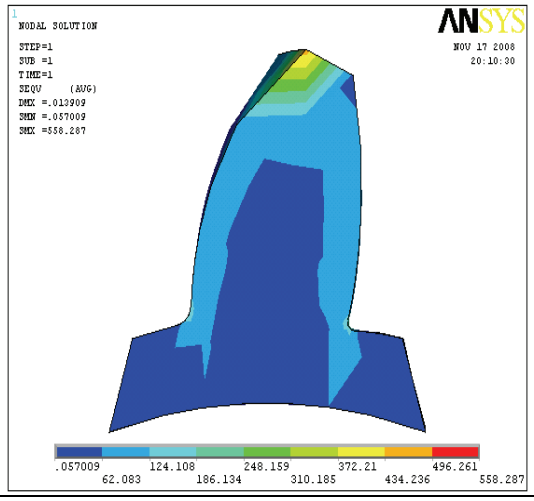	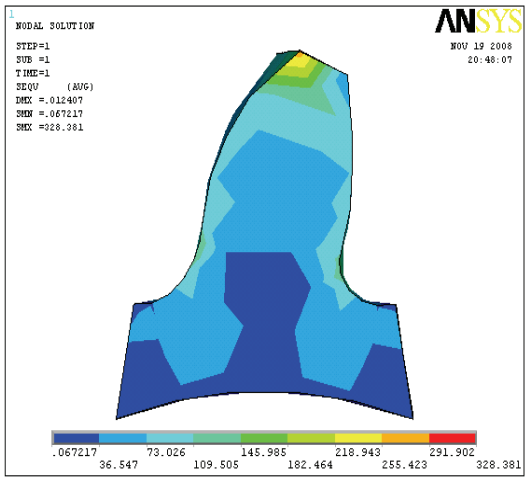

at 1000 rpm

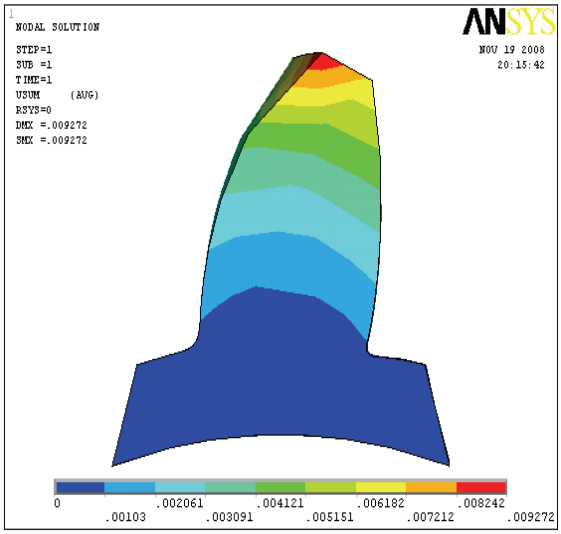

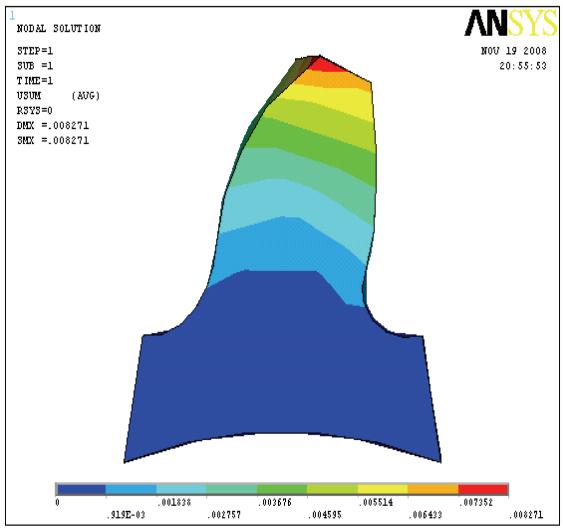

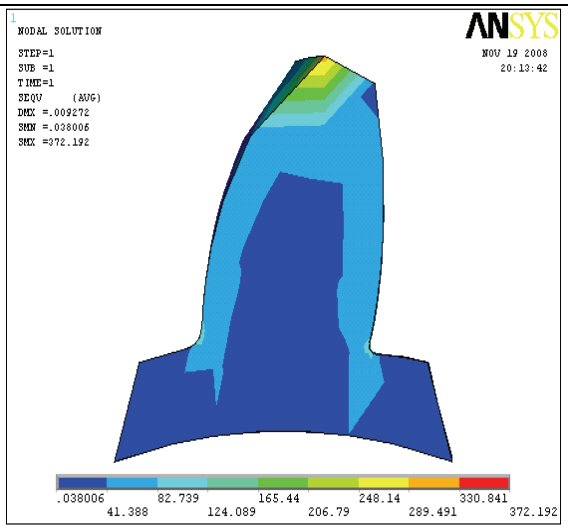

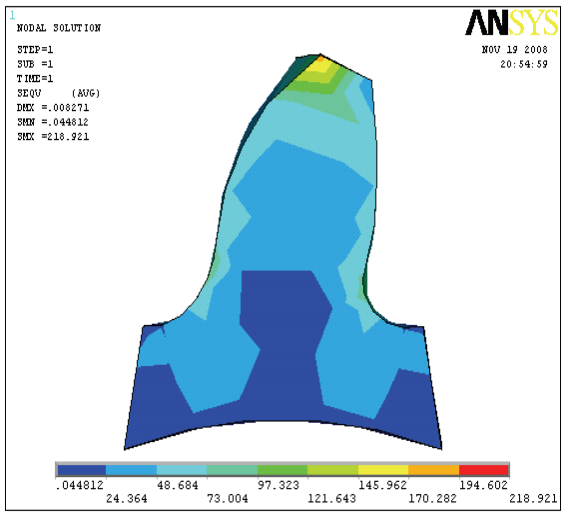

at 1500 rpm

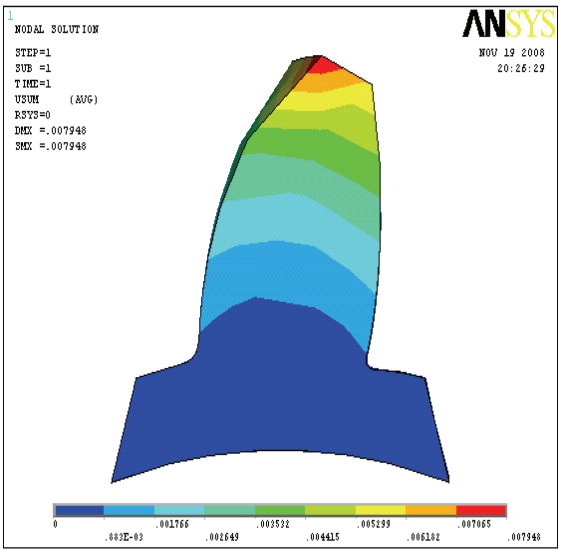

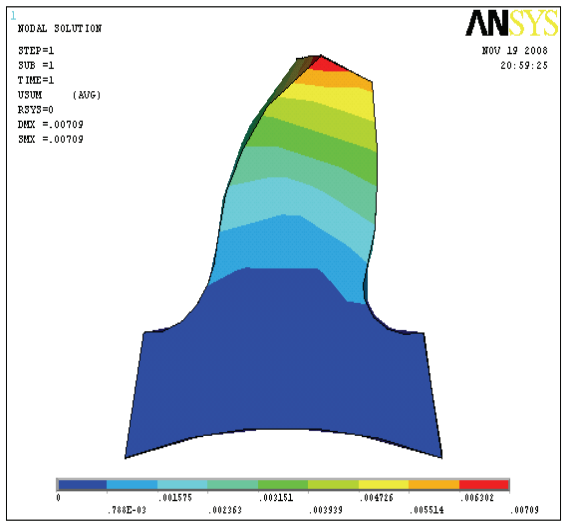

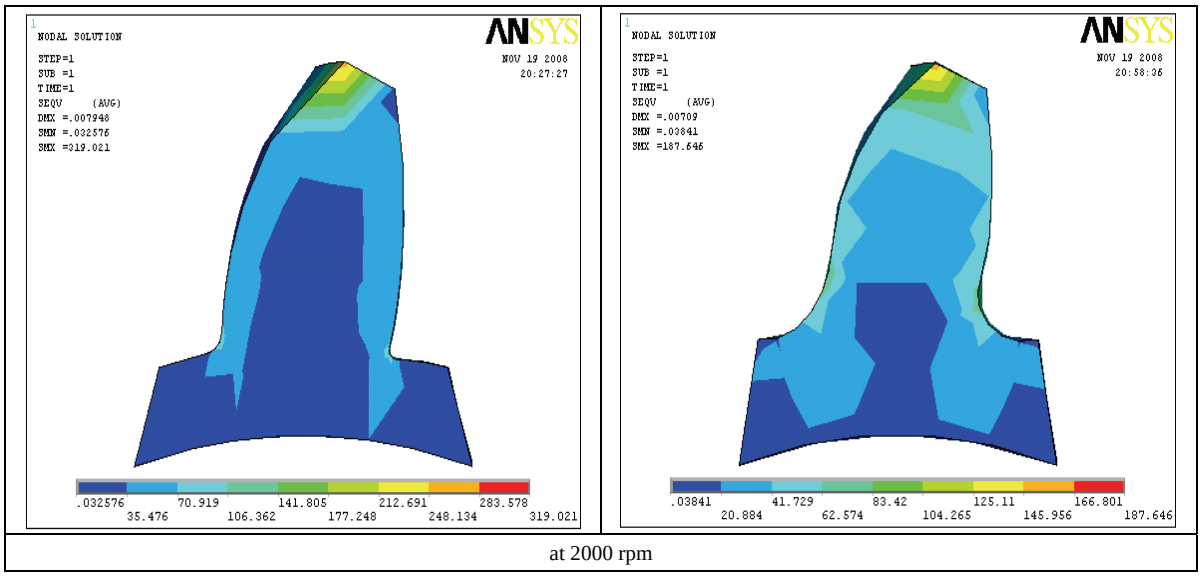

at 2000 rpm

Figure 11. FEA results for 16 teeth gear.

(187.646 N/mm^2) was least for 16 T circular root fillet gear at 2000 rpm when compared with trochoidal root fillet gear (319.021 N/mm^2). In sort, the results obtained from ANSYS result shows that the bending stress and deflection values are lesser for Circular root fillet gear irrespective of speed than Trochoidal root fillet gear.

6. Conclusions

The investigation result infers that the deflection in circular root fillet is almost same comparing to the trochoidal root fillet gear tooth. However, there is appreciable reduction in bending stress value for circular root fillet design in comparison to that of bending stress value in trochoidal root fillet design.

From the foregoing analysis it is also found that the circular fillet design is more opt for lesser number of teeth in pinion and trochoidal fillet design is more suitable for higher number of teeth in gear (more than 17 teeth) and whatever may be the pinion speed. In addition to that the ANSYS results indicates that the gears with circular root fillet design will result in better strength, reduced bending stress and also improve the fatigue life of gear material. Further work shall be done to ascertain the stiffness and rigidity of gear tooth in the circular root fillet design so that the feasibility of this particular design can be useful to put in practical application in future.

7. References

[1] T. Costopoulos and V. Spitas, "Reduction of Gear Fillet Stresses by Using One Sided Involute Asymmetric Teeth," *Mechanism and Machine Theory*, Vol. 44, No. 8, 2009, pp. 1524-1534.

[2] Y. A. Tesfahunegn and F. Rosa, "The Effects of the Shape of Tooth Profile Modification on the Transmission Error Bending and Contact Stress of Spur Gears," *Journal of Mechanical Engineering Science*, Vol. 224, No. 8, 2010, pp. 1749-1758.

[3] V. Spitas, T. Costopoulos and C. Spitas, "Increasing the Strength of Standard Involute Gear Teeth with Novel Circular Root Fillet Design," *American Journal of Applied Sciences*, Vol. 2, No. 6, 2005, pp. 1058-1064.

[4] L. Fredette and M. Brown, "Gear Stress Reduction Using Internal Stress Relief Features," *Journal of Mechanical Design*, Vol. 119, No. 4, 1997, pp. 518-521.

[5] M. Ciavarella and G. Demelio, "Numerical Methods for the Optimization of Specific Sliding Stress Concentration and Fatigue Life of Gears," *International Journal of fatigue*, Vol. 21, No. 5, 1999, pp. 465-474.

[6] M. S. Hebbal, V. B. Math and B. G. Sheeparamatti, "A Study on Reducing the Root Fillet Stress in Spur Gear Using Internal Stress Relieving Feature of Different Shapes," *International Journal of RTE*, Vol. 1, No. 5, May 2009, pp. 163-165.

[7] S. Senthilvelan and R. Gnanamoorthy, "Effects of Gear Tooth Fillet Radius on the Performance of Injection Moulded Nylon 6/6 Gears," *Materials and Design*, Vol. 27, No. 8, 2005, pp. 632-639.

[8] T. H. Chong, T. H. Myong and K. T. Kim, "Tooth Modification of Helical Gears for Minimization of Vibration and Noise," *International Journal of KSPE*, Vol. 2, No. 4, 2001, pp. 5-11.

[9] M. Beghini, F. Presicce and C. Santus, "A Method to Define Profile Modification of Spur Gear and Minimize the Transmission Error," *AGMA Fall Technical Meeting*, Milwaukee, Wisconsin, October 2004, pp. 1-28.

[10] ISO, 6336-3, "Calculation of the Load Capacity of Spur

and Helical Gears-Part 3," Calculation of Bending Strength, 1996.

[11] AGMA, 2101-C95, "Fundamental Rating Factors and Calculation Methods for Involute Spur and Helical Gear (Metric Version)," American Gear Manufacturers Association, 1995.

[12] H. H. Mabie, C. A. Rogers and C. F. Reinholtz, "Design of Nonstandard Spur Gears Cut by a Hob," *Mechanism and Machine Theory*, Vol. 25, No. 6, 1990, pp. 635-644.

[13] C. A. Rogers, H. H. Mabie and C. F. Reinholtz, "Design of Spur Gears Generated with Pinion Cutters," *Mechanism and Machine Theory*, Vol. 25, No. 6, 1990, pp. 623-634.

[14] G. Niemann,"Maschinenelemente," Band 2, Springer, Verlag, 1965.

Nomenclature

F_n – Normal force
P – Rated power
F_t – Tangential force
d – PCD of gear
R – Reaction of shaft
n – Speed of the gear in rpm
r_f – Root Circle of gear
T – Transmitted Torque
S_s – Arc length at BCD
r_s – Form Circle of gear
FEA – Finite Element Analysis

Call for Papers

ENGINEERING

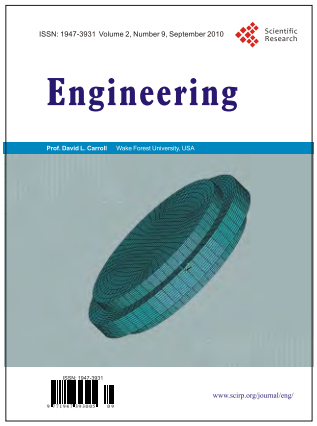

A Journal Published by Scientific Research Publishing, USA

www.scirp.org/journal/eng

ENGINEERING is an international journal dedicated to the latest advancement of engineering. The goal of this journal is to provide a platform for engineers and academicians all over the world to promote, share, and discuss various new issues and developments in different areas of engineering. All manuscripts must be prepared in English, and are subject to a rigorous and fair peer-review process. Accepted papers will immediately appear online followed by printed hard copy. The journal publishes original papers including but not limited to the following fields:

- Aerospace Engineering
- Agricultural Engineering
- Chemical Engineering
- Civil Engineering
- Electrical Engineering
- Environmental Engineering
- Industrial Engineering
- Materials Engineering
- Mechanical Engineering
- Mining Engineering
- Nanotechnology
- Nuclear Engineering
- Power Engineering
- Test Engineering
- Transportation Engineering

We are also interested in: 1) Short Reports—2-5 page papers where an author can either present an idea with theoretical background but has not yet completed the research needed for a complete paper or preliminary data; 2) Book Reviews—Comments and critiques.

☆ Notes for Intending Authors

Submitted papers should not be previously published nor be currently under consideration for publication elsewhere. Paper submission will be handled electronically through the website. For more details, please access the website.

☆ Website and E-Mail

http://www.scirp.org/journal/eng eng@scirp.org

Engineering, 2010, 2, 673-749
Published Online September 2010 in SciRes (http://www.scirp.org/journal/eng/)

TABLE OF CONTENTS

Volume 2 Number 9 **September 2010**

